Computational Microscopy: Breaking the Limit of Conventional Optics

Thesis by
Xiaoze Ou

In Partial Fulfillment of the Requirements for the
degree of
Doctor of Philosophy

CALIFORNIA INSTITUTE OF TECHNOLOGY
Pasadena, California

2016
Defended April 5th, 2016

Xiaoze Ou
ORCID: 0000-0001-9918-0221

ACKNOWLEDGEMENTS

First and foremost, I would like to express my sincere gratitude to my advisor, Dr. Changhuei Yang, for the guidance throughout my studies at Caltech. He was insightful to point me in the right direction whenever I felt puzzled, supportive for all kinds of discussion and bold ideas, and patient with the mistakes I make. From him I learned about the characteristics of being a great researcher: intellectual curiosity, determination, self motivation, imagination, and humbleness, all of which I will keep on pursuing to possess as I advance in my future career.

I also want to express my appreciation to Dr. Yu-Chong Tai, Dr. P. P. Vaidyanathan, Dr. Mikhail G. Shapiro, and Dr. Long Cai, for being members of my committee. Their insightful comments and generous advice have encouraged me to explore more deeply and broadly for my thesis work.

I would like to give my special thanks to Dr. Guoan Zheng, who mentored me from day one of my study in Caltech. I appreciate all the time we spent together, discussing ideas and carrying out experiments. Without his guidance and inspiration, it would have been impossible for me to finish the projects that led to this thesis. I would also like to thank Dr. Roarke Horstmeyer and Mr. Jaebum (Albert) Chung, who worked with me hand in hand on these projects. I cannot image having better colleagues and buddies.

Everyone in the biophotonics lab is awesome. I want to thank Ms. Anne Sullivan, the 'mom' of our group, for the great management of our lab, and the care and love for us. I would like to thank Dr. Ying Min Wang, Dr. Seung Ah Lee, Dr. Benjamin Judkewitz, Dr. Jian Ren, Dr. Lap Man Lee, Dr. Shuo Pang, and Dr. Chao Han for being my role models. I would like to thank all my friends and colleagues in the lab: Dr. Haowen Ruan, Joshua Brake, Michelle Cua, Mooseok Jang, Jinho Kim, Helen Lu, Daniel Martin, Donghun Ryu, and Edward Zhou. You guys are the best teammates ever. I wouldn't have made it through my five years of Ph.D. studies without being around with you.

I also want to thank Albert and Helen for helping with revising my thesis, and Josh for the advice and assistance on latex.

Finally, I want to dedicate my sincerest gratitude to my parents and my girlfriend Kun. You are always my strongest support and my patientest listeners. Your love makes me a better person, for both my work and my life.

ABSTRACT

Computational imaging is flourishing thanks to the recent advancement in array photodetectors and image processing algorithms. This thesis presents Fourier ptychography, which is a computational imaging technique implemented in microscopy to break the limit of conventional optics. With the implementation of Fourier ptychography, the resolution of the imaging system can surpass the diffraction limit of the objective lens's numerical aperture; the quantitative phase information of a sample can be reconstructed from intensity-only measurements; and the aberration of a microscope system can be characterized and computationally corrected. This computational microscopy technique enhances the performance of conventional optical systems and expands the scope of their applications.

PUBLISHED CONTENT AND CONTRIBUTIONS

[1] X. Ou, J. Chung, R. Horstmeyer, and C. Yang, "Aperture scanning Fourier ptychographic microscopy," *Biomedical Optics Express (to be submitted)*, 2016,
X. Ou participated in the conception of the project, designed and carried out the experiment, processed and analyzed the data, and wrote the manuscript.

[2] J. Chung, H. Lu, X. Ou, H. Zhou, and C. Yang, "Wide-field Fourier ptychographic microscopy using laser illumination source," *ArXiv preprint arXiv: 1602.02901*, 2016,
X. Ou participated in the conception of the project, data analysis, and manuscript writing.

[3] J. Chung, J. Kim, X. Ou, R. Horstmeyer, and C. Yang, "Wide field-of-view fluorescence image deconvolution with aberration-estimation from Fourier ptychography," *Biomedical Optics Express*, vol. 7, no. 2, pp. 352–368, 2016. DOI: 10.1364/BOE.7.000352,
X. Ou participated in the conception of the project, design of experimental setup, data processing for imaging system aberration, and manuscript writing.

[4] J. Chung, X. Ou, R. P. Kulkarni, and C. Yang, "Counting white blood cells from a blood smear using Fourier ptychographic microscopy," *PloS one*, vol. 10, no. 7, e0133489, 2015. DOI: 10.1371/journal.pone.0133489,
X. Ou participated in the conception of the project, design of experiment, image processing and analysis, and manuscript writing.

[5] R. Horstmeyer, R. Y. Chen, X. Ou, B. Ames, J. A. Tropp, and C. Yang, "Solving ptychography with a convex relaxation," *New journal of physics*, vol. 17, no. 5, p. 053 044, 2015. DOI: 10.1088/1367-2630/17/5/053044,
X. Ou participated in the design of experiment, data acquisition, image processing, and manuscript writing.

[6] R. Horstmeyer, X. Ou, G. Zheng, P. Willems, and C. Yang, "Digital pathology with Fourier ptychography," *Computerized Medical Imaging and Graphics*, vol. 42, pp. 38–43, 2015. DOI: 10.1016/j.compmedimag.2014.11.005,
X. Ou participated in the design of experiment, data acquisition, and image processing.

[7] X. Ou, R. Horstmeyer, G. Zheng, and C. Yang, "High numerical aperture Fourier ptychography: Principle, implementation and characterization," *Optics express*, vol. 23, no. 3, pp. 3472–3491, 2015. DOI: 10.1364/OE.23.003472,
X. Ou initiated the project, designed and implemented the experiment, processed and analyzed the data, and wrote the manuscript.

[8] R. Horstmeyer, X. Ou, J. Chung, G. Zheng, and C. Yang, "Overlapped Fourier coding for optical aberration removal," *Optics express*, vol. 22, no. 20, pp. 24 062–24 080, 2014. DOI: 10.1364/OE.22.024062,
X. Ou participated in the design of experiment, data analysis, and manuscript writing.

[9] G. Zheng, X. Ou, R. Horstmeyer, J. Chung, and C. Yang, "Fourier ptychographic microscopy: A gigapixel superscope for biomedicine," *Optics and Photonics News*, vol. 25, no. 4, pp. 26–33, 2014. DOI: 10.1364/OPN.25.4.000026,
X. Ou participated in the design of experiment, data acquisition and analysis, and manuscript writing.

[10] A. Williams, J. Chung, X. Ou, G. Zheng, S. Rawal, Z. Ao, R. Datar, C. Yang, and R. Cote, "Fourier ptychographic microscopy for filtration-based circulating tumor cell enumeration and analysis," *Journal of biomedical optics*, vol. 19, no. 6, pp. 066 007–066 007, 2014. DOI: 10.1117/1.JBO.19.6.066007,
X. Ou participated in the design of experiment, acquired and analyzed the data, and participated in manuscript writing.

[11] S. A. Lee, J. Erath, G. Zheng, X. Ou, P. Willems, D. Eichinger, A. Rodriguez, and C. Yang, "Imaging and identification of waterborne parasites using a chip-scale microscope," *PloS one*, vol. 9, no. 2, e89712, 2014. DOI: 10.1371/journal.pone.0089712,
X. Ou participated in the data processing, and manuscript writing.

[12] S. Dong, R. Horstmeyer, R. Shiradkar, K. Guo, X. Ou, Z. Bian, H. Xin, and G. Zheng, "Aperture-scanning Fourier ptychography for 3d refocusing and super-resolution macroscopic imaging," *Optics express*, vol. 22, no. 11, pp. 13 586–13 599, 2014. DOI: 10.1364/OE.22.013586,
X. Ou participated in the conception of project, design and implementation of experiment.

[13] X. Ou, G. Zheng, and C. Yang, "Embedded pupil function recovery for Fourier ptychographic microscopy," *Optics express*, vol. 22, no. 5, pp. 4960–4972, 2014. DOI: 10.1364/OE.22.004960,
X. Ou initiated the project, designed and implemented the experiment, processed and analyzed the data, and wrote the manuscript.

[14] G. Zheng, X. Ou, and C. Yang, "0.5 gigapixel microscopy using a flatbed scanner," *Biomedical optics express*, vol. 5, no. 1, pp. 1–8, 2014. DOI: 10.1364/BOE.5.000001,
X. Ou participated in the design of experiment, acquired and analyzed the data, processed the image, and participated in manuscript writing.

[15] X. Ou, R. Horstmeyer, C. Yang, and G. Zheng, "Quantitative phase imaging via Fourier ptychographic microscopy," *Optics letters*, vol. 38, no. 22, pp. 4845–4848, 2013. DOI: 10.1364/OL.38.004845,

X. Ou participated in the design of experiment, acquired and analyzed the data, processed the image, and wrote the manuscript.

[16] G. Zheng, X. Ou, R. Horstmeyer, and C. Yang, "Characterization of spatially varying aberrations for wide field-of-view microscopy," *Optics express*, vol. 21, no. 13, pp. 15 131–15 143, 2013. DOI: 10.1364/OE.21.015131,
X. Ou participated in the design of experiment, acquired and analyzed the data, processed the image, and participated in the manuscript writing.

[17] S. A. Lee, X. Ou, J. E. Lee, and C. Yang, "Chip-scale fluorescence microscope based on a silo-filter complementary metal-oxide semiconductor image sensor," *Optics letters*, vol. 38, no. 11, pp. 1817–1819, 2013. DOI: 10.1364/OL.38.001817,
X. Ou participated in the data processing, and manuscript writing.

TABLE OF CONTENTS

LIST OF ILLUSTRATIONS

LIST OF TABLES

Chapter 1

INTRODUCTION TO OPTICAL MICROSCOPY

A microscope is an instrument designed to produce a magnified image of small objects, which is widely applicable to a large number applications in areas such as biological research, clinical diagnosis, semiconductor inspection, etc. The optical microscope, which uses visible light to convey sample information, is the one with longest history and broadest scope of application.

This history of the microscope can date back to the 16th century, when British microscopist Robert Hooke invented a simple compound microscope, which already consists of an objective lens and an eye-piece, in the 1660s. Ever since then, the field of microscopy has been gradually evolving. A few key points in the course of microscopy development include the following: in 1886, Ernst Abbe's work with Carl Zeiss formed the key theory on microscope image formation [1], leading to the production of the aberration-corrected objective lens. In 1893, August Köhler developed an illumination scheme (Köhler illumination) which allowed microscopists to take full advantage of the resolving power of Abbe's objective [2]. In 1934, Dutch physicist Frits Zernike invented phase contrast microscopy, a contrast-enhancing optical technique that converts phase variation into intensity distribution and largely expands the observable sample range of microscope. Georges Nomarski introduced differential interference contrast microscopy in 1955, another important contrast-enhancement technique for the observation of unstained, transparent samples. Starting from late 1980s, most of the major manufacturers of the microscope migrate from finite corrected to infinity-corrected optics, which provides a larger intermediate parallel light path that can freely add-in slabs such as polarizers or filters.

In this chapter, the structure of modern microscope will be introduced, and a few key parameters will be pointed out and analyzed. At the end of the chapter, limitations of modern optical microscope will be explained.

1.1 Modern Microscope Model and Performance

Most modern microscopes use the infinity-corrected ray path structure, as shown in Fig. 1.1. The magnification optic is composed of an objective lens with

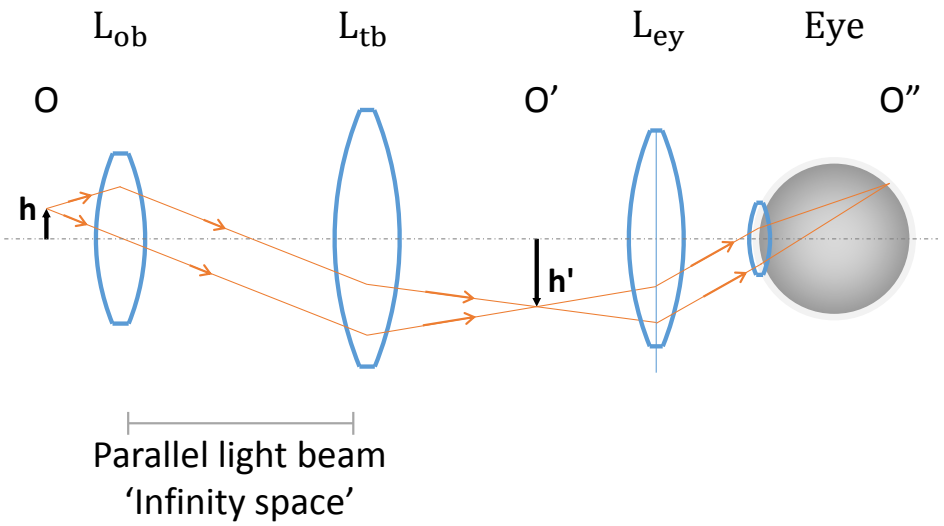

Figure 1.1: Infinity-corrected microscope ray path. O: object plane, O': intermediate image plane, O": image plane on retinal. L_{ob}: objective lens, L_{tb}: tube lens, L_{ey}: eyepiece. h: object height, h': intermediate image hight.

focal length L_{ob} and a tube lens with focal length L_{tb}. The object is placed at the front focal plane of the objective, and thus the collected light from a point from the object will be focused to infinitely far away (parallel light), which is where the name 'infinity-corrected' is from. The parallel light is then refocused onto a point in the intermediate image plane by the tube lens. From simple geometrical optics theory, we can derive that the magnification of the object $M = \frac{h'}{h} = \frac{L_{tb}}{L_{ob}}$. The magnified image can be further magnified by placing an eyepiece a focal length away and observed by human eye, or can be recorded by placing a film or photo-electronic array detector at the intermediate image plane.

Resolution

As mentioned above, the combination of objective and tube lens forms a magnified image of the sample, with magnification defined as $M = \frac{L_{tb}}{L_{ob}}$. We note that 'magnification' only means the scale of the feature; the amount of detail we can distinguish from the sample is determined by 'resolution', which is defined as the smallest resolvable distance of two points on the object side. Fundamentally, the resolution of the microscope is limited because the wave property of light causes diffraction.

Let's look at a point on the object plane. According to ray optics theory, the light coming out from this point will be collected by the optics and refocused on the

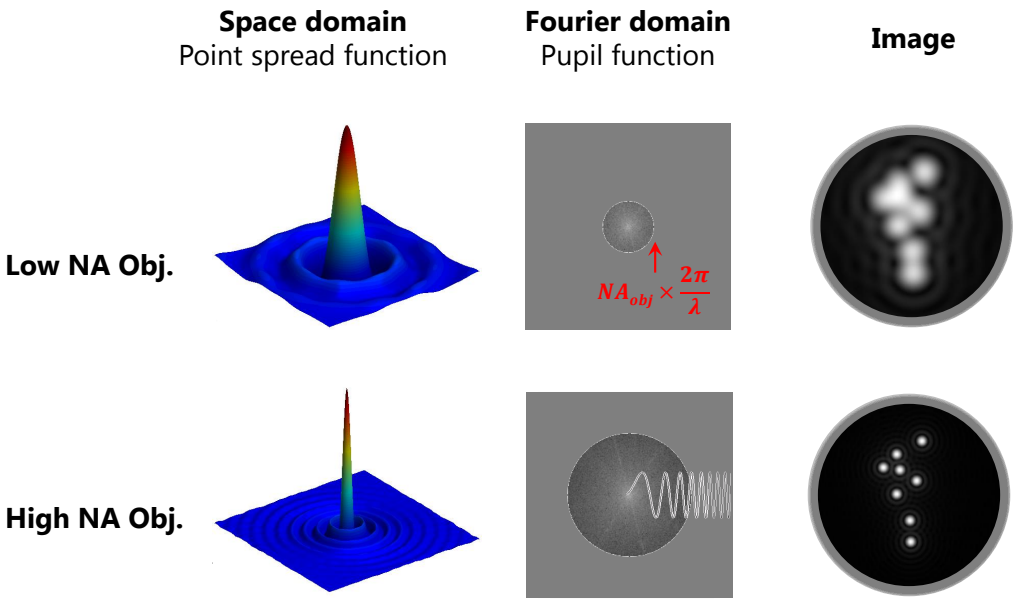

Figure 1.2: The resolution of a microscope system can be analyzed from space domain and Fourier domain

intermediate plane, forming a point image. However, because of the diffraction of the light, what will form on the image plane is a diffraction pattern. The size and shape of the diffraction pattern is determined by the cone of light that is collected and the wavelength of the light. Take a circular-shape light cone with collection angle of θ and wavelength λ as an example: the diffraction pattern will be a first order Bessel function (Airy disk), as shown in Fig. 1.2. Because the optical system is a space-invariant linear system [3], the image of a complex sample is the convolution of the sample distribution with the impulse response (point-spread function (PSF)) of the optical system .

For the case of two-point target imaging, when the two points are placed too close, their point spread functions will merge into one and we can not tell if the target has two points or one big dot. The smallest resolvable distance on the sample side can be derived as $r = \frac{\alpha\lambda}{\mathrm{NA}}$, where α is a parameter between 0.4 to 1 determined by the criteria used in the resolvability analysis, and NA is the numerical aperture of the objective defined as $\mathrm{NA} = n \sin\theta$ with n being the refractive index between the sample and the objective lens. Further analysis on resolving criteria is described in Appendix A.4. Intuitively, higher NA means a larger collection cone of light, which will form a sharper PSF, resulting in a smaller resolvable distance.

Another way of resolution analysis is in the spatial frequency domain (Fourier

domain), in which higher spatial frequency represents higher periodicity of the target, in other words, higher resolution feature. The combination of objective lens with tube lens can be treated as a 4f imaging system [4], in which the sample placed at the front focal plane is Fourier transformed by the objective lens, low pass filtered because of the limited NA, and then invert Fourier transformed by the tube lens and forms the image. The low pass filter is the pupil function of the system, which is the Fourier transform of the point spread function. When the sample is under coherent illumination, the low pass filter has all 1 inside the pass band, 0 outside the pass band, and a sharp cutoff frequency determined by the NA: $k_c = \frac{2\pi}{\lambda}\text{NA}$, which is called the coherent transfer function (CTF) of the microscope system [3]. Intuitively, higher NA allows information of higher spatial frequencies to pass through the system and form images with higher resolution.

Field of View

The field of view (FOV) of a microscope, as its name implies, is the area on the sample plane that can be viewed simultaneously through the microscope. This property is characterized by field number (F.N.) of the objective lens, which is the diameter of the view field in millimeter measured at the intermediate image plane. Therefore, the field size in the sample plane can be easily calculated as: $\text{FieldSize} = \frac{\text{F.N.}}{M}$. A typical microscope objective has a F.N. of 20 to 26.5.

Optical Aberration

Aberration is the phenomenon that actual light ray's trajectory deviates from the prediction of paraxial optics, resulting in a degradation of image quality. The existence of aberration is not due to the flaws in optical elements, but rather it roots in the inaccurate model of simple paraxial theory to describe the effect of an optical system on light.

In the derivation of image formation, the basic rule that one uses is Snell's law, which describes the behavior of light at the interface of two different isotropic media: $n_1 \sin\theta_1 = n_2 \sin\theta_2$. What the equation states is that the product of refractive index and the sine of the angle of incidence remains a constant when the light passes through the interface. In order to make the imaging system a linear system, paraxial approximation is made in which $\sin\theta \approx \theta$. This assumption is only valid when the angle is small. For a light ray with large incident or refraction angle, it will deviate from the prediction of paraxial theory and cause aberration.

Other causes of aberration include the curvature of the image plane, the dis-

tortion caused by varying magnification of different areas in the FOV, chromatic aberration caused by dispersion of the material, and the extra aberrations due to the flaws of optical elements and misalignment in assembly.

Aberration is a key bottleneck that restricts the overall performance of microscope. A large portion of the effort for modern microscope design is to correct for aberrations. Multiple pieces of lens, advanced materials, and free-form surfaces are used to make objective lenses with better performance. Despite the efforts, aberrations can not be eliminated entirely, they can only be brought down to tolerable range.

From the above analysis, we know that the larger the incident or refraction angle, the more severely the aberrations need to be corrected. On one hand, a larger NA objective will require the collection of light coming from a steeper angle, and on the other hand, a larger FOV means that the light from the edge of the sample will have a steeper angle. Because the total amount of aberration that can be corrected is limited with a certain aberration-correction method, there exists a compromise between NA and FOV: one of the parameters needs to be brought down if the other one needs to be brought up. The result is that if we want to make the NA larger for the observation of a finer feature, we have to sacrifice the FOV, meaning that the area of the sample we can observe at the same time will become smaller. The same compromise exists vise versa.

Spatial Bandwidth Product of Microscope Objective

From the view-point of information theory, the compromise between NA and FOV means the 'information transfer' from sample to image is limited by the 'bandwidth' of the channel, which is the microscope system in our case. We can use the term spatial bandwidth product (SBP) [5] to describe the throughput of the system.

The SBP of the objective lens is defined as the total amount of pixel counts on the image plane. Assuming an objective has diffraction-limited-resolution performance over the entire FOV, the resolution of it is determined by $r = 0.73\lambda/\text{NA}$, using sparrow resolution limit under coherent illumination. According to Nyquist sampling theory, the effective pixel size is half of the resolution $\frac{r}{2}$. The FOV area at the sample plane can be calculated as $\pi * (\frac{\text{F.N.}/2}{M})^2(\text{mm}^2)$, so the SBP can be defined as:

$$SBP = \pi \cdot (\frac{\text{F.N.}/2}{M})^2/(\frac{r}{2})^2 = \frac{\pi \cdot (\text{F.N.} \cdot \text{NA})^2}{(0.73M\lambda)^2}. \quad (1.1)$$

A few microscope objectives' SBPs are calculated and shown in Table 1.1. As the NA of the objective lens increases, aberration correction becomes harder, making the SBP of the objective lens smaller.

Objective (M/NA/ F.N.)	**Resolution** (λ=532 nm)	**SBP** (megapixels)
1.25×/0.04/26.5	9709 nm	15.0 MP
2×/0.08/26.5	4855 nm	23.4 MP
4×/0.16/26.5	2427 nm	23.4 MP
10×/0.3/26.5	1295 nm	13.2 MP
20×/0.5/26.5	777 nm	9.1 MP
40×/0.75/26.5	518 nm	5.1MP
60×/0.9/26.5	432 nm	3.3 MP
100×/1.3/26.5	299 nm	2.5 MP

Table 1.1: SBP values for several Olympus microscope objectives

1.2 Limitation of Conventional Microscope System

- **Limited SBP**

The limited SBP restricts a lot of applications of the conventional microscope. Because of the compromise between resolution and FOV, the user has to switch back and forth between low NA large FOV objective and high NA small FOV objective in the examination of sample, or a complicated mechanical scanning system has to be used in applications that require high throughput.

- **Uncorrected Aberration**

The SBP calculation is made under the assumption of a well-corrected aberration over the entire FOV (diffraction limited resolution). However, in the use of a conventional microscope, we observed uncorrected aberration which degrades the image performance. Moreover, the uncorrected aberration becomes severer at the edge of the FOV, making the effective SBP of the microscope much lower than the nominal value. More analysis on uncorrected aberration is elaborated in Chapters 3 and 4.

- **Loss of phase information**

Because both human eyes and opto-electronic detectors are not sensitive to the phase of e-field, the phase information of sample is lost in observation. Different imaging schemes such as Zernike phase or DIC can convert phase variation into intensity distribution. However, the conversion is not linear and the phase will mix with the intrinsic intensity distribution, preventing the detection of quantitative phase information from the sample.

- **Loss of 3D information**

When imaging a thick 3-dimensional sample, the in-focus plane of the sample will be recorded as a clear image. At the same time, the out-of-focus plane of the sample will generate a blurred image added on the clear image. The results are: 1) the in-focus plane information cannot be easily distinguished from the blurred information coming from other planes, and 2) to examine information at a different plane, mechanical scanning in the depth direction is required.

1.3 Computational Microscopy System

The limitation of the conventional microscope system has restricted its applications. Recently, the advancement a few key technologies are changing the game: 1) large pixel count, high frame rate, and low noise digital array light detectors (CCD and CMOS) are easily accessible; 2) the computation power of the computer is improving exponentially; 3) novel illumination methods such as LD and LED are cheaper and more compact. These advancements led to the prosperity of computational microscopy, where advanced illumination schemes can be designed, transient phenomena can be recorded, and information can be processed to generate high quality images of microscopic sample. A few of these examples in computational microscopy include digital holography, structure light illumination, aperture coding, etc.

In this thesis, the work of Fourier ptychography(FP) technique, which is one of the computational microscopy techniques benefiting from these game changing technologies, is presented. This technique untangles the compromise between FOV and resolution, provides quantitative phase measurement, characterizes and corrects residual aberration, and can be modified to deal with 3-dimensional sample. In Chapter 2, the principle of FP is explained. In Chapter 3, a Fourier ptychographic

microscopy (FPM) system is built by LED matrix illumination, and gigapixel amplitude + phase imaging capability is demonstrated. In Chapter 4, an improvement of FPM is made which leads to the characterization and correction of microscope aberration. Chapter 5 reports the effort of building an oil-free FPM system with numerical aperture over unity and resolution power of 330nm. Chapter 6 presents aperture scanning FPM, which is a different scheme to implement the FP technique that can deal with 3-dimensional samples.

Chapter 2

FOURIER PTYCHOGRAPHY

Fourier ptychography is a computational imaging technique which combines ideas from synthetic aperture and translational-diversity phase retrieval. The word ptychography was derived from the Greek words *ptyché* (fold) and *gráphein* (to write), coined by Hoppe and Hegerl in the early 1970s to describe a newly invented coherent diffractive imaging technique [6]. Unlike holographic imaging techniques which requires a stable reference wave, ptychography uses diffraction interference occurring in the object itself. Moreover, ptychography calculates the phase relationship from magnitude-only measurement of the diffracted field. For a more comprehensive description of ptychographic imaging technique, readers can refer to a review written by J. M. Rodenburg [7].

Fourier ptychography, as the name implies, is a Fourier domain counterpart of the conventional ptychography. In this case, all the sampling, tiling, and phase retrieval are operated in the spatial frequency domain. There are two key components in this technique: 1) In the image acquisition process, transverse-translationally diversified Fourier domain measurements of the sample are carried out. One main method to provide the measurements is through angularly varying illumination. 2) In the reconstruction process, the measurements are inputted into a phase retrieval algorithm to stitch all the information together in the Fourier domain. Meanwhile, the algorithm recovers the phase information from the intensity-only measurements. There are different modalities to realize transverse-translationally diversified Fourier domain measurements and different methods for phase retrieval, which will be covered in the following chapters. In this chapter, the basic mathmatical model and the fundamental method for measurement and reconstruction will be explained.

2.1 Acquisition Process

As has been mentioned in Chapter 1, under a coherent illumination, the microscope system can be modeled as a spatial frequency low-pass filter for the sample's e-field (electromagnetic field) distribution. Therefore, the resolution limit of a single microscope image can be characterized by the pupil function of the imaging system, which is the coherent transfer function (CTF) in this case. The pupil function of an aberration-free infinity-corrected objective lens is given by the geometric shape

of its aperture [3]. Typically, the aperture of an objective lens is a circle. Thus, the pupil function in our microscope model will remain a circular low pass filter. This filter's cutoff spatial frequency, k_c, is defined by the lens's numerical aperture, $\mathrm{NA}_{\mathrm{obj}}$, and the illumination wavelength λ: $k_c = 2\pi \cdot \mathrm{NA}_{\mathrm{obj}}/\lambda$. In conclusion, the pupil function $P(k_x, k_y)$ can be described as:

$$P(k_x, k_y) = \begin{cases} 1 & \text{if } (k_x^2 + k_y^2) \leq k_c^2 \\ 0 & \text{if } (k_x^2 + k_y^2) > k_c^2, \end{cases} \tag{2.1}$$

where k_x, k_y are the coordinates in the spatial frequency domain. When a thin sample $s(x, y)$ is illuminated by a quasi-monochromatic plane wave with wavevector $\mathbf{u}_n = (k_{xn}, k_{yn})$, the exit light wave from the sample can be written as $e(\mathbf{r}) = s(\mathbf{r}) \exp(i\mathbf{u}_n \cdot \mathbf{r})$. Here we define $\mathbf{r} = (x, y)$ as the coordinate in the spatial domain and $\mathbf{u} = (k_x, k_y)$ as the coordinate in the spatial frequency domain. This e-field is first propagated to the Fourier plane and multiplied by the pupil function $P(\mathbf{u})$ of the objective lens, and then propagated to the image plane, which is an inverse Fourier transform process: $e_2(\mathbf{r}) = \mathcal{F}^{-1}\left(\mathcal{F}(e(\mathbf{r})) * P(\mathbf{u})\right)$. If we define $S(\mathbf{u}) = \mathcal{F}(s(\mathbf{r}))$ as the Fourier spectrum of the sample, $\mathcal{F}(e(\mathbf{r})) = S(\mathbf{u} - \mathbf{u}_n)$ due to the frequency-shift property of Fourier transform. The propagated e-field equation can be simplified as:

$$e_2(r) = \mathcal{F}^{-1}\left(S(\mathbf{u} - \mathbf{u}_n) * P(\mathbf{u})\right). \tag{2.2}$$

From Eq. 2.2, we can see that although the cutoff frequency of the objective lens is determined by $\mathrm{NA}_{\mathrm{obj}}$, spatial frequency information higher than the cutoff can pass the imaging system with modulation by oblique angle illumination. The high spatial frequency information carried by oblique angle illumination is the key to reconstruct a high resolution image.

Because optical camera is only sensitive to the intensity distribution of the e-field, the image recorded with illumination wavevector $\mathbf{u}_n$ is:

$$I_{\mathbf{u}_n} = |\mathcal{F}^{-1}(S(\mathbf{u} - \mathbf{u}_n) * P(\mathbf{u}))|^2. \tag{2.3}$$

To sum up, in the image acquisition process, a stack of N images $\{I_{\mathbf{u}_0}, I_{\mathbf{u}_1}, \ldots I_{\mathbf{u}_{N-1}}\}$ are captured with N different illumination, which samples different areas of the

sample's Fourier spectrum. These images are stitched together in the reconstruction process by putting the Fourier spectrum information back to its corresponding position.

2.2 Reconstruction Process

The goal of the reconstruction process is to recover complex (amplitude and phase) sample Fourier spectrum $S(\mathbf{u})$ from the stack of intensity measurements $\{I_{\mathbf{u}_N}\}$. This problem can be categorized as a phase retrieval problem, which has been studied for decades for applications such as electron microscopy, wavefront sensing, astronomy, crystallography, and in other fields that wish to recover phase while only intensity measurements can be made [8]. To be more specific, in this case, this problem is a phase retrieval problem with transverse-translationally diversified measurements [9] provided by angularly varying illumination.

The most popular method that is used to solve this problem is the iterative phase retrieval algorithm. The algorithm iteratively propagates the intermediate result between planes with constraints, and updates the intermediate result gradually using these constraints. In our case, the planes are spatial domain and Fourier domain, and the constraints are measurements and a priori knowledge of the system. The process of the algorithm is described as follows:

In the initialization step, an initial guess of the sample's Fourier spectrum $S_0(\mathbf{u})$ is set. The initial guess can be the Fourier transform of one frame of up-sampled low-resolution image, or a Dirac delta function at the origin representing uniform distribution in the space domain.

In the iterative reconstruction step, all the captured images are addressed in a sequence $\{I_{\mathbf{u}_N}\}$, and considered in turn to update the sample Fourier spectrum, as shown in Fig. 2.1 on the left. This iterative engine contains two layers of loop. The inner layer loops over all the intensity measurements to update $S(\mathbf{u})$, and the outer layer repeats the updating process until exit criteria is satisfied. The exit criteria can be the change of $S(\mathbf{u})$ within this loop being smaller than a certain value, or a certain number of loops being executed.

For the updating step which is the core of iterative phase retrieval algorithm, different updating schemes are proposed. One of the most broadly used ones is the Gerchberg-Saxton algorithm [10, 11], and the steps are shown in Fig. 2.1 on the right. For the nth update using image $I_{\mathbf{u}_n}$, the region corresponding to illumination $\mathbf{u}_n$ is extracted and inverse Fourier transformed to simulate a captured image. Then the

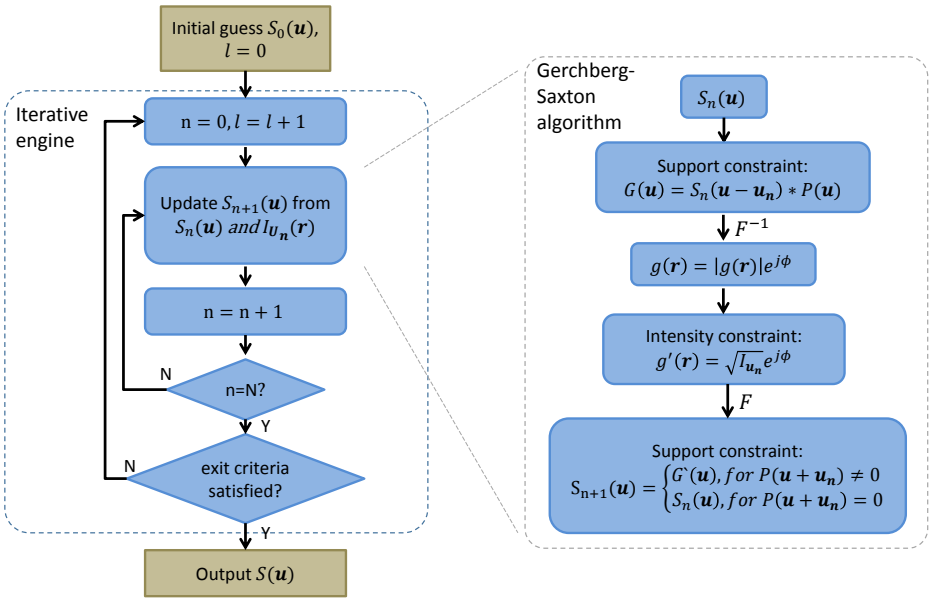

Figure 2.1: Iterative phase retrieval algorithm with Gerchberg-Saxton type update function.

'intensity constraint' is applied on the simulated image by replacing the amplitude with the square root of the real captured image. This modified simulated image is Fourier transformed back to spatial frequency domain and is used to update the sample's Fourier spectrum. In this method, the 'support constraint' is applied and the region corresponding to illumination vector $\mathbf{u}_n$ is replaced by the Fourier transform of the 'intensity-constrained' simulated image.

Although there is no explicit error metric for GS type phase retrieval algorithm, it has been argued that they end up minimizing the sum of the squared difference between simulated and measured amplitude [8, 12]:

$$\min_{s(\mathbf{u})} f(S(\mathbf{u})) = \sum_{n} \sum_{\mathbf{r}} \left| \sqrt{I_{\mathbf{u}_n}(\mathbf{r})} - \left| \mathcal{F}^{-1}\{S(\mathbf{u} - \mathbf{u}_n)P(\mathbf{u})\} \right| \right|^2, \ s.t.\ I_{\mathbf{u}_n}(r),\ P(u). \tag{2.4}$$

Besides the GS type phase retrieval algorithm, there are other methods raised to update $S_{n+1}(\mathbf{u})$ which are designed to make the algorithm converge faster. These algorithms include the gradient descending method, which we will mention in Chapter 4, the input-output algorithm, etc. There are also non-iterative phase retreival methods. In Ref. [13], a convex formulation of the ptychography problem is proposed and a low-rank factorization based algorithm is used to solve the problem.

One more thing to point out here is that the phase retrieval method is not a global minimizer for the optimization problem mentioned in Eq. 2.4. However, for a natural sample, with a proper initial guess and adequate measurements with overlapping in the spectrum domain, the solution falls towards ground truth value with a high probability. Practically, it has been shown experimentally that the RMS errors decrease as the spectrum overlapping percentage increases, and a minimum of 35% overlapping percentage is needed for a successful FP reconstruction [14]. In real experiment, 60% of overlapping is used in the design of illumination and 10 iterations of the algorithm is carried out to ensure convergence.

2.3 Performance Analysis

Resolution enhancement

As been analyzed by the previous section, the high spatial frequency information of the sample that is beyond the cutoff frequency of the objective lens is captured and placed back to its corresponding place by using Fourier ptychography. As a result, an expended Fourier spectrum of the sample is acquired, and thus a higher resolution imaging system is achieved. This sub-session analyzes the enhancement of resolution quantitatively.

In a microscope system, when the sample $s(\mathbf{r})$ is illuminated by normal incident plane wave, the highest spatial frequency of the sample $k_s = \sqrt{k_{xs}^2 + k_{ys}^2}$ that can pass the imaging system is determined by the lens's cutoff frequency k_c (Fig. 2.2, right). Thus the CTF defines the image spatial frequency support as $[-k_c, k_c]$.

In the case of oblique angle illumination, we define the illumination wavevector as $k_i = \frac{2\pi}{\lambda} n_{illu} \sin\phi = \sqrt{k_x^2 + k_y^2}$, where n_{illu} is the refractive index of the medium separating the illuminator and the sample, and ϕ is the angle between the wavevector and the optical axis. As been mentioned in the previous section, the Fourier spectrum of the exit wave will be a shifted version of the sample's Fourier spectrum: $\mathcal{F}(e(\mathbf{r})) = S(\mathbf{u} - \mathbf{u}_n)$. Because of this shift, a different range (i.e., support) of the sample spectrum will now pass through the fixed lens CTF to the image sensor. Now in the off-axis case the CTF defines a shifted spatial frequency support as $[-k_i - k_c, -k_i + k_c]$.

FP repeats this shift-and-capture imaging process for N different illumination, extending to a maximum off-axis angle of ϕ_{max}. After data capture, FP has thus acquired N images, each originating from a distinct spatial frequency support. A phase retrieval algorithm is used to digitally fuse all N captured spatial frequency

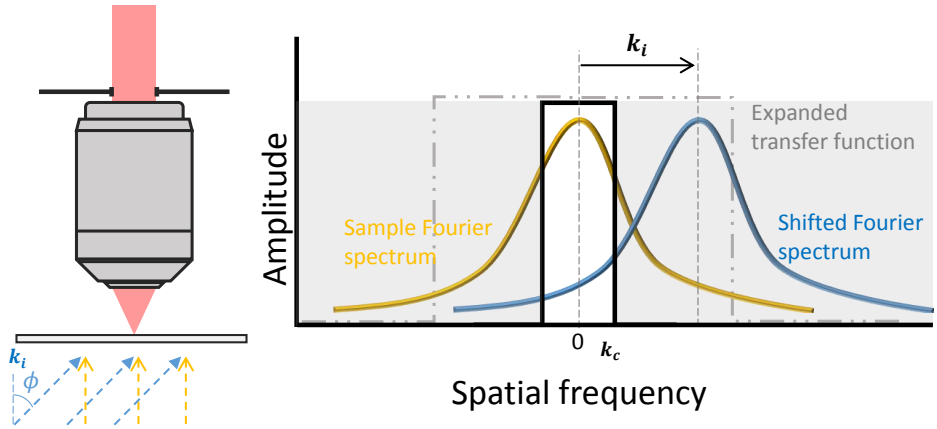

Figure 2.2: Principle of Fourier ptychrography. The CTF of the microscope objective is a low pass filter with cutoff frequency k_c. When the sample is illuminated by normal incident plane wave (yellow line), the spatial frequency of the sample in the range $[-k_c, k_c]$ passes through the CTF to form an image. Illuminating the sample with a tilted plane wave with wavevector k_i (blue line) shifts the sample spectrum. The CTF now defines the image's spatial frequency support as $[-k_i - k_c, -k_i + k_c]$. After image capture, a phase retrieval algorithm stitches together the spatial frequency information from the unique support of each image. The resulting FP reconstruction is expected to exhibit a cutoff frequency of $k_{max} + k_c$, corresponding to an expanded system NA, $\mathrm{NA}_{\mathrm{sys}} = \mathrm{NA}_{\mathrm{obj}} + \mathrm{NA}_{\mathrm{illu}}$.

supports together. The final resulting spectrum will thus lie within a contiguous spatial frequency window $[-(k_c + k_{max}), k_c + k_{max}]$, where $k_{max} = \frac{2\pi}{\lambda} n_{illu} \sin \phi_{max}$ is the illumination wave vector from the maximum off-axis angle. If we define $\mathrm{NA}_{\mathrm{illu}} = \frac{k_{max}}{2\pi/\lambda} = n_{illu} \sin \phi_{max}$ as the illumination NA, the synthesized NA (i.e., $\mathrm{NA}_{\mathrm{sys}}$) of the FPM system is given by:

$$\mathrm{NA}_{\mathrm{sys}} = \mathrm{NA}_{\mathrm{obj}} + \mathrm{NA}_{\mathrm{illu}}. \tag{2.5}$$

This system NA is analogous to the resulting NA of synthetic aperture setups. [15–23]. Unlike a true synthetic aperture, FP does not measure the phase of each shifted optical field at either the aperture plane or the image plane. Its unique phase retrieval procedure instead allows us to stitch together each shifted spatial frequency window when only the resulting intensities at the image plane are known.

Phase Imaging Capability

Since the phase retrieval algorithm reconstructs the complex Fourier spectrum $S(\mathbf{u})$ of the sample, the complex spatial distribution of the sample is also recon-

structed. In other words, the phase of the sample is reconstructed from intensity-only measurements.

There is a long history of using the phase retrieval algorithm to seek a complex field solution that is consistent with measurements of its intensity. In its original form, only one intensity measurement was used, and the Gerchberg-Saxton algorithm [10, 11], as well as its related error reduction algorithm [8], was used to solve this type of problem. Although this form of phase retrieval algorithm works well for many cases of interest, stagnation and ambiguity problems are known to prevent strict convergence.

Later on, a technique termed phase diversity has been developed to overcome these limitations. This technique relies on measuring multiple intensity patterns with a known modification to the optical setup applied between each measurement. Methods to provide phase diversity include transverse-translationally diversified measurement [9] (used in FP), defocus variation [24] (used in Chapter 3 for aberration estimation), etc [25–27]. The set of captured images, along with the knowledge of the diversity function, is then used to iteratively converge to a complex field that agrees with each measurement. Stagnation and ambiguity problems are overcome by providing a set of measurements that more robustly constrain the phase retrieval process. Increased accuracy is guaranteed through an analysis of its Cramer-Rao lower bound [28].

The capability to measure phase is preferable for many applications, such as observation of unstained tissue, cell culture monitoring, etc. In the following chapters, an experimental verification of the quantitative phase measurement capability will be presented and more implementations of the phase information such as digital refocusing and aberration correction will be demonstrated.

Chapter 3

FOURIER PTYCHOGRAPHIC MICROSCOPY WITH LED MATRIX ILLUMINATOR

3.1 Microscopy System Setup

A prototype of Fourier Ptychographic microscopy (**FPM**) system is built, as shown in Fig. 3.1 (a). The system consists of an upright microscope (Olympus BX61) with a 2X 0.08NA objective lens (Olympus 2X PlanApo), a Prosilica GX6600 (CCD: Kodak KAI-29050, sensor size: 36.2 mm × 24.1 mm, Pixel size: 5.5μm, 28.8MPixel) with coverage over the full FOV of the objective lens, and an LED matrix (Adafruit, 4mm spacing, controlled by an Arduino) to provide angularly varying illumination.

As shown in the inlet of Fig. 3.1, each LED element has a red, green, and blue chip which can be lit up separately. The lit up area of each color is 200μm, and the LED panel is placed at 80mm away from the sample. Since the matrix is far away from the sample, each LED provides close-to-plane-wave illumination for a small area of the sample. The wavevector (k_x, k_y) corresponding to the illumination can be calculated using simple geometry. For all following experiments, red channel LEDs, if not specified, are used when we capture monochromatic images. Red, green, and blue LEDs are used separately to reconstruct red, green, and blue images. These three images are combined when we capture color images.

In the experiment, 15x15 red LED are lit up sequentially (center LED right on optical axis) and 225 images are captured. The overlap between two images is 70%, satisfying the requirement of phase retrieval algorithm. All the captured data is fed into the phase retrieval algorithm to reconstruct a high resolution image.

3.2 Resolution Enhancement

As been shown in Eq. 2.5, an FPM system has a system NA equal to the summation of objective NA and illumination NA. In this case, the LED has a pitch of 4mm, and is placed 80mm beneath the sample. The edge LED provides an illumination NA of $\sin(\arctan(\frac{7*4}{80})) = 0.33$. The objective NA is 0.08, so the system NA equals 0.41, which is 5 times NA improvement compared to the original microscope.

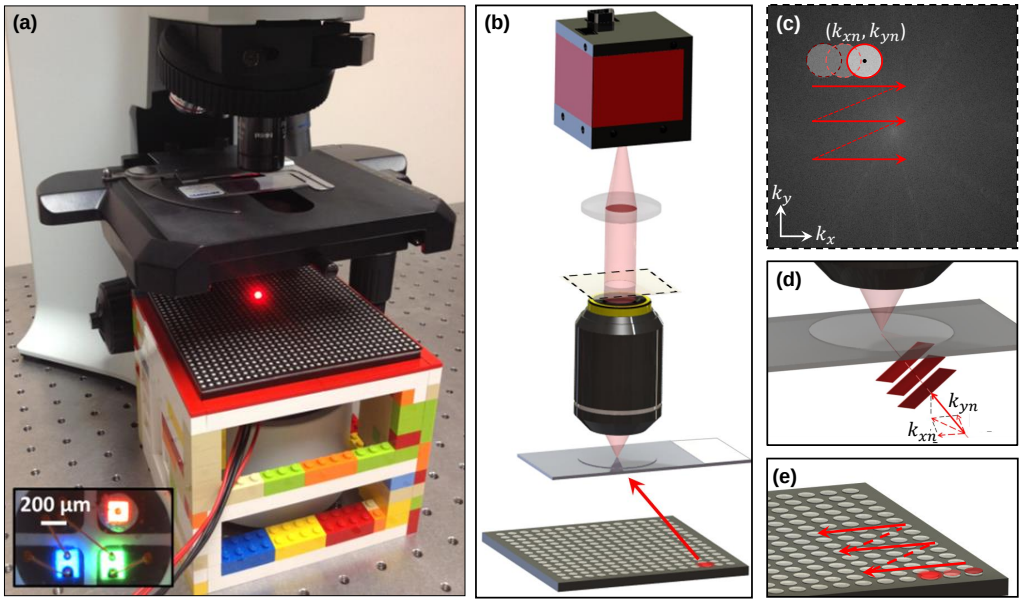

Figure 3.1: FPM system schematic. (a) FPM system is built by substituting the original lightsource with an LED matrix. (b) Schematic with key optical elements. (c) The object's finite spatial frequency support, defined by the microscope's NA in the Fourier domain (red circle), is imposed at offset locations to reflect each unique LED illumination angle. The Fourier transform of many shifted low-resolution measurements (each circle) is stitched together to extend the complex sample spectrum's resolution well beyond the objective lens's cutoff. (d) Light emitted from a single LED strikes a small sample area with wavevector (k_{xi}, k_{yi}). (e) LEDs are sequentially activated during FPM image acquisition.

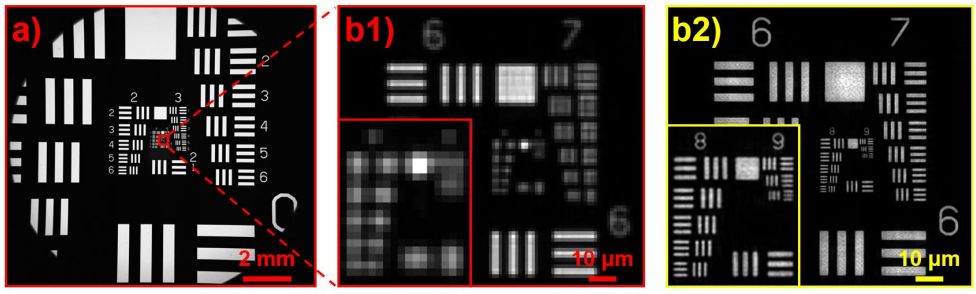

Figure 3.2: FPM image of USAF resolution target. (a) Full FOV image using a 2X objective; (b1) segment of image with normal illumination; (b2) resolution enhanced by FPM method.

To demonstrate the resolution improvement, a 1951 US Air Force (USAF) resolution target is used as a sample. The images are shown in Fig. 3.2. With one LED lit up, corresponding to coherent imaging of the original imaging sytem, group 7, element 1 can be resolved (period=7.81μm). With FPM, group 9 element 3 (period=1.55μm) can be resolved, which matches the theoretical resolution prediction: $r = \frac{\lambda}{\mathrm{NA}_{\mathrm{sys}}} = 1.58\mu\mathrm{m}$.

3.3 Quantitative Phase

To verify FPM's capability to accurately recover optical phase, we image a sample containing microspheres in oil (3μm and 6.5μm diameter, n_{oil} = 1.48, n_{sphere} = 1.6), shown in Fig. 3.3(a1-a3). Unwrapped line traces of the optical phase shift induced by two different-sized spheres lead to estimated microsphere thickness curves in Fig. 3.3(c1)-(c2), exhibiting close agreement with theory. The root mean-squared errors (RMSEs) between experimental and theoretical thickness are 0.25 μm and 0.33 μm, respectively.

A phase-shifting digital holography (DH) microscope is also used to provide experimental ground-truth comparison. Our DH setup splits a solid-state 532 nm laser into a sample and reference arm (both spatially filtered and collimated). The reference arm passes through an electro-optic phase modulator (Thorlabs EO-PM-NR-C1) before recombination with the sample beam for imaging (Prosilica GX 1920, 4.54 μm pixels) via an objective (40×, 0.65 NA Nikon Plan N) and tube lens. Four images are captured with a $\pi/2$ phase shift added to the reference between each image. Sample phase is calculated from the four images via the phase recovery equation [29]. RMSEs of 0.41 μm and 0.30 μm for the 3 μm and 6.5 μm line traces also offer close agreement between the DH experimental measurements and theory.

Fig. 3.3(b2) presents an FPM reconstruction of a complex biological sample – a human blood smear immersed in oil, a common quantitative phase measurement target [30]. The FPM and ground-truth DH phase (Fig. 3.3(b3)) maps closely match, as exhibited by the phase trace through a red blood cell in Fig. 3.3(c3) (RMSE = 0.58 μm). Sources of error for the FPM setup include the inclusion of slight aberrations by the objective lens, effects of a partially coherent illumination source, and the influence of noise within the iterative reconstruction scheme. The primary source of error in the DH data is speckle "noise" caused by a coherent illumination source. FPM phase tends towards a smoother phase profile in part because its LEDs' partially coherent illumination avoids coherent speckle artifacts.

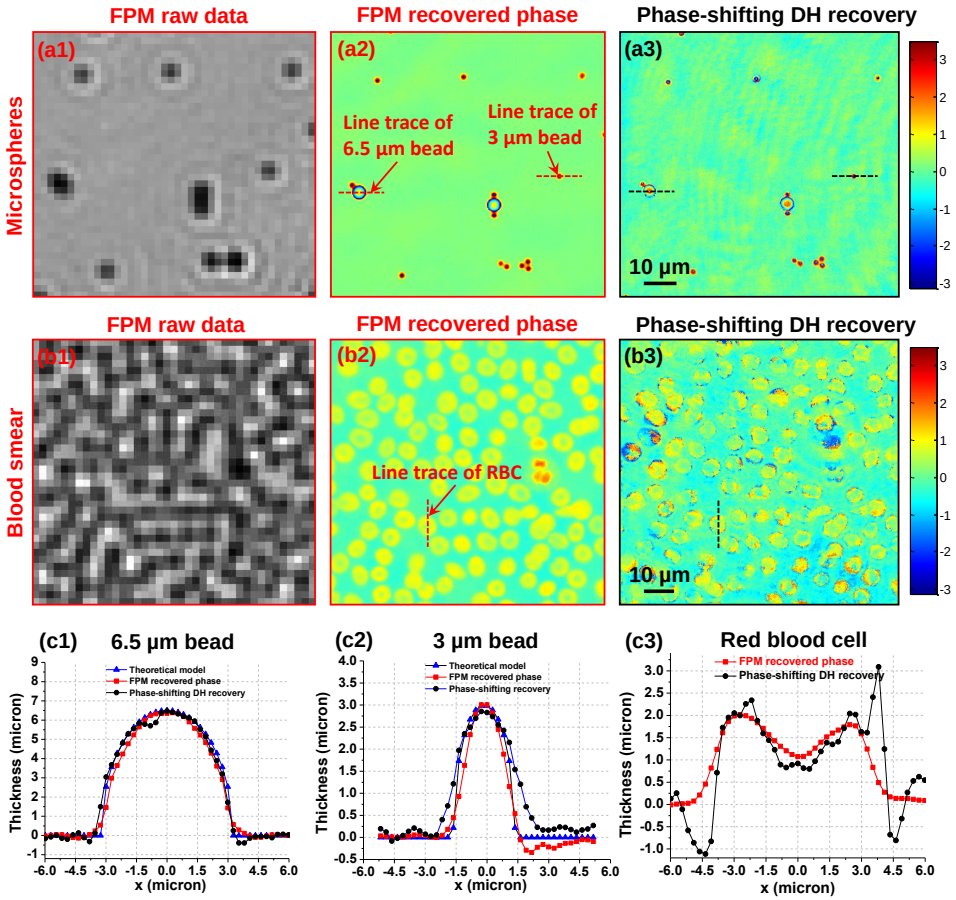

Figure 3.3: Comparing FPM phase reconstructions to digital holographic and theoretical data. FPM transforms low-resolution intensity images from a 2X objective (a1) into a high-resolution phase map (a2) of different-sized polystyrene microbeads, as compared with a DH reconstruction (a3) using a 40X objective. (b) A similar image sequence highlights FPM's phase imaging capabilities on a human blood smear. (c) Line traces through the microbeads and a RBC demonstrate quantitative agreement with expected phase performance.

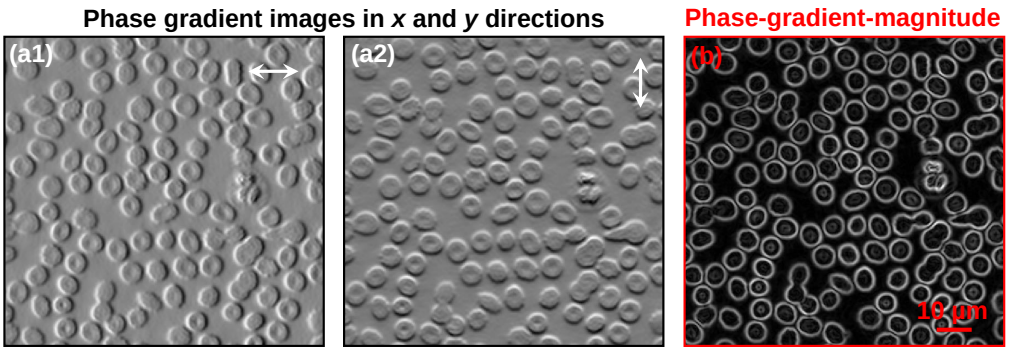

Figure 3.4: Computed phase gradient images in x direction (a) and y direction (b), and phase gradient magnitude image (c) from the human blood smear phase map in Fig. 3.

A simple one-dimensional model helps describe limitations on the resolution of FPM's acquired phase image. From [31, 32], we know FPM's maximum resolvable wavevector k_x is limited by its maximum LED angle θ: $k_x^{max} = k(sin\theta + \text{NA})$. Likewise, the wavevectors emitted by a slowly varying phase object $\phi(x)$ are set by its gradient: $k_x^{max} = d\phi/dx$ in 1D. Assuming the phase object is a grating of period p and thickness t, we can write $\phi(x) = t\sin(px)$. Using the above gradient relationship tells us its maximum emitted wavevector $k_x^{max} = tp$. Thus, the resolution limit for the FPM phase is set by the product of the sample's spatial resolution and thickness, which both must be accounted for during system design. This argument extends to an arbitrary extended complex sample by Fourier-decomposing it into a finite set of gratings. While this relationship helped guide the design of the included experiments, a more detailed analysis is worth future investigation.

The benefits of an acquired phase map are easily demonstrated with the computational generation of phase-gradient images in Fig. 3.4, simulating the improved visibility of a differential-interference-contrast microscopy. However, we note that this computational processing does not produce new information for the complex sample. Fig. 3.5 demonstrates how an acquired FPM phase map can give additional sample information otherwise absent from FPM's improved intensity resolution image.

3.4 Gigapixel Imaging

By the implementation of Fourier ptychography on the 2X 0.08 NA microscope system, the resolution is enhanced fourfold. Because of the quantitative phase reconstruction capability of FP, the residual aberration over the entire FOV

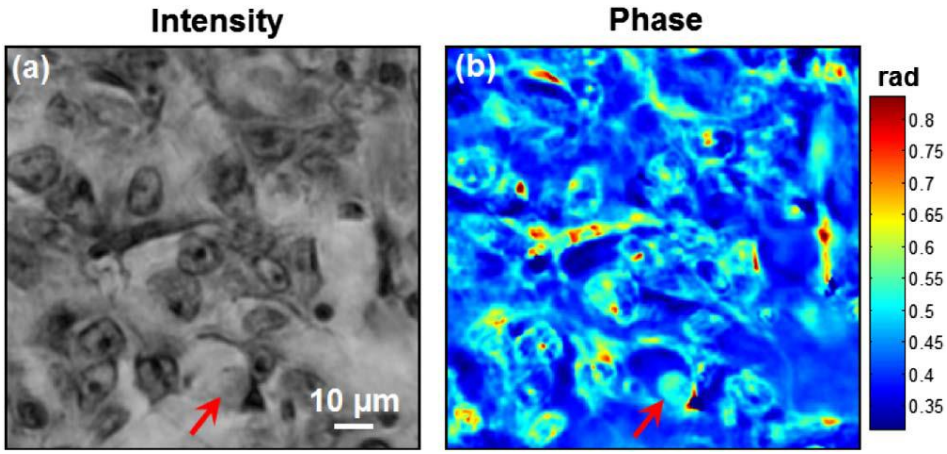

Figure 3.5: FPM intensity and phase images of a tissue sample. As indicated by the red arrow, some cell features are transparent in the intensity image but visible in the phase image.

can be removed by a digital wavefront-correction method and diffraction-limited resolution given by NA_{sys} can be achieved over the entire FOV. Thanks to these two achievements, the FPM system can be used to generate gigapixel images of samples.

Digital Wavefront Correction

Although the FPM method does not require phase information as an input, its operation implicitly accommodates phase during iterative reconstruction. We demonstrate in this section that the depth-of-focus of our FPM prototype can be significantly extended beyond that of the employed objective lens, using a numerical strategy to compensate for aberrations in the pupil function [33, 34].

This digital correction process, as shown in Fig. 3.6, is inspired by similar wavefront correction concepts in adaptive optics [35]. The basic idea is to digitally introduce a phase map to our coherent optical transfer function to compensate for aberrations at the pupil plane during the iterative image reconstruction process. The FPM algorithm incorporates this compensation into two additional multiplication steps (steps 2 and 5 in Fig. 3.6(a) and (b)). Specifically, step 2 models the connection between the actual sample profile and the captured intensity data (with included aberrations) through multiplication with a pupil function $e^{i\cdot\varphi(k_x,k_y)}$, whereas step 5 inverts such a connection to achieve an aberration-free reconstructed image. Sample defocus is essentially equivalent to introducing a second-order Zernike mode, or a quadratic phase factor, to the pupil plane (i.e., a defocus aberration [36]):

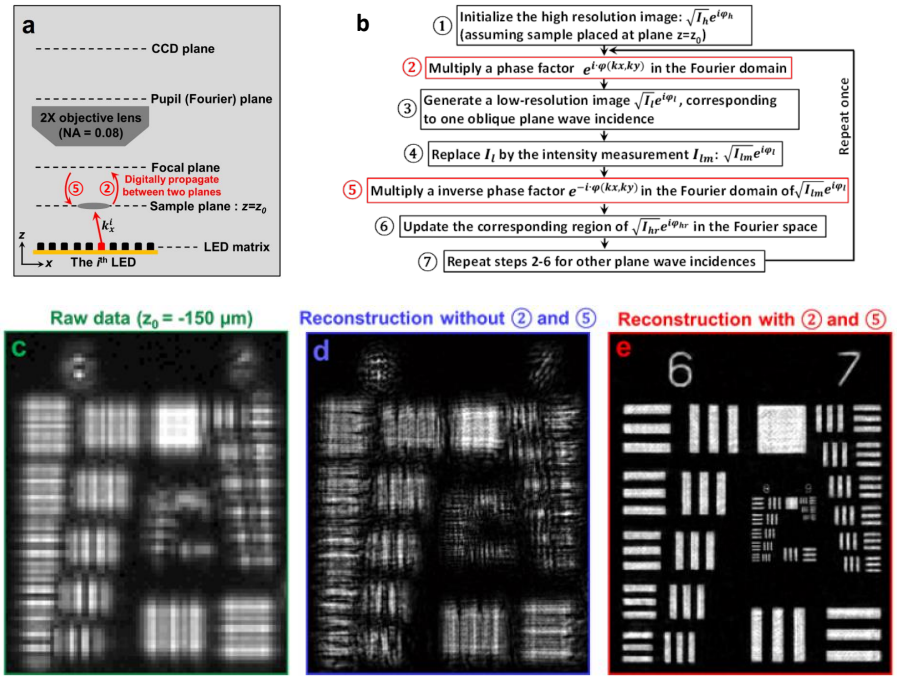

Figure 3.6: Extending depth-of-focus with digital wavefront correction. (a) The principle of FPM's digital wavefront correction technique. A digital pupil function is introduced in steps 2 and 5 to model the connection between the actual sample profile and the captured intensity data, which may exhibit aberrations caused by defocus. (b) Diagram of FPM's iterative recovery algorithm with the addition of digital wavefront correction. (c) One raw low-resolution image of the USAF target placed at $z_0 = -150\mu$m. High-resolution FPM reconstructions without (d) and with (e) steps 2 and 5 added to the iterative recovery procedure.

$$e^{i\cdot\varphi(k_x,k_y)} = \begin{cases} e^{i\sqrt{k_0^2-k_x^2-k_y^2}\cdot z_0} & \text{if } (k_x^2+k_y^2) \le k_c^2 \\ 0 & \text{if } (k_x^2+k_y^2) > k_c^2, \end{cases} \tag{3.1}$$

where $k_0 = 2\pi/\lambda$ is the wavevector, k_x and k_y are the wave numbers at the pupil plane, z_0 is the defocus distance, and $k_c = k_0 \cdot \mathrm{NA}$ is the objective's cutoff spatial frequency.

Fig. 3.6(c-e) experimentally demonstrates FPM's ability to fully resolve an object given a set of intensity images defocused by 150 μm. The significance of wavefront correction is made clear by comparing reconstruction results without (Fig. 3.6(d)) or with (Fig. 3.6(e)) digital addition of a defocused pupil. We note that, in Fig. 3.6(e), the defocus distance is known a priori. If the defocus distance is unknown, we can digitally adjust the 'z' parameter to different values, reconstruct the

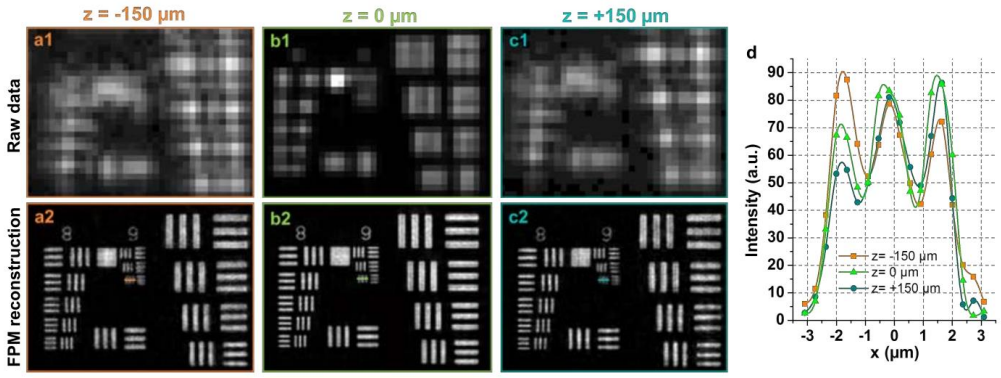

Figure 3.7: Correcting aberrations with digital wavefront correction, experiment. (a1)-(c1) Low-resolution raw data of our USAF resolution target, each corresponding to different defocused distances (-150 μm to 150 μm). (a2)-(c2) FPM's high-resolution image reconstructions using digital wavefront correction. (d) Line traces for the smallest features in (a2)-(c2), with a minimum contrast difference of 30%.

corresponding FPM images, and pick the sharpest image through observation or by a computer algorithm [37]. This approach can also be extended to image a tilted or uneven sample [38]. In this case, we can digitally adjust the 'z' parameter to achieve acuity for each region of the whole image and combine the in-focus regions to form a fully focused image of the tilted sample. From Fig. 3.6, we conclude that our FPM prototype can achieve a resolution-invariant depth-of-focus of approximately 0.3 mm with digital wavefront correction. This point is further validated in Fig. 3.7. In contrast, the natural depth-of-focus of the employed 2x objective lens (0.08 NA) is approximately 80 μm. The improvement is even more remarkable if compared to an objective lens with a resolution-matching 0.5 NA, where the FPM prototype's 0.3 mm depth-of-focus offers an approximate factor of improvement of 75.

Finally, we note that alternate digital multiplicative phase factors can be included in steps 2 and 5 to correct for a variety of aberrations, as long as they correctly model the employed optics. Following this strategy, we characterize and correct higher order aberrations of our prototype's objective lens in the following section.

Spatially-varying-aberration Characterization and Correction

For characterizing residual aberrations which are spatially varying, the microscope's FOV is divided into small tiles within each of which aberrations can be considered as constant. For each tile, a phase retrieval approach based on defocus variation is used to calibrate the aberrated wavefront. Then we apply a generalized pattern search (GPS) method [39], a nonlinear optimization algorithm, to recover

aberration parameters at 350 different spatial locations over the entire FOV. These parameters are used to generate 2D aberration maps by parameter fitting. This recovered aberration map is plugged into the digital wavefront correction algorithm described in the previous section to reconstruct aberration-free images.

- **Phase retrieval and defocus diversity**

The first concept essential to our work is the application of the phase retrieval algorithm using defocus diversity. Similar to the phase retrieval algorithm for FP which uses transverse-translationally diversified intensity measurements to recover lost phase information, this technique relies on measuring multiple intensity patterns with a known modification (defocus) to the optical setup applied between each measurement.

In the implementation, two or more images must be captured with known defocus distances, as shown in Fig. 3.8(a). Based on these intensity measurements I(s) (s= -2, -1, 0, 1, 2 in Fig. 3.8(a)) at different defocus planes, we follow the multi-plane iterative algorithm outlined in Fig. 3.8(b) [24]. In this algorithm, we first initialize a complex estimate of the object function. This complex estimate is then propagated to one defocus plane (multiplication by a quadratic phase factor in the Fourier domain [3]). After propagation, the amplitude of the estimate is replaced by the square root of the corresponding measurement I(s), while the phase is kept unchanged. Such a propagate-and-replace process is repeated until the complex solution converges. (see section 'Off-axis pupil function recovery' for implementation details)

- **Spatially varying pupil aberrations**

Second, an understanding of spatially varying pupil aberrations is important to fully appreciate the impact of this work. In an aberration-free coherent imaging system, the light field distribution at the pupil plane (i.e., the back focal plane of the objective lens) is directly proportional to the Fourier transform of the light field at the object plane. Therefore, the spatial coordinates at the object plane and the pupil plane can be expressed as (x, y) and (k_x, k_y), respectively, with k_x and k_y as the wave number in the x and y directions. Due to such a Fourier relationship, aberrations of an imaging platform are often characterized at the pupil plane for simplicity [3]. Different types of aberrations can be quantified as different Zernike modes at the

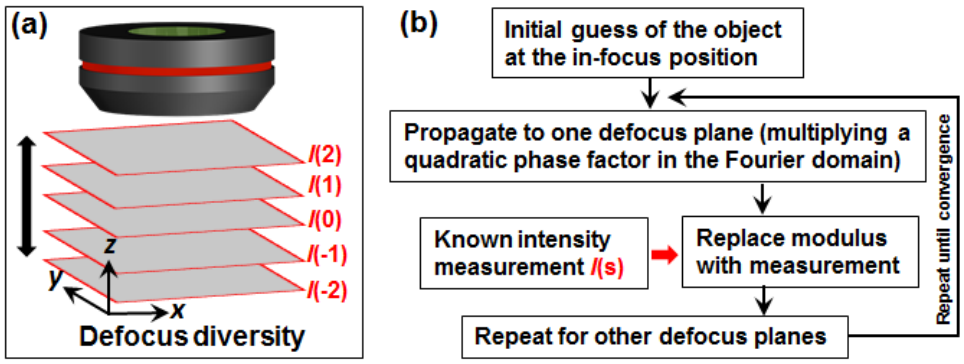

Figure 3.8: Multi-plane phase retrieval with defocus diversity. (a) Multiple intensity images I(s) (s= -2, -1, 0, 1, 2) are captured at different defocus settings. (b) Multi-plane iterative phase retrieval algorithm presented in [24].

pupil plane. For example, defocus aberration can be modeled as a phase factor $p_5 \cdot Z_2^0(k_x, k_y)$, where $Z_2^0(k_x, k_y)$ denotes the corresponding Zernike polynomial for this aberration (here a quadratic function), while coefficient p_5 denotes the amount of defocus aberration (subscript '5' indicates the fifth Zernike mode).

A more complete aberration model uses the generalized pupil function $W(k_x, k_y)$, whose phase factor is a summation of different Zernike modes with different aberration coefficients p_m (p_m denotes the amount of m^{th} Zernike mode; refer to Eq. 3.2). If the imaging platform is shift-invariant, each aberration coefficient p_m is constant over the entire imaging FOV and the generalized pupil function $W(k_x, k_y)$ is independent of spatial coordinates x and y. However, recent extreme-FOV computational imaging platforms push beyond the limits of conventional lens design and thus invalidate this shift-invariant assumption. Aberration coefficients p_ms are 2D functions of x and y in this case, and thus the generalized pupil function can be expressed as a function of both k_x, k_y and x, y, i.e., $W(k_x, k_y, x, y)$. Our goal here is to characterize the aberration parameters $p_m(m = 1, 2, \ldots)$ as a function of spatial coordinates x and y. Based on $p_m(x, y)$, we can derive the generalized pupil function $W(k_x, k_y, x, y)$ at any given spatial location and accurately perform post-detection image aberration correction using deconvolution method [40] or digital wavefront correction method in Fourier ptychography.

- **Off-axis pupil function recovery**

Assuming the aberrations of the objective lens are minimal (i.e., they are well-corrected for) at the center of its FOV, we use images of the object located near the

FOV's center to serve as the ground truth for other off-axis positions. The proposed approach for off-axis aberration characterization consists of three primary steps: 1) sample preparation, 2) phase retrieval, and 3) pupil function estimation.

1) Sample preparation. We first create a calibration "target" sample containing identical discretized objects over its full viewing area. While several convenient targets exist, we found that simply spin-coating a layer of 10μm diameter microspheres (Polysciences, Inc.) on top of a microscope slide offered an ideal calibration sample. Selecting a sparse concentration of microspheres ensures that an automated search algorithm can successfully identify each microsphere. For example, a slide that contains 350 microspheres distributed randomly over the 1.3 cm FOV associated with the 2X objective works well.

2) Phase retrieval. Following the general procedure outlined above, we displace the microscope stage from the focal plane at $\delta = 50\mu$m increments in either defocus direction, capturing a total of 17 images of the microsphere calibration target I(s), where s=(-8, ... 0, ...8). The maximum defocus distance with such a scheme is 400μm in either direction. For each image, the microsphere target is illuminated with a quasi-monochromatic collimated plane wave (632 nm).

Next, we create a 64^2-pixel cropped image set $I_c(s)$ that contains one microsphere at the center FOV (see Fig. 3.9, left). We recover the complex profile of this centered microsphere using the multi-plane phase retrieval algorithm [24], detailed briefly as follows. First, an estimate of the complex field is initialized at the object plane. The initial estimate's phase is set to a constant and its amplitude is set to the square root of the in-focus intensity measurement of the centered microsphere $I_c(0)$. Second, this complex field estimate is Fourier transformed and multiplied by a quadratic phase factor $\exp(ik_z z)$, describing defocus of the field by axial distance $z = s \cdot \delta$. To begin, we set $s = 1$, corresponding to $z = +50\mu$m of defocus. Third, after digitally defocusing, we again replace the amplitude values of the complex field estimate with the square root of the intensity data from recorded image, $I_c(s)$. Beginning with s = 1, we first use the intensity values $I_c(1)$ captured at $z = +50\mu$m for amplitude value replacement, while the estimate's phase values remain unchanged. This digital propagate-and-replace process is repeated for all values of s (all 17 cropped intensity measurements from the captured focal stack). Finally, we iterate the entire phase retrieval loop approximately 10 times. The final recovered complex image, denoted as $\sqrt{I_{truth}}e^{i\phi_{truth}}$, serves as a "ground truth" estimate of the complex field from a minimally aberrated microsphere, which may be digitally refocused to

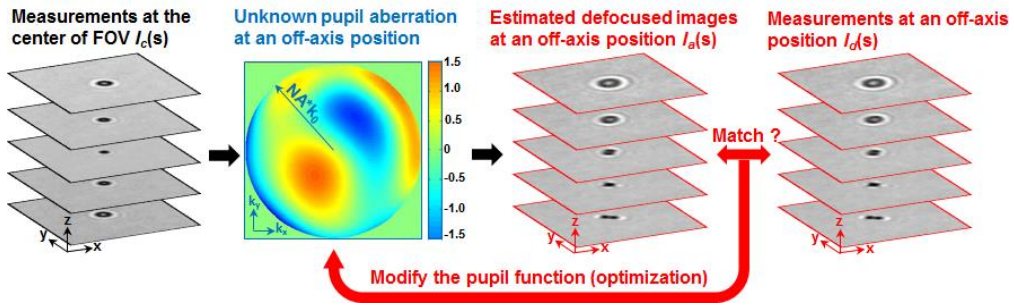

Figure 3.9: Pupil function recovery at an off-axis position. Two cropped areas of one set of defocused intensity images are used for algorithm input. One cropped set $I_c(s)$ is centered on a microsphere at the images' central FOV (left), while the other cropped set $I_d(s)$ is centered on a microsphere at an off-axis position (right). Each cropped image set contains 17 intensity measurements (here only 5 are shown) at different defocus distances (-400 μm to +400 μm, 50 μm per step). We approximate an unknown pupil function W with 8 Zernike coefficients (x-tilt, y-tilt, x-astigmatism, y-astigmatism, defocus, x-coma, y-coma, and spherical aberration). We use this pupil function estimate to modify the 17 "ground truth" images $I_c(s)$ of the central microsphere to generate a new set of aberrated intensity images, $I_a(s)$ (middle). We then adjust the values of the 8 unknown Zernike coefficients to minimize the difference between $I_a(s)$ and the actual intensity measurements of the off-axis microsphere, $I_d(s)$ (right). The corresponding pupil function described by 8 Zernike coefficients is recovered when the mean-squared error difference between these two image sets is minimized.

any position of interest.

3) Pupil function estimation at an off-axis position. Next, we select a microsphere at a position (x_0, y_0) off the optical axis and generate a new 64^2-pixel cropped image set $I_d(s)$ from our initial measurements, centered at (x_0, y_0) (see Fig. 3.9). We also initialize an estimate of the unknown location-dependent pupil function for this position, $W(k_x, k_y, x_0, y_0)$. For simplicity, we approximate the unknown pupil function $W(k_x, k_y, x_0, y_0)$ with eight Zernike modes, z_1^{-1}, z_1^1, z_2^{-2}, z_2^2, z_2^0, z_3^{-1}, z_3^1, and z_4^0, corresponding to x-tilt, y-tilt, x-astigmatism, y-astigmatism, defocus, x-coma, y-coma, and spherical aberration, respectively [41]. The point-spread function at the selected off-axis microsphere location (x_0, y_0) may be uniquely influenced by each mode above. We denote the coefficient for each Zernike mode with $p_m(x_0, y_0)$, where the subscript 'm' stands for the mode's polynomial expansion order (in our case, m = 1, 2,..., 8). With this notation, our unknown pupil function estimate $W(k_x, k_y, x_0, y_0)$ can be expressed as:

$$W(k_x, k_y, x_0, y_0) = \exp\Big\{i2\pi\big[p_1(x_0, y_0)Z_1^{-1}(k_x, k_y) + p_2(x_0, y_0)Z_1^{1}(k_x, k_y) + \ldots \\ p_3(x_0, y_0)Z_2^{-2}(k_x, k_y) + p_4(x_0, y_0)Z_2^{2}(k_x, k_y) + \ldots \\ p_5(x_0, y_0)Z_2^{0}(k_x, k_y) + p_6(x_0, y_0)Z_3^{-1}(k_x, k_y) + \ldots \\ p_7(x_0, y_0)Z_3^{1}(k_x, k_y) + p_8(x_0, y_0)Z_4^{0}(k_x, k_y)\big]\Big\}. \quad (3.2)$$

Here, each mode $p_m(x_0, y_0)$ is a space-dependent function evaluated at $(x = x_0, y = y_0)$, allowing the pupil function W to model spatially varying aberrations. This pupil function estimate is then used along with the "ground truth" complex field of the centered microsphere found in step 2 to generate a set of aberrated intensity images, $I_a(s)$, as follows:

$$I_a(s) = \left|\mathcal{F}^{-1}\left(W(k_x, k_y, x_0, y_0) \times \mathcal{F}(\sqrt{I_{truth}}e^{i\phi_{truth}}) \times e^{ik_z\delta s}\right)\right|^2, \quad (3.3)$$

where $\mathcal{F}$ is the Fourier transform operator and the term $e^{ik_z\delta s}$ represents defocus of the ground truth microsphere field to plane s. We then adjust the values of the 8 unknown Zernike coefficients p_m comprising the pupil function W to minimize the difference between this modeled set of aberrated intensity images $I_a(s)$ and the actual set intensity measurements of the selected off-axis microsphere, $I_d(s)$. The corresponding pupil function described by 8 Zernike coefficients is recovered when the mean-squared error difference is minimized. We apply a GPS algorithm [39] to solve the following nonlinear optimization problem for pupil function recovery:

$$(p_1, p_2, ..., p_8)|_{(x=x_0, y=y_0)} = \underset{(p_1, p_2, ..., p_8)}{\arg\min} \sum_{s=-8}^{8} \left(\sqrt{I_a(s)} - \sqrt{I_d(s)}\right)^2. \quad (3.4)$$

Based on these optimal Zernike coefficients, the off-axis pupil function can be approximated following Eq. 3.2. Determining the aberration function associated with one off-axis microsphere requires an approximate computation time of 90 seconds on a personal computer with an Intel i7 CPU. We note that higher-order aberrations can also be included in such an optimization process, with the cost of longer computational time (about 3-4 folds longer for one more Zernike mode).

- **Spatially varying aberration characterization over the entire FOV**

Repeating the previous section's off-axis aberration recovery scheme for many different microspheres spread over the image plane, we are able to characterize a microscope objective's spatially varying aberrations over its entire FOV. The center of each microsphere is automatically identified using a marker-controlled watershed segmentation algorithm [42]. We also measure the distance between each marked microsphere and its nearest neighbor. Any microsphere within a 150 μm radius of a neighbor is automatically skipped to avoid multiple computations at sphere clusters.

Fig. 3.10(a) shows a full FOV image of the calibration target with 350 microspheres denoted by a red dot. For each microsphere, we recover the same 8 location-specific Zernike coefficients. For example, Fig. 3.10(b) shows the pupil function W recovered following Eq. 3.4 at position (x_1, y_1), the center of the black square in Fig. 3.10(a). Fig. 3.10(c1)-(c5) are 5 of the 17 intensity measurements of the microsphere at position (x_1, y_1) under different amounts of defocus: $I_d(s = 0)$, $I_d(s = \pm 3)$, and $I_d(s = \pm 6)$. Fig. 3.10(d1)-(d5) display the corresponding aberrated image estimates $I_a(s)$ generated by the recovered pupil function in Fig. 3.10(b). The applied GPS algorithm successfully minimizes the mean-squared error difference between the measurements $I_d(s)$ and the estimates $I_a(s)$.

Following this aberration recovery pipeline, 8 Zernike coefficients are calculated for approximately 350 unique spatial locations across the microscope's FOV. Fig. 3.11(a)-(f) plot the recovered second, third, and fourth order spatially varying aberrations of our tested 2X objective lens, corresponding to x-astigmatism, y-astigmatism, defocus, x-coma, y-coma, and spherical aberration, respectively (first order Zernike modes are normally not considered as aberrations, and are thus not shown). The full FOV image of our calibration target is displayed at the bottom plane of each plot, where the FOV diameter is 1.3 cm. Each blue dot in Fig. 3.11 represents the recovered coefficient for the corresponding Zernike mode, and the spatial location of each blue dot corresponds to one microsphere labeled in Fig. 3.10(a).

Finally, we fit these 350 discrete values to a continuous polynomial function $p_m(x, y)$, allowing us to accurately recover the pupil function at any location across the image plane (curved surfaces in Fig. 3.11). The order of each polynomial function can be predicted via aberration theory for a conventional imaging platform [41]. The aberrations of increasingly unconventional optical designs in computational imaging systems may not follow such predictable trends, which we may account for with alternative fitting models and/or recovering coefficients at more

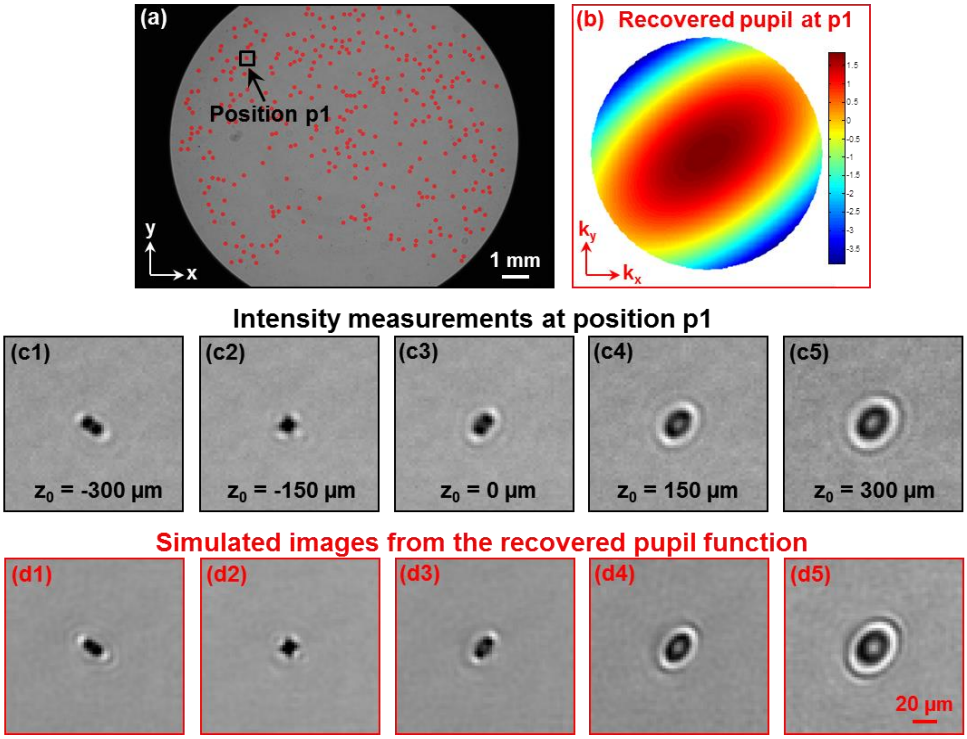

Figure 3.10: Off-axis aberration characterization with a calibration target. (a) 350 microspheres are automatically identified on a microscope slide, each denoted by a red dot. (b) The recovered pupil function at position (x_1, y_1). (c1)-(c5) Intensity measurements $I_d(s)$ of the microsphere centered at (x_1, y_1) under different amounts of defocus. (d1)-(d5) The corresponding aberrated image estimates generated using the pupil function in (b).

than 350 unique spatial locations.

We verified the accuracy of our aberration parameter recovery process with an additional simple experiment. We defocused the calibration target by +50 μm along the optical axis and again implemented our aberration parameter recovery process (using the same ground truth images as before). For the tested wide-field microscope objective, Fig. 3.12 displays two of these fitted polynomial functions for spatially varying defocus: one computed for an in-focus target and one for the target under +50 μm of defocus. The major difference between the two polynomial fits is a constant offset corresponding to $\Delta z = 48.9\mu$m, which is in good agreement with the experimentally induced +50 μm displacement distance. As a reference, the depth-of-focus of the objective lens is about 80 μm.

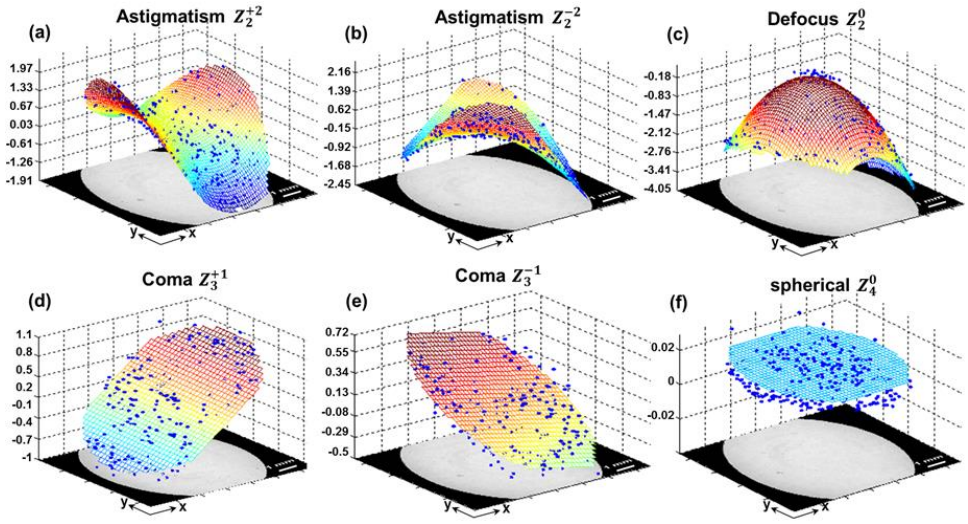

Figure 3.11: Spatially varying aberrations of the 2X objective lens. Each data point, denoted by a blue dot, represents the extracted Zernike coefficient weight for one microsphere. 350 microspheres are identified over the entire FOV and their corresponding parameters are fitted to a 2D surface for each type of aberration. (a)-(f) correspond to x-astigmatism, y-astigmatism defocus, x-coma, y-coma, and spherical aberration.

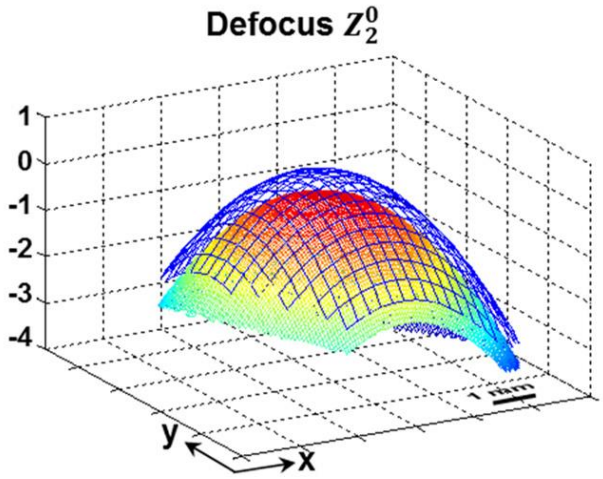

Figure 3.12: Recovered defocus parameter function $p_5(x, y)$ with (color surface) and without (blue grid) +50 μm of sample defocus. The difference between these two surfaces corresponds to a defocus distance of +48.9 μm, which is in a good agreement with the actual displacement distance.

Large FOV, High Resolution FP Microscopy System

The full FOV is segmented into 40x40 small tiles in which the LED illumination can be treated as a plane wave and the aberration can be considered spatially invariant. Each image in the captured full FOV image stack is segmented into tiles and the stack of images in the same tile are used to reconstruct a high resolution image of the tile. In the per-tile-reconstruction process, the aberration information calibrated from sub-section 3.4 is used to generate an aberrated pupil function and is incorporated in the phase retrieval algorithm so that the aberration is removed during the reconstruction. These resolution-enhanced tiled images are stitched together to generate a large FOV, high resolution FPM image. To get a color FPM image, red, green, and blue LEDs are used to generate three color channels of FPM images, which are later combined into an RGB image.

We demonstrate color FPM with our prototype by acquiring a wide-FOV color image of a pathology slide (human adenocarcinoma of breast section, Carolina), as shown in Fig. 3.13. Vignetted high-resolution views are provided in Fig. 3.13(b)-(d). The imaging FOV is approximately 120 mm^2, the same as that from a 2X objective lens, whereas the maximum achieved NA is 0.4, similar to that of a typical 20x objective (MPLN, 0.4 NA, Olympus). The conventional microscope images taken with 20X and 2X lenses are shown for comparison in Fig. 3.13(c2) and (c3).

For the generated FPM image, the resolutions is 1.56 μm so the Nyquist sampling pixel size is $(0.78\mu m)^2$. The SBP of a monochromatic image is: $SBP = \frac{120mm^2}{(0.78\times10^{-3}mm)^2} \times 2 = 0.395$gigapixel. The factor of 2 here is because both amplitude and phase information are reconstructed. For the full FOV color image, it contains approximately 1.2 gigapixels of information.

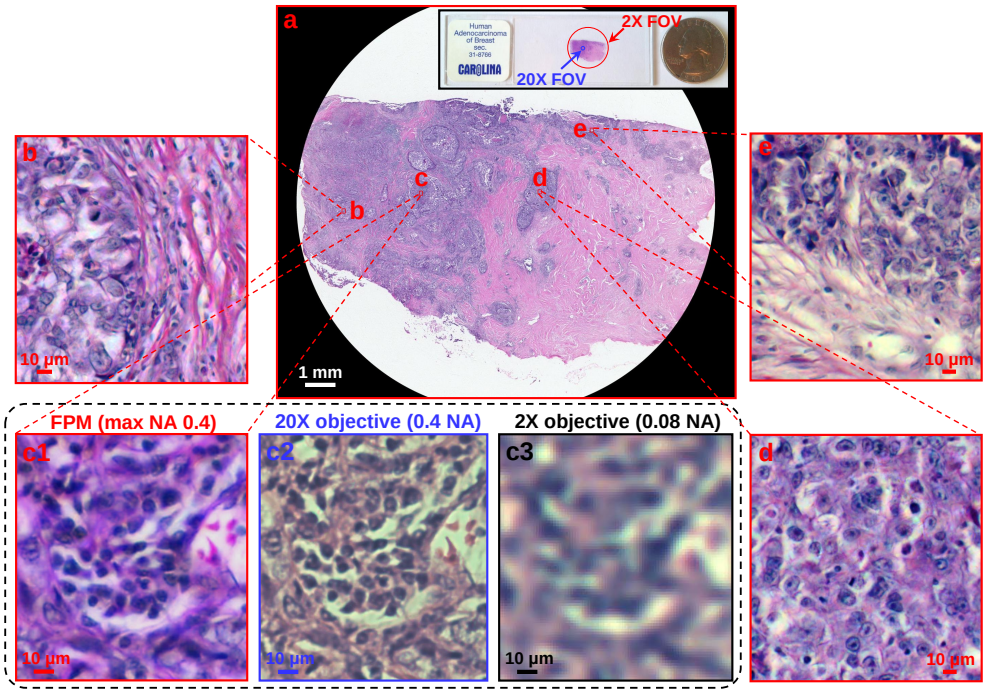

Figure 3.13: Gigapixel color imaging via FPM. (a) A wide-FOV color image of a pathology slide, with a SBP of approximately 0.9 gigapixels. (b, c1, d, and e): Vignetted high-resolution views of the image in (a). Images taken by a conventional microscope with a 20X (c2) and a 2X (c3) objective lens, for comparison. A color image sensor (DFK 61BUC02, Image Source Inc.) is used for capturing (c2 and c3).

Chapter 4

EMBEDED PUPIL FUNCTION RECOVERY

4.1 Introduction

We elaborated a digital wavefront correction strategy to correct for the spatially varying aberration [40, 43, 44] in Section 3.4 to exploit the full throughput of the FPM imaging platform. We demonstrated a high-resolution (1.56 μm, 0.4 NA), wide-FOV (120 mm^2) computational microscope with a final SBP of 0.4 gigapixel, which is highly desired for many biomedical applications such as digital pathology, haematology, and immunohistochemistry.

One of the drawbacks of the aforementioned wavefront correction is that a pre-characterization of the spatially varying aberration of the microscopy system is needed [40]. Such a characterization can be computationally onerous, and is sensitive to the movement of the elements in the system. An adaptive wavefront correction method for FPM has been reported [37] and it uses an image-quality metric as a guide star for adaptive system corrections. This method eliminates the need of a pre-characterization process and is in particular useful for factoring out system uncertainty. However, the global optimization process imposes a heavy load on computational resources; only a limited number of low order aberrations can be corrected in a reasonable time duration.

In this chapter, we introduce a new phase retrieval algorithm, termed embedded pupil function recovery (EPRY), which can reconstruct both the spatial Fourier spectrum of the sample and the pupil function of the imaging system from the captured FPM dataset (the spatial Fourier spectrum can be directly recast as the spatial image of the sample by simply taking an inverse Fourier Transform). In this case, an aberration-free image of the sample can be recovered and the aberration behavior of the image system can be estimated from the recovered pupil function without a complicated calibration process.

4.2 Reconstruction Algorithm

In cases when we have a precise estimation of the pupil function $P(\mathbf{u})$ from the pre-characterized aberration behavior, the phase retrieval algorithm with G-S type update function is used to reconstruct a sample spectrum $S(\mathbf{u})$. However, because

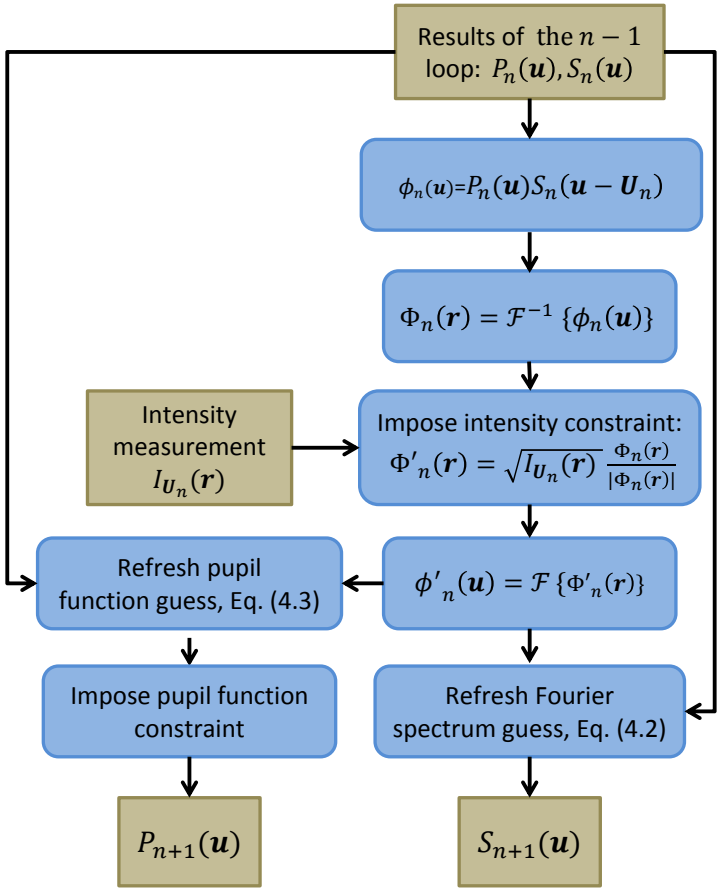

Figure 4.1: Flowchart of EPRY-FPM algorithm.

the phase retrieval algorithm only renews the sample spectrum while keeping the pupil function unchanged, an imprecisely estimated pupil function will result in a poor recovery. Such inaccuracy in the pupil function estimation can be caused by the limited orders of aberration considered in the pre-characterization process [40] or by mechanical or optical changes in the microscopy system.

In this chapter, we demonstrate the EPRY-FPM algorithm, which is developed to address these errors by recovering both the Fourier spectrum of the sample and the pupil function of the imaging system simultaneously. We make two main changes to the original FP algorithm: 1) a gradient-descent-based update function is used, making the phase retrieval algorithm converge faster, and 2) in the updating step, the error information is used to update both the sample spectrum and the pupil function.

The flowchart of the EPRY-FPM algorithm is shown in Fig. 4.1. At the beginning, an initial guess of the pupil function and sample spectrum, labeled as

$P_0(\mathbf{u})$ and $S_0(\mathbf{u})$, are provided to start the algorithm. Generally, the initial pupil function guess is set as a circular shape low-pass filter, with all ones inside the pass band, zeros out of the pass band, and uniform zero phase. The radius of the pass band is $k_c = \mathrm{NA_{obj}} \times 2\pi/\lambda$, where $\mathrm{NA_{obj}}$ is the numerical aperture of the microscope objective and λ is the illumination wavelength. The Fourier transform of a frame of an up-sampled low-resolution image is taken as the initial sample spectrum guess. All the captured images are addressed in a sequence $I_{\mathbf{u}_n}(\mathbf{r})$, n from 0 to N-1 (N is the number of captured images), and considered in turn, with both the pupil function and sample spectrum updated each loop.

In the nth loop, with the knowledge of reconstructed $P_n(\mathbf{u})$ and $S_n(\mathbf{u})$ from the previous loop, the exit wave at the pupil plane while the sample is illuminated by wavevector $\mathbf{u}_n$ can be simulated by the multiplication $\phi_n(\mathbf{u}) = P_n(\mathbf{u})S_n(\mathbf{u} - \mathbf{u}_n)$, and the simulated image on the detector is the inverse Fourier transform of it $\Phi_n(\mathbf{r}) = \mathcal{F}^{-1}\{\phi_n(\mathbf{u})\}$. Then the intensity constraint is applied: the modulus of the simulated image is replaced by the square-root of the real intensity measurement $I_{\mathbf{u}_n}(\mathbf{r})$, which is captured with illumination wavevector $\mathbf{u}_n$, such that:

$$\Phi'_n(\mathbf{r}) = \sqrt{I_{\mathbf{u}_n}(\mathbf{r})} \frac{\Phi_n(\mathbf{r})}{|\Phi_n(\mathbf{r})|}. \tag{4.1}$$

Next, an updated exit wave is calculated via a Fourier transform: $\phi'_n(\mathbf{u}) = \mathcal{F}\{\Phi'_n(\mathbf{r})\}$, and the updated pupil function and sample spectrum is extracted from this result using two update functions, whose form is similar to the extraction function mentioned in [8, 45]. The sample spectrum update function is given by:

$$S_{n+1}(\mathbf{u}) = S_n(\mathbf{u}) + \alpha \frac{P_n^*(\mathbf{u} + \mathbf{u}_n)}{|P_n(\mathbf{u} + \mathbf{u}_n)|^2_{max}} \left[\phi'_n(\mathbf{u} + \mathbf{u}_n) - \phi_n(\mathbf{u} + \mathbf{u}_n)\right]. \tag{4.2}$$

The correction of the sample spectrum is extracted from the difference of the two exit waves by dividing out the current pupil function, and this correction is added to the current sample spectrum guess with weight proportional to the intensity of the current pupil function estimate. The constant α adjusts the step size of the update. In this work, $\alpha = 1$ is used for the results.

The pupil update function takes the similar form:

$$P_{n+1}(\mathbf{u}) = P_n(\mathbf{u}) + \beta \frac{S_n^*(\mathbf{u} - \mathbf{u}_n)}{|S_n(\mathbf{u} - \mathbf{u}_n)|^2_{max}} \left[\phi'_n(\mathbf{u}) - \phi_n(\mathbf{u})\right]. \tag{4.3}$$

In this function, the roles of the pupil function and sample spectrum function are reversed, while the basic principle remains the same. The constant β adjusts the step size of the pupil function update and $\beta = 1$ is used in this work.

To suppress noise, a pupil function constraint is imposed on the updated pupil function. For a microscope system, a physical circular aperture stop is set to define the NA, and thus the area in the pupil function that corresponds to the stop should always be zero. The non-zero points in the updated pupil function in the region corresponding to the stop are caused by the noise in image acquisition, and are set to zero to eliminate the noise. After that, we have updated pupil function $P_{n+1}(\mathbf{u})$ and sample spectrum function $S_{n+1}(\mathbf{u})$.

This process continues until all the N captured images in the sequence $I_{\mathbf{u}_n}(\mathbf{r})$ are used to update the pupil and sample spectra, at which point a single iteration of EPRY-FPM is complete. Then the whole iterative process is repeated for more iterations to improve convergence toward the final pupil and sample spectra. Finally, the sample spectrum is inverse Fourier transformed back to the spatial domain, where we get a high resolution, modulus and phase distribution of the sample.

The extra computational cost of EPRY-FPM algorithm is tiny compared to the original FPM algorithm. Assuming that each captured low-resolution intensity image contains m raw pixels. For each loop, the exit wave simulation, inverse Fourier transform, intensity constraint and Fourier transform process has computational cost of m, $m \cdot \log(m)$, m and $m \cdot \log(m)$ respectively. The sample spectrum update, pupil function update and pupil function constraint has a computational cost of $3m$, $3m$, and m, respectively. So the computational cost of the original FPM algorithm is $5m + 2m \cdot \log(m)$ for each loop, and the computational cost of the EPRY-FPM algorithm is $9m + 2m \cdot \log(m)$. Generally, the raw pixel count m is in the order of a million, so the incremental computational cost of $4m$ is small compared to $2m \cdot \log(m)$.

4.3 Simulation Results

To verify the effectiveness of the EPRY-FPM algorithm to separate the pupil function and sample distribution from the measurements, the original FPM phase retrieval algorithm used in [31] and the EPRY algorithm are run using a simulated FPM dataset. Here we set the initial FPM pupil function guess as a flat function. We note that the FPM work reported in [31] actually used a pupil function estimate (with only the lowest five orders of Zernike polynomials accounting for the aberrated

phase). The point of this current exercise is to compare the FPM and EPRY-FPM performance in the total absence of prior aberration determination.

Two images, each containing 512x512 pixels with pixel size 0.2μm, are used as the modulus and phase of the sample, as shown in Fig. 4.2(a1)-(a2). The modulus is rescaled to $(0, 1)$ and phase is rescaled to $(-\pi, \pi)$. The simulated microscope system has an $\mathrm{NA}_{\mathrm{obj}} = 0.08$ with wavefront aberration, resulting in a circularly shaped pupil function with a radius of 13 pixels and a pupil function phase as shown in Fig. 4.2(a3). A sequence of 225 images are simulated with different plane wave illuminations, with enough overlap in Fourier domain to assure convergence of the of the algorithm [31].

In both algorithms, the initial guess of the pupil function is set as a circular shape low-pass filter radius of 13 pixels with zero phase, and the first image in the sequence is up-sampled and Fourier transformed to serve as the initial guess of sample spectrum. Both algorithms were run for 100 iterations and the results are shown in Fig. 4.2(b1-b3) and 4.2(c1-c3). The reconstruction using the original uncorrected FPM is severely degraded. This is because the aberrated wavefront of the pupil function repeatedly influenced the low and high frequency components of the sample spectrum. In addition, there is a significant degree of crosstalk between the modulus and phase images resulting from the lack of knowledge about the pupil function phase distribution. In comparison, the EPRY-FPM reconstruction is able to successfully separate the pupil function from the sample spectrum, resulting in a quality-improved image and an accurate measurement of the real pupil function phase. Because the illuminations do not cover the entire Fourier spectrum of the sample, there exists a small amount of crosstalk in the modulus and phase image, resulting in several phase-wrapped pixels in the reconstructed pupil function.

The convergence of both algorithms are also measured by calculating the normalized mean square error metric [46] in each iteration:

$$E^2(m) = \frac{\sum_{\mathbf{u}} |S(\mathbf{u}) - \alpha S_m(\mathbf{u})|^2}{\sum_{\mathbf{u}} |S(\mathbf{u})|^2}. \tag{4.4}$$

The parameter α is given by:

$$\alpha = \frac{\sum_{\mathbf{u}} S(\mathbf{u}) S_m^*(\mathbf{u})}{\sum_{\mathbf{u}} |S(\mathbf{u})|^2}. \tag{4.5}$$

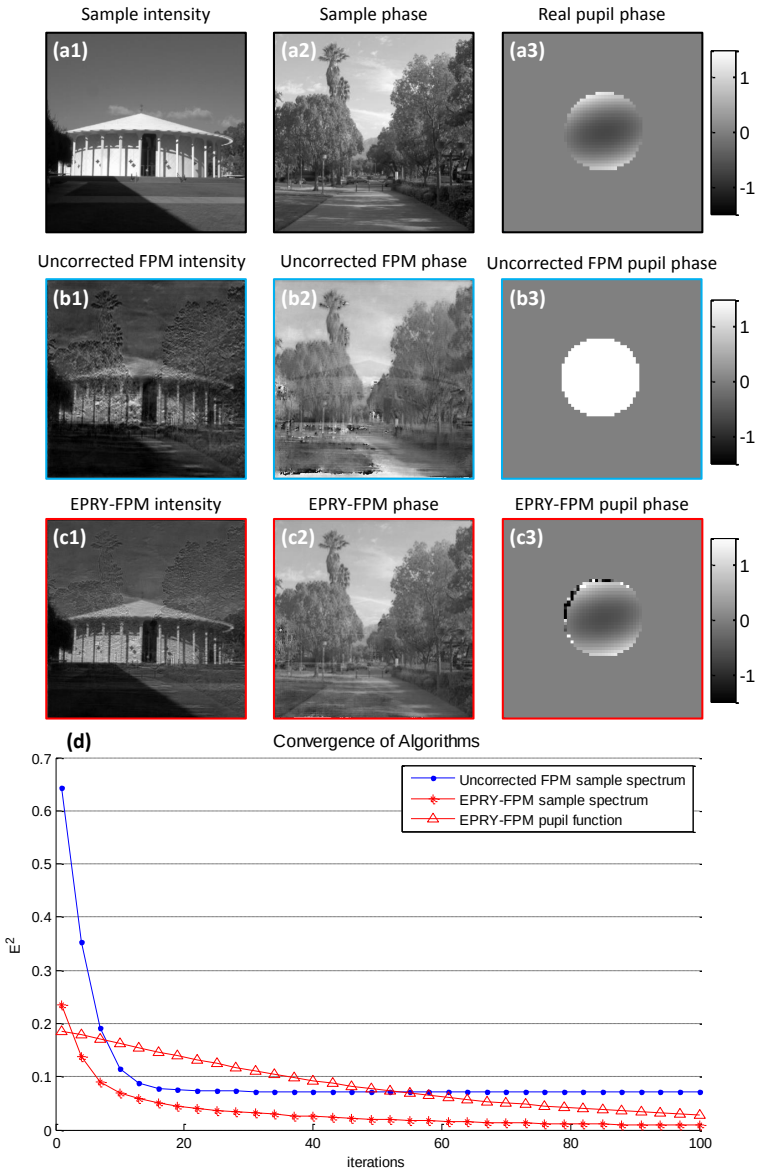

Figure 4.2: Sample for simulation and reconstruction results. (a1-a2) Sample modulus and phase used to generate simulated dataset. (a3) Phase of the pupil function used to generate simulated dataset; intensity of the pupil function is a circular shape low pass filter the same size as the phase circle. (b1-b2) Reconstructed modulus and phase using the original uncorrected FPM algorithm. (b3) Initial guess of the pupil phase used in both uncorrected FPM and EPRY-FPM, the initial guess of the pupil intensity is a circular shape low pass filter the same size as the phase circle. (c1-c2) Reconstructed modulus and phase using EPRY-FPM algorithm; the initial guess of the sample spectrum is the same as the one used in uncorrected FPM algorithm. (c3) Reconstructed pupil function phase, showing a similar distribution as (a3). (d) Plot of convergence of both algorithms using the normalized mean square error metric.

This parameter allows the error metric to be invariant to a constant multiplication and a constant phase offset. Here $S(\mathbf{u})$ is the true sample spectrum distribution and $S_m(\mathbf{u})$ is the reconstructed sample spectrum distribution after m iterations. $E^2(m)$ is calculated over the center 128 x 128 pixels area which have enough overlapping, and the results are shown in Fig. 4.2(d). For the reconstructed sample spectrum, EPRY-FPM algorithm has a significantly faster convergence rate compared to the uncorrected FPM algorithm, and ends up with an error of less than 0.01. Meanwhile, for the uncorrected FPM algorithm, the error stopped decreasing at 0.08 after 20 iterations, which is the limit imposed by the wavefront aberration in the real pupil function. The convergence of reconstructed pupil function using EPRY-FPM is also calculated using the same metric. As we can see in the plot, although it converges slower than the sample spectrum at the first few iterations, the final result has a small error of about 0.05.

4.4 Experimental Results

We also implement the algorithm on experimental data to demonstrate its performance. Our experimental setup consists of a conventional microscope with a 2X, NA=0.08 objective, a CCD camera mounted on top, and a programmable color LED matrix as the light source. The setup is the same as the one reported in [31]. We used a Wright-Giemsa stained blood smear as a sample and we captured a sequence of 225 images using the center 15x15 red LEDs. We analyzed an area of 150μm*150μm from the sample, located at 35% to the edge from the center of the FOV of the imaging system, where the aberration is non-negligible. We ran both uncorrected FPM and EPRY-FPM algorithms on the dataset from this area for 5 iterations through all 225 images. The initial guess of the pupil function was set as a circular shape low-pass filter, whose radius was determined by the NA, with zero phase, and the first image is up-sampled and Fourier transformed to serve as the initial guess of sample spectrum.

The results of both algorithms are shown in Fig. 4.3. Fig. 4.3(a1) and (a2) shows the intensity and phase distribution of the blood smear using the uncorrected FPM algorithm. The image is blurry due to the very significant amount of objective aberration at that location in the FOV (the aberrations get progressively worse as we move away from the FOV's center), the contour of the blood cells cannot be recognized clearly and it is hard to distinguish white blood cells from red blood cells. A high quality image can be achieved using the EPRY-FPM algorithm, as shown in Fig. 4.3(b1)-(b2). The morphology of blood cells is clear, the zone of

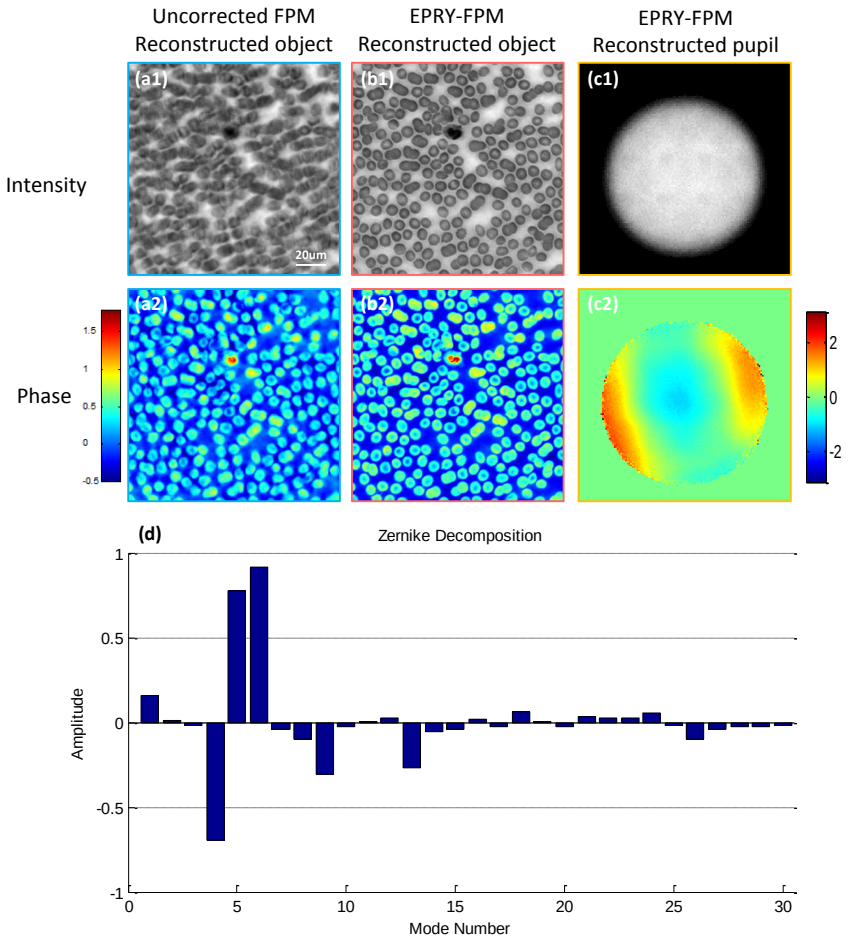

Figure 4.3: Reconstruction from uncorrected FPM and EPRY-FPM algorithms using FPM blood smear dataset. The initial guess of the pupil function is a circular shape low pass filter with no phase, and the reconstructed region is located 35% from the center of the FOV. (a1-a2) Reconstructed sample intensity and phase using uncorrected FPM algorithm. (b1-b2) Reconstructed sample intensity and phase using EPRY-FPM algorithm. (c1-c2) Reconstructed pupil function modulus and phase using EPRY-FPM algorithm. (d) Zernike decomposition of pupil function phase. The amplitude of the lowest 30 modes (representing the 30 lowest order aberrations) are shown.

central pallor for the red blood cells is obvious, and the shape of the nucleus of the white blood cell is recognizable. From the phase image in Fig. 4.3(b2), we can also see the donut shape of the red blood cell. The pupil function for this FOV is also recovered using the EPRY-FPM algorithm and shown in Fig. 4.3(c1)-(c2).

The recovered pupil function can be further studied to examine the properties of the lens system. For one example, the size and shape of the modulus of the pupil function reflects the shape and position of the physical aperture stop. In this case, the modulus part of the pupil function approximately remains the same as the initial guess, meaning that the numerical aperture is well defined by a circular shape aperture. We can also see that the pupil function that ought to be centered has a slight shift to the bottom right, which reflects an imprecise estimation of the wavevector $\mathbf{u}_n$ caused by the shift of the LED matrix from its originally aligned position. Through the EPRY-FPM algorithm, this error is corrected.

As another example, we note that the phase of the pupil function represents the wavefront aberration [3]. If we do a decomposition of the pupil function phase component in Zernike polynomials [47], the coefficient of each Zernike polynomial represents the extent of aberration corresponding to this Zernike polynomial. In our case, the decomposition is executed and the coefficients of the first 30 Zernike polynomials are shown in Fig. 4.3(d). Different Zernike polynomials represent different types of aberration, from low order to high order according to the mode number. Mode number 1 represents the piston term, which will cause a constant phase shift to the entire aperture and is not considered as an aberration. The three dominant modes for the wavefront aberration are mode number 4, 5, and 6, which represent defocus aberration, astigmatism in the x direction, and astigmatism in the y direction, respectively. We can also see that coma aberration (mode 7 and 8) is not severe for this FOV but there are some higher order aberrations that are non-negligible for this position, such as mode 9 (trefoil) and mode 13.

4.5 EPRY-FPM for Large FOV, High Resolution Image Reconstruction

For a large FOV microscope system, the aberration and, by extension, pupil function can be expected to show spatial variations [40, 48]. To ensure the effectiveness of the EPRY-FPM algorithm, we segment the entire FOV into small tiles where in each tile the aberration can be considered as constant [31, 40]. For our FPM system with a 6mm radius FOV, the entire area is segmented into tiles sized 350μm*350μm, and the EPRY-FPM algorithm is run on the dataset of each tile

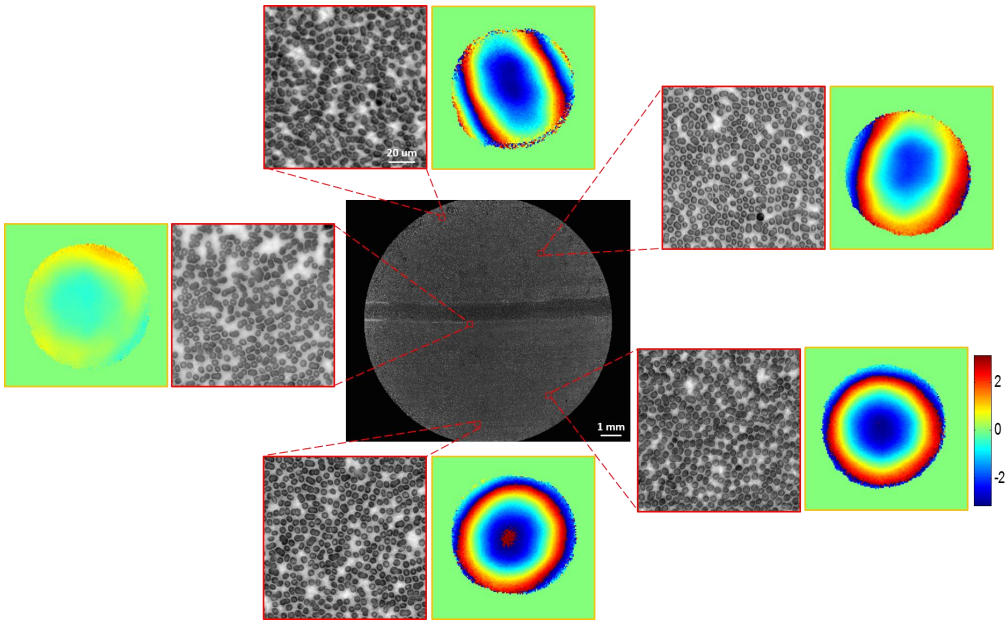

Figure 4.4: Full FOV high resolution monochrome image (red LED illumination) reconstruction of blood smear: the entire FOV is segmented into small tiles, and the aberration is treated as constant in each tile. EPRY-FPM algorithm is run on each tile and the reconstructed high resolution images are mosaicked together. The insets show the detail of the reconstructed image and also the wavefront aberration at those locations.

independently, using the aforementioned process. We take advantage of the fact that the pupil function varies continuously and use the reconstructed pupil function from the adjacent tile as the initial pupil function guess (instead of a flat phase initial guess) for the current tile to increase the convergence rate of the algorithm. All these reconstructed high resolution, aberration eliminated images are combined together to form a full FOV high resolution image, as shown in Fig. 4.4. The reconstructed sample image and wavefront aberration of five regions on the FOV are shown in Fig. 4.4, demonstrating the stable image quality from center to edge achieved by EPRY-FPM algorithm, despite the much more severe aberration at the edge compared to the center.

The same algorithm was also implemented to render a high resolution, large FOV color image of a pathology slide. The center 15x15 red, green, and blue LEDs on the LED matrix are lit up individually and 3 sets of FPM data are captured. For each color channel, the same segmentation and reconstruction processes are executed as previously described. For each tile, because the pupil function which contains the defocus aberration is separated from the sample spectrum in EPRY-FPM

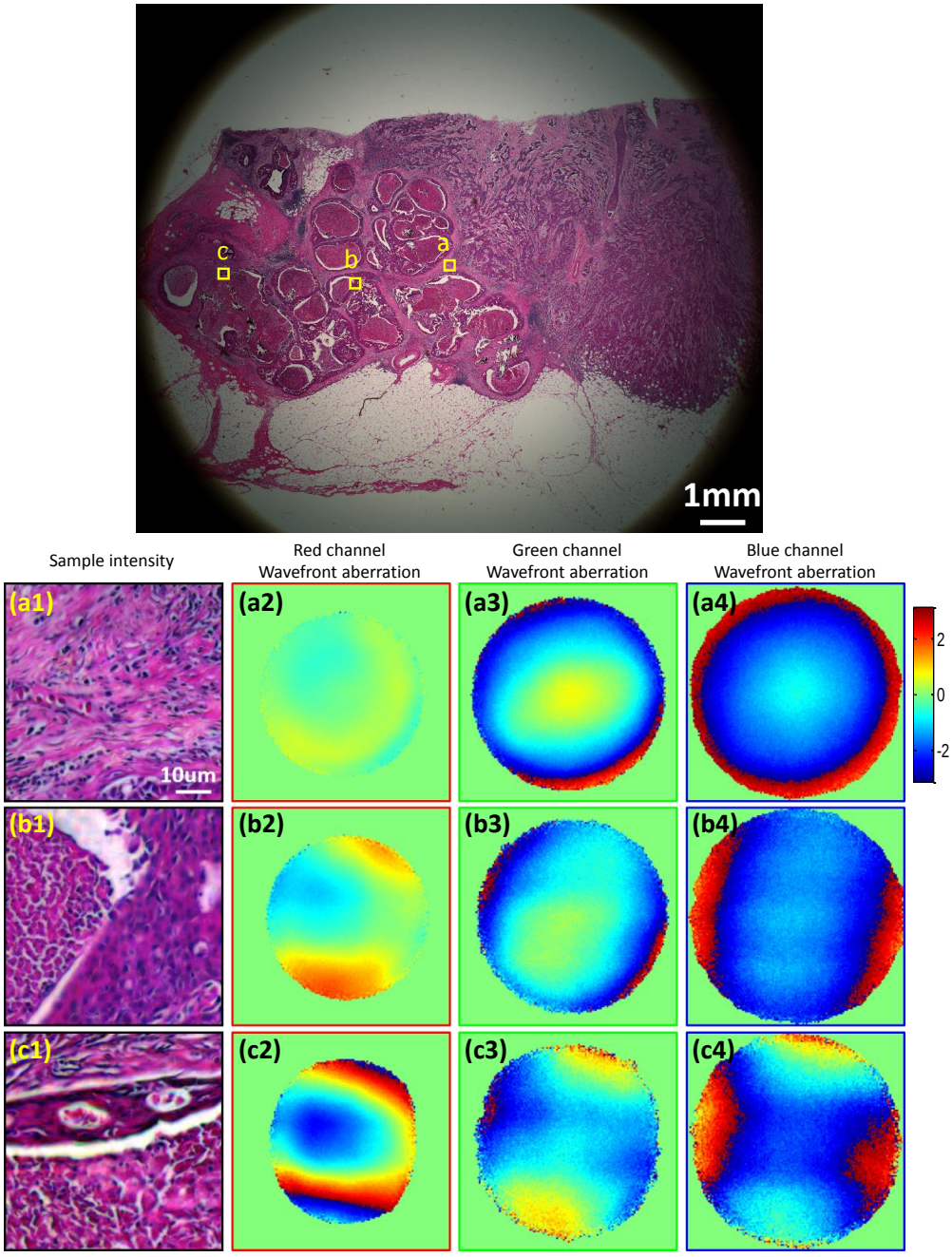

Figure 4.5: Full FOV high resolution color image reconstruction of pathology slide: each color channel is reconstructed using the same method described in Fig. 4.4, and three channels are combined to generate RGB image. (a1, b1, c1) reconstructed sample intensity of three regions in the FOV. (a2, b2, c2) reconstructed red channel wavefront aberration of the three regions. (a3, b3, c3) reconstructed green channel wavefront aberration of the three regions. (a4, b4, c4) reconstructed blue channel wavefront aberration of the three regions.

reconstruction process, each color channel is focused at its best focal plane. In other words, the axial chromatic aberration, which is caused by different wavelengths focused at different planes, is correctable by EPRY-FPM. Before we combine red, green, and blue channel images in the same tile together, green and blue images are slightly shifted spatially relative to the red channel to correct for lateral chromatic aberration. An automatic program is run to find the correct amount of shift which maximizes the correlation of the red-green image pair and red-blue image pair respectively. Finally, all the color tiles are mosaicked together and the result is shown in Fig. 4.5. Three regions are magnified and shown in Fig. 4.5(a1)-(c1). The wavefront aberration on corresponding region for red, green, and blue channels are also shown in the second (a2-c2), third (a3-c3), and fourth columns (a4-c4) of Fig. 4.5. We would like to point out that the different sizes of the circles between different color channels are caused by the different wavelengths. We further note that the shape of the pupil function changed from a circle to an ellipse significantly as we move towards the edge of the image. This is because the 2X objective we are using is not strictly a telecentric lens [49] and, as such, the aperture shape can be expected to change asymmetrically.

4.6 Comparison with Original Phase Retrieval Algorithm

To quantify the improvement in image quality, we use a USAF target in the next set of experiments. The target is placed at 0%, 27%, 54%, and 80% of the entire FOV from the center, and four sets of images are captured respectively using the red LED. Three methods are run on these four sets of images: 1) the original FPM algorithm without the knowledge of wavefront aberration (uncorrected FPM), 2) the original FPM algorithm with pre-characterized defocus and astigmatism aberration (corrected FPM) [40], 3) the EPRY-FPM algorithm without the knowledge of wavefront aberration. Group 8 and 9 of all the 12 reconstructed images are shown in Fig. 4.6.

As we can see, the image quality is highly degraded by aberration for the 54% and 80% FOV locations (Fig. 4.6(a3), (a4)). After the correction of defocus and astigmatism aberration by method 2, the line on Group 9 (periodicity < 2μm) can be vaguely resolved (Fig. 4.6(b3), (b4)). Three reasons prevent further improvement of the image quality using method 2. First, a non-linear optimization algorithm [40] is used for the aberration pre-characterization process, so adding N more aberration variables for optimization means searching for the minimum point in an Nth order higher dimensional space, which will make the computational complexity 2N times

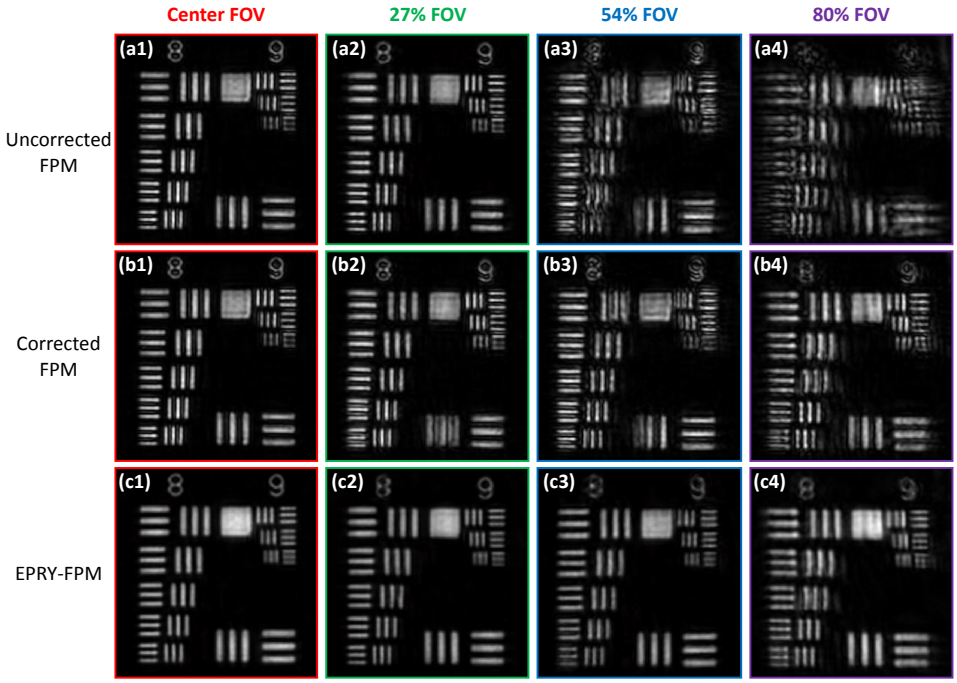

Figure 4.6: Characterization of achievable resolution by three methods using USAF target: (a1-a4) Images at different FOV reconstructed by using uncorrected FPM method. (b1-b4) Images at different FOV reconstructed by using corrected FPM method. (c1-c4) Images at different FOV reconstructed by using EPRY-FPM method without pre-characterized aberration.

that of the original 3 aberration optimization. Second, the image sets that are used for aberration characterization only contain low resolution images captured by the NA=0.08 objective. The high order aberration information is easily overwhelmed by the noise of the imaging system, resulting in an imprecise measurement of the high order aberration. Third, the characterized high order aberration information can be volatile. This is because such aberration is highly sensitive to mechanical or optical system drifts. In conclusion, method 2 is impractical to correct higher order aberration.

However, by using the EPRY-FPM algorithm, the image quality is significantly improved. This is largely attributable to the fact that the EPRY-FPM considers and characterizes the entire pupil function rather than focusing on just the lower orders of wavefront aberration. As shown in Fig. 4.6(c3), (c4), group 9 element 3 can be resolved, resulting in a resolution of 1560μm throughout the entire FOV. There are two primary reasons that the image quality at the edge is worse than the center:

First, the synthesized Fourier spectrum domain is no longer symmetric for the edge region because the 15x15 LEDs for illumination are centered at the center point of the entire FOV. Second, because of the field distortion of the 2X objective, the pixel size on the sample plane is not the same from center to edge. The imprecise distance measurement from pixel count results in an imprecise estimation of wavevectors $\mathbf{U}_n$ for the reconstruction of the edge FOV, which degrades the image quality.

4.7 Conclusion

In this chapter, we described a new phase retrieval algorithm for FPM system called EPRY-FPM which can recover both the expanded sample spectrum and the pupil function of the imaging system by merely using the image set of the sample captured by FPM. The implementation of EPRY-FPM algorithm provided us with improvement of image quality, due to the fact that the entangled sample spectrum and pupil function are isolated from the captured image set during the recovery process. Moreover, the recovered pupil function which contains wavefront aberration information of the microscopy system can be further studied to characterize the behavior of the lenses. We illustrated the ability of the EPRY-FPM algorithm to cope with the spatially varying aberration of a large FOV image system, and reconstructed high resolution, large FOV monochrome and color images of biological samples using this algorithm. In the study of the recovered pupil function for the large FOV image system, we observed variation spatially and spectrally. From the elliptical shape of the pupil function at the edge of the FOV, we can also estimate the deviation of this objective lens from a telecentric lens. By imaging a standard USAF target and comparing the result with the original FPM algorithms, we showed that the EPRY-FPM algorithm is an automatic method which is less time consuming, generates higher quality images, and is more robust to the alignment drift of FPM system.

With the help of this algorithm, the FPM no longer requires the time-consuming and laborious acquisition of pupil characterization data. Besides its obvious advantage in simplicity of use, the development of EPRY-FPM also opens up the choice of optical systems we can adapt for FPM usage. Highly aberrated optical systems or systems without a well-defined physical aperture stop, which were previously precluded, can now be considered.

Finally, we would like to note that the EPRY-FPM method can also be potentially employed to characterize optical system aberrations for purposes beyond

FPM. For example, it can be used to benchmark the quality of imaging systems for comparison purposes. Alternately, the recovered system aberration data can be used to design appropriate correction optics to improve a target system. We believe that this simple while elegant method can convert aberration characterization and correction from a formidable task which requires optical professionals to a handy tool for researchers in all areas.

Chapter 5

HIGN NUMERICAL APERTURE FOURIER PTYCHOGRAPHY

5.1 Introduction

As has been mentioned in Chapter 1, the resolving power of an optical microscope is mainly determined by the numerical aperture (NA) of its objective lens, defined as NA $= n \cdot \sin\theta$. Here, n is the refractive index of the medium between the sample and lens, and $\sin\theta$ is the lens acceptance angle. While switching to a higher-NA objective lens in a conventional microscope improves image resolution, it also introduces several undesirable effects. First, the image field-of-view (FOV) is correspondingly reduced. Second, high-NA (i.e., large θ) lenses also require a short working distance, which can make sample manipulation challenging. Third, a way of further increasing the lens NA is through a higher refractive index, n. However, while the introduction of a liquid immersion medium can push the NA beyond unity, it also increases the risk of sample contamination and microscope damage. Fourth, as θ increases, so do lens aberrations, which become increasingly difficult to correct for [50]. This last problem is especially problematic for high NA objective lenses. In Chapters 3 and 4, we showed that aberrations can be significant even within the specified field-of-view of an otherwise well-corrected objective lens system, which prevents diffraction limited performance.

As has been shown in Chapters 2, 3, and 4, Fourier ptychography (FP) is a super-resolution technique that offers an alternative way to increase the NA of a bright-field microscope [31, 51, 52]. Instead of changing the objective lens and possibly applying an immersion medium, we use an LED array to provide angularly varying illumination and acquire a sequence of images. Each off-axis LED shifts a different amount of high spatial frequency information, diffracted from the sample, into the acceptance angle of a dry objective lens. FP then uses a phase retrieval algorithm to fuse each uniquely illuminated image into a final output image with increased resolution. This paradigm shift comes with two notable consequences. First, for a fixed desired resolution, FP operates with a lower-NA objective lens as compared with a conventional microscope. This increases both the imaging FOV and sample-lens working distance. Second, by working with a lower-NA objective lens, we will need to contend less with residual (i.e., uncorrected) aberrations to

potentially achieve a resolution that is more closely matched to the NA-predicted value.

This second point is practically important, because it could significantly alleviate the need to design and construct complicated, multi-element lens systems with many components included just to minimize aberrations. Furthermore, our previous works with microscope systems (Chapter 3 and 4) suggests that the presence of residual aberrations still notably impacts the experimental formation of accurate, wide FOV images. In this chapter, our prime focus is thus to systematically study the true resolution of high-NA objective lenses and determine whether FP offers a significant advantage by working with lower-NA lenses.

Here, we accomplish such a study by working towards two related goals. First, we construct two unique FP microscopes (FPMs) with effective system numerical apertures, NA_{sys}, greater than unity (using a dry 20X 0.5NA and 40X 0.75NA objective lenses, respectively). Second, we benchmark the performance of our new FPMs against other commonly available high-NA microscopes, including oil-immersion setups. Due to its inherent use of controllable illumination and computation, a direct comparison of FPM to conventional oil immersion images is somewhat nuanced.

5.2 High-NA FPM setup

Previous demonstrations of FPM only applied this aperture synthesis process to low-NA microscope setups [31, 51, 53]. To extend FPM to the high-NA case, we start from a conventional microscope with a 20X 0.5NA objective lens (Olympus UPLFLN 20X) and a CCD camera (Kodak KAI-29050). An array of LEDs arranged in concentric rings is used to provide variable off-axis illumination, as shown in Fig. 5.1(a). Each LED consists of three active areas with center wavelengths at 632nm (red), 522nm (green) and 471nm (blue), which can separately acquire three color channels for an RGB image. The outmost ring has a radius of 40 mm and contains 12 LEDs. Two more inner rings, each containing 8 LEDs, are arranged to ensure enough overlap in the Fourier domain with radii of 16 mm and 32 mm, respectively. An Adafruit 32x32 RGB LED matrix panel (same as the one in chapter 3) is used in our experiment, and 3 rings of LEDs are selected within the panel such that their distances to the panel center match with the aforementioned parameters. The LED array is placed 41 mm away from the sample, providing an illumination NA of 0.7 ($\phi_{max} = 45°$). The total spatial frequency support that this arrangement covers is shown in Fig. 5.1(b). The center red circle represents the pass band edge

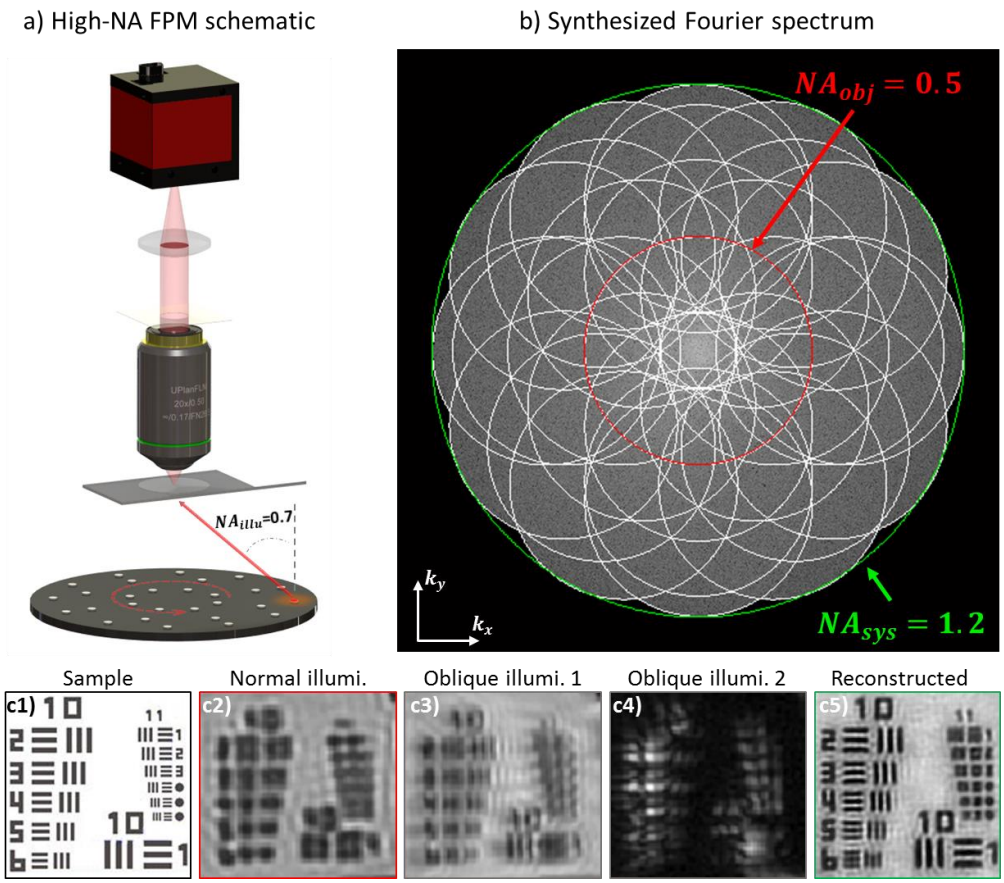

Figure 5.1: High-NA FPM setup and synthesized Fourier domain spectrum. (a) Our primary high NA FPM system consists of a conventional microscope with a 20X 0.5NA objective lens and a ring illuminator, offering an illumination NA of 0.7. (b) Each captured image is merged in the Fourier domain, forming an enlarged passband. Center red circle: Fourier support of the original microscope; white circle: Fourier support of one LED; green circle: synthesized Fourier support of the FPM system. (c1) Known sample intensity; (c2) image captured by a conventional 20X microscope corresponding to red circle in (b); (c3-c4) two images captured with different off-axis LEDs on, corresponding to two of the white circles; (c5) FPM reconstruction, corresponding to the green circle.

(i.e., the CTF) set by the objective lens numerical aperture. During FP capture, we sequentially turn on each of the 28 LEDs in the illumination array and acquire an image. The unique spatial frequency support of each image is denoted by a white circle. In the reconstruction process, all of the information within each white circle is fused together to reconstruct an image with support defined by the large green circle, which is our synthetic system NA. For the present case, $NA_{sys} = 1.2$.

Just like with a conventional microscope, FP can switch to a higher NA objective

lens and achieve a higher system NA. Alternatively, we can move the LED array closer to the sample to form a higher illumination NA, so long as the overlap between each image's spatial frequency support remains sufficiently large (greater than 60% area overlap) [14]. In this work, we select the former option to construct a second FPM system, now using a 40X objective lens with $NA_{obj} = 0.75$ (Olympus UPLFLN 40X) and the same illumination setup as discussed above ($NA_{illu} = 0.7$). Following Eq. 2.5, we expect this second FPM to synthesize a system NA of 1.45. With these two unique setups, we hope to first validate Eq. 2.5, and then test whether the experimental performance of FP, due to its utilization of low-NA, low-aberration lenses, can have a better performance than its high-NA conventional microscope counterpart.

5.3 Resolution Characterization

Comparison between Coherent and Incoherent Illumination

In this section, we propose an experimental procedure to verify the resolution of each of our new high-NA FPM systems. We select this procedure both to help verify our synthetic aperture model in Eq. 2.5, and to fairly compare the resolution of FPM to the resolution of a conventional incoherently (i.e., Köhler) illuminated microscope.

As noted in Section 2.3, Fourier ptychography ideally functions as a coherent imaging system. Given each LED emits light of suitable temporal and spatial coherence (see Appendix A.1), the formation of each FP image simply involves a multiplication of the complex sample spectrum $S(\mathbf{u})$ with a suitably shifted objective lens CTF in the Fourier domain, defining the image's spatial frequency support. The computational goal of FP is to determine $S(\mathbf{u})$ by correctly fusing together the image measurements from each of these uniquely shifted support regions. Section 2.3 argues that this goal is equivalent to the formation of a large, coherent synthetic CTF, CTF_{sys}, with a cutoff frequency defined through Eq. 2.5. CTF_{sys} is a complex function that completely defines the ideal performance of FP.

Unlike the incoherent optical transfer function that solely depends upon image intensities, CTF_{sys} is sensitive to the input light's phase at each spatial frequency [3]. Thus, while it would be ideal for us to characterize each FPM by measuring its CTF_{sys}, required stability at sub-wavelength scales presents an experimental challenge (e.g., small sample imperfections or setup instabilities can lead to large measurement errors). Instead of measuring an entire CTF_{sys}, it is common to define

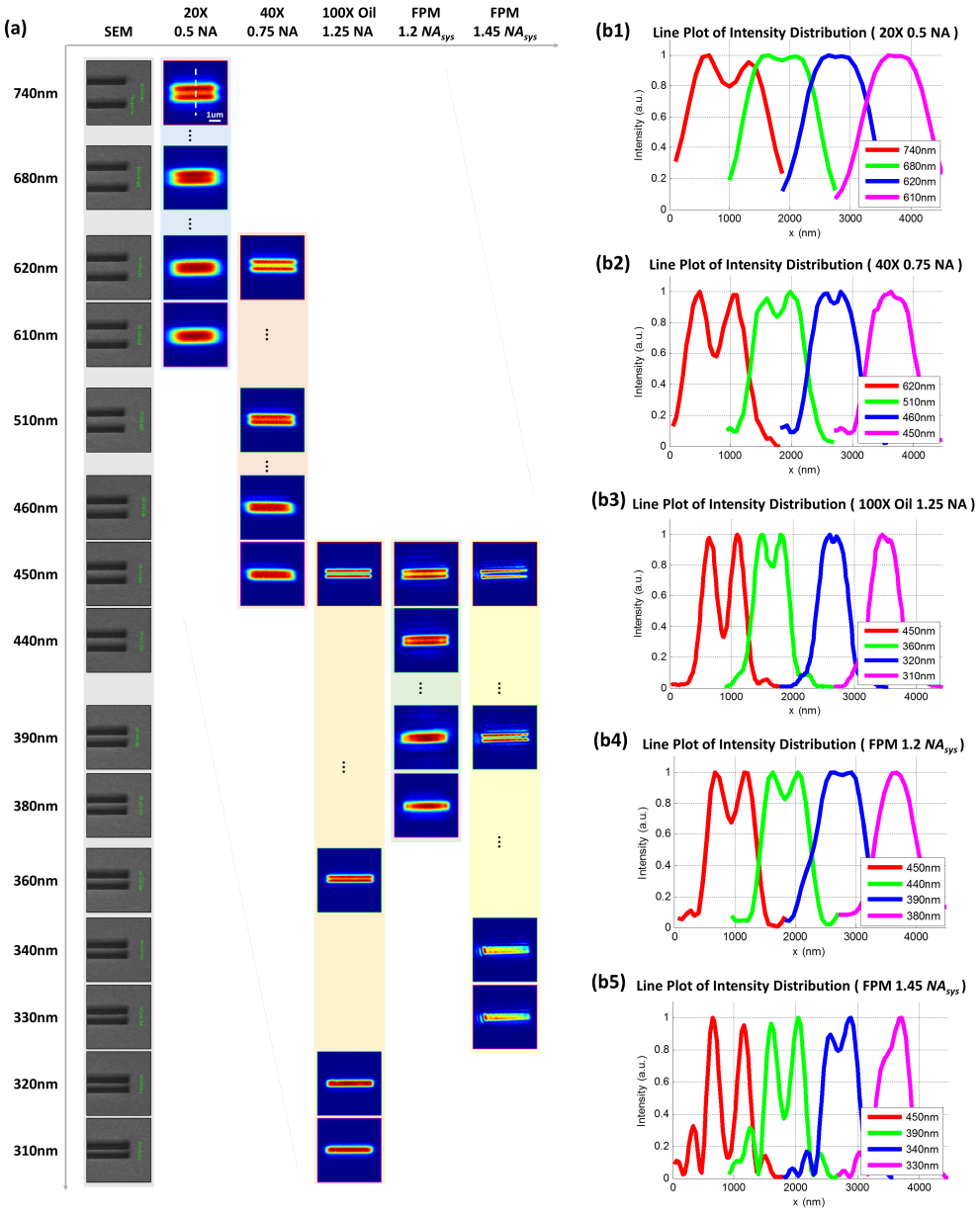

Figure 5.2: Resolution calibration using customized two-slit targets, illumination wavelength $\lambda = 632nm$. (a) SEM, conventional microscope, and FPM images of the two-slit targets (180 nm width, 4500 nm length). (b) Line plots of vertical intensity distribution across both slits, showing a Sparrow resolution limit of 615 nm for 20X 0.5 NA objective (b1), 455 nm for 40X 0.75 NA objective (b2), 315 nm for 100X oil immersion 1.25 NA objective (b3), 385 nm for 1.2 NA_{sys} FPM system (b4), and 335 nm for 1.45 NA_{sys} FPM (b5). Line plots of about 81% dip-to-peak ratio are also shown for a rough estimation of Rayleigh resolution limit [54].

microscope performance using a single cutoff metric [3, 55].

The approach by which the resolution of a coherent imaging system ought to be quantified with a single metric is not a settled matter in literature. In broad terms, published quantifications fall into two camps. One major approach is to use the width of a point-spread function (PSF) (or some related variant), which is widely used to characterize incoherent imaging systems. Significant papers using this method include [56–58]. Proponents of the second camp rightly pointed out that a point-spread function-defined resolution can systematically overestimate the ability of a coherent imaging system to actually resolve two points in close proximity [59]. As such, they argue that a two-point resolution measurement ought to be the defining way to characterize resolution. On the other hand, a counter-argument may be made that for a target with two points that are out of phase with each other, coherent systems can be expected to do a better job of resolving two points than an incoherent one, and as such, the two-point resolution measurement method unfairly penalizes coherent systems [3].

Resolution of FPM Compared to High NA Objective

Here, we choose to risk underestimating instead of overestimating resolution performance. We characterize system resolution by simply identifying the minimum separation between two points or lines that the system can resolve. While alternative resolution measures exist [55], this well-known two-point/slit criterion lends itself nicely to comparing the resolution performance of coherent and incoherent imaging systems. Specifically, we may use the same two-point/slit target to mark FP's performance against typical incoherent standard microscopes. Since the quantification metrics for coherent and incoherent performance are connected to imaging system NA by different constant factors [55, 60], we caution readers seeking to compare our achieved resolutions to those of other reported systems to exercise due diligence. Furthermore, for this target, coherent imaging systems, such as the FPM, can be expected to systemically fare worse than incoherent imaging systems, such as a standard microscope, as the light transmitted through the two-point/slit would have the same phase. In comparison, a target with more phase variations can be expected to perform better for coherent systems. This means that the resolution we expect to measure here for the FPM is a base resolution quantity. For actual practical samples, the FPM may actually do better in resolving features.

We construct our resolution targets by forming aperture pairs of different sep-

aration with a focused ion beam on a gold coated (100 nm thickness) microscope slide. When illuminated from below, each aperture pair forms our two points at a unique separation. We tested two different aperture pair geometries. In the first set, we fabricated each aperture as a round hole with a 200 nm diameter. In the second set, each aperture is a slit of width 180 nm and length 4500 nm. For both target types, we fabricated multiple targets with varying aperture center-to-center distances ranging from 300 nm to 740 nm. For both tested FPM systems, we found that the more light-efficient two-slit target set led to less noisy images, and thus more reliable resolution measurements. The two-slit targets form the focus of this section, while we present and discuss our similar two-hole resolution measurements in Appendix A.3. The scanning electron microscope (SEM) images of 15 different two-slit targets are shown in the first column of Fig. 5.2(a). We mount each target with a #1 coverslip (to simulate our mounting of a biological sample) before imaging.

To measure the two-point resolution for our FPM system, we first illuminate each of the targets with a sequence of red LEDs (center wavelength = 632nm) and capture an image set. We then apply our FP phase retrieval algorithm [31] to reconstruct a high-resolution image from each image set. We execute this entire procedure for our 1.2 NA_{sys} FPM setup first, with the resulting reconstructions shown in the second-to-last column of Fig. 5.2(a). We then repeat this procedure with our 1.45 NA_{sys} FPM setup. These reconstructions are in the last column of Fig. 5.2(a). Each reconstruction displays the image intensity in pseudo-color.

Next, we use the Sparrow resolution criterion [61] to determine the cutoff resolution of our two FPM setups from their target image sets. The Sparrow resolution limit is defined as the distance between two points/slits where the dip in brightness between each peak vanishes in an image. Vertical line traces through each slit pair help identify this resolution cutoff, which we plot in Fig. 5.2(b4-b5). For the 1.2 NA_{sys} FPM setup, we see this intensity dip between the slit peaks decrease as the slit center-to-center distance decreases (Fig. 5.2(b4)). It vanishes at a center-to-center distance of 380 nm, which suggests the measured Sparrow resolution limit of this FPM is approximately 385 nm. The theoretically predicted Sparrow resolution of a coherent illuminated, diffraction limited imaging system with an NA of 1.2 for two-slit target, defined as $d = 0.68\lambda/NA$ (Appendix A.4 shows our derivation of a suitable Sparrow resolution equation), is 358 nm. Thus, with only an 8% deviation between measurement and theory, we find that this 1.2

NA_{sys} FPM coherent synthetic aperture (computed via Eq. 2.5) closely adheres to the theoretical limit. Furthermore, as our Sparrow limit measurement relies upon images of multiple targets, we can immediately ascertain if one target is tilted or misaligned (i.e., setting one aperture out of phase with the other), ensuring this measurement is robust against experimental error.

We also search for the same intensity dip vanishing point within image traces taken with our 1.45 NA_{sys} FPM setup (Fig. 5.2(b5)). These traces exhibit a higher contrast than the corresponding traces from the 1.2 NA_{sys} FPM setup, as expected. The intensity dip now disappears at a center-to-center spacing of 330 nm. This suggests our measured Sparrow resolution limit is approximately 335 nm, which deviates by 13% from theory (296 nm) for a 1.45 NA coherent microscope. In both cases, the small difference between theory and experiment is attributable to a mismatch in nominal NA and aberrations within the microscope objective that are not accounted for, thus concluding that Eq. 2.5 is an accurate model.

For comparison, we also image the same set of two-slit targets with a conventional incoherent microscope setup. We test the resolution performance of three different objective lenses: a 20X 0.5 NA objective, a 40X 0.75 NA objective and a 100X 1.25 NA oil immersion objective (Olympus PLN 100X). For each, we illuminate the sample with a halogen lamp beneath a condenser (i.e., Köhler illumination with matched illumination NA [62], and here we use Olympus U-AC2 condenser for 20X 0.5NA and 40X 0.75NA objective and Olympus U-AAC oil immersible condenser for 100X 1.25NA objective), and place a red filter (Thorlabs FB630-10) in the light path to match its spectrum to the FPM LED illumination spectrum.

Sample images from the conventional microscope are shown in Fig. 5.2(a), columns two to four. We plot a vertical trace through the two-slit intensity distribution for each of these sample images, shown in Fig. 5.2(b1)-(b3). Under Köhler illumination imaging, the theoretical Sparrow resolution limit is given as $d = 0.44\lambda/\text{NA}$ (Appendix A.4). A comparison between the theoretical value and each of our measured Sparrow resolution limits for the three tested incoherent microscope objectives is in Table 5.1.

The measurements for the incoherent microscope objectives showed significant and increasing deviations from theory as the NA increases. This mismatch is likely attributable to the deviation of their practical NA from their nominal NA, which includes the negative impact of uncorrected aberrations. It is generally known that due in part to a larger deviation from the paraxial approximation, aberrations

	System Parameter	Theoretical Sparrow resolution (nm)	Measured Sparrow resolution (nm)	Deviation from theory
Conventional Microscope	20X 0.5NA	556	615	11%
	40X 0.75NA	371	455	23%
	100X 1.25NA	222	315	42%
FPM 1.2 NA_{sys}	0.5 NA_{obj} + 0.7NA_{illu}	358	385	8%
FPM 1.45 NA_{sys}	0.75 NA_{obj} + 0.7NA_{illu}	296	335	13%

Table 5.1: Sparrow resolution for microscope systems (λ = 632nm, two-slit targets)

are harder to eliminate within higher NA lenses [50]. Perhaps, of more pertinent importance is the observation that the 1.45 system NA FPM achieved a measured Sparrow resolution that is comparable to that of an incoherent 1.25 NA oil-immersion objective.

Finally, we would like to point out that the slightly larger Sparrow resolution limit for the 1.45 NA_{sys} FPM compared to the 100X 1.25 NA oil immersion objective does not necessarily means a vaguer image for practical samples, since the phase relationship of the sample will have an influence on the coherent system's resolution performance. This point will be further elaborated upon in the next section.

Our observations here remind us that when using a high-NA objective lens, the nominal NA value (as marked on the lens casing) is not necessarily the best indicator for imaging system cutoff resolution, due to its high measurement-to-theory resolution deviation. Instead, the precise value should be calibrated via a test target. We suggest that our two-slit target sequence is a simple and robust procedure offering accurate results. At the same time, these tests reveal that FP offers a well-controllable way to improve resolution performance while preserving the longer working distance, larger FOV, and less-aberration-challenge benefits of lower-NA microscope objectives.

At this point, we would like to point out that resolution provides a convenient and objective way for comparing microscope performance. The overall image quality is much more difficult to quantify, if at all possible. In fact, image quality can differ not just between systems, but is also dependent on the samples that are examined. The strong diffraction fringes observable for the 1.45 NA_{sys} FPM in Fig.

5.2 is attributable to the sharp cutoff in transfer function associated with a coherent imaging nature of the FPM. The dropoff of the optical transfer function for an incoherent system (conventional microscope) is much more gradual [3]. This does not imply that a coherent system is inferior in general, because system performance is highly sample dependent. This point is well explained in [3] and illustrative examples can be found in Fig. 6.17 and 6.21 of the book. The subjectivity of image quality versus the objectivity of resolution quantification is the reason we chose resolution as the way to benchmark and quantify the performance of our system. In the next section, we will look at the various system image performance with an actual biospecimen.

5.4 Imaging Performance

In this section, we demonstrate how our high-NA FPM systems may benefit a particular medical imaging scenario: the diagnosis of malaria-infected human blood. We prepare a sample slide containing malaria-infected blood cells by first maintaining erythrocyte asexual stage cultures of the P. falciparum strain 3D7 in culture medium, following the protocol described in [63]. Then, we smear these cultures on glass slide, fix them with methanol, and stain them with a Hema 3 stain set (a modified Wright-Giemsa stain).

To image the stained cells with a conventional microscope, we use the same incoherent Köhler illumination as the previous section, but now without a spectral filter. To obtain color images of the cells via FPM, we repeat the FP capture and process steps three separate times using red, green, and blue LED illumination from the same LED array, and then place each reconstruction in the appropriate color channel for the final color image in Fig. 5.3(a). We apply gamma adjustment to this final color image to diminish its difference in color with the conventional microscope images, caused by differences in the spectrum of the illumination light. We detail imaging performance in two image sub-regions, marked by red squares in Fig. 5.3(a). The same sub-regions from our 1.2 NA_{sys} and 1.45 NA_{sys} FPM reconstructions are in Fig. 5.3(e)-(f). The pebbly pattern in the cells on 1.2 NA_{sys} FPM image and the colorized pattern in the background on 1.45 NA_{sys} FPM images are mainly caused by the variation of brightness between LED elements and between RGB chips within an LED, which are not fully corrected in the reconstruction process. Images from the conventional color microscope setup, using the same three different objective lenses as noted above, are in Fig. 5.3(b)-(d). Image clarity increases as the objective lens NA increases, but at a sacrifice of a smaller field-of-view (marked for each

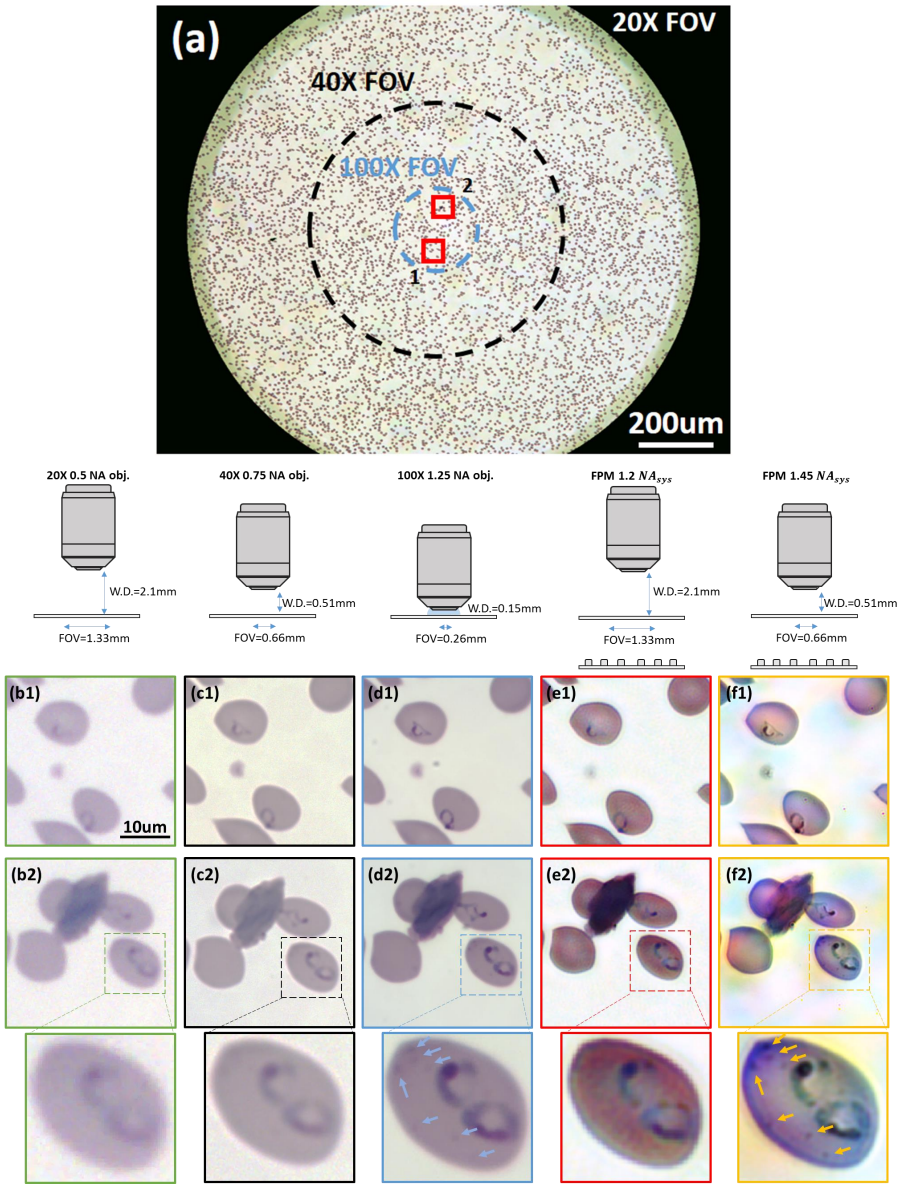

Figure 5.3: Microscope images of a malaria infected blood smear. (a) Full-sized 1.2 NA_{sys} FPM reconstruction, which maintains the FOV and working distance of the 20X objective. The FOV of the 40X and 100X objective are marked with black and blue circles, respectively. (b1-b2) Two sub-regions from (a) (marked with red squares) captured by the 20X objective, (c1-c2) 40X 0.75 NA objective lens, and (d1-d2) 100X 1.25 NA objective lens. (e1-e2) 1.2 NA_{sys} FPM, (f1-f2) 1.45 NA_{sys} FPM images of cells from the same sub-regions. A malaria infected red blood cell from sub-region 2 are further zoomed in, showing particles (pointed by arrows) that are clearly resolved by 1.45 NA_{sys} FPM and vaguely resolved by 100X oil immersion microscope.

objective lens with dashed circles in Fig. 5.3(a)) and a smaller working distance (noted in each lens diagram).

The 1.2 NA_{sys} FPM's image is sharper compare to the 40X 0.75NA conventional microscope setup, while the 1.45 NA_{sys} FPM images contain details that are not resolved in any of the other images. For one example, a malaria infected red blood cell from Fig. 5.3(a) sub-region 2 are further zoomed in, showing particles (pointed by arrows) that are clearly resolved by 1.45 NA_{sys} FPM (Fig. 5.3(f2)). In comparison, for 100X oil immersion microscope, part of these particles are vaguely resolved and part of them are not resolved (Fig. 5.3(d2)), while all the particles are not resolved in the rest of the microscope setups.

As noted earlier, the Sparrow resolution measurements for each of our FPM setups was performed on a slit pair. Light transmitted through both slits undergoes the same phase retardation. A coherent imaging system (such as the FPM) can be expected to underperform for such a target more so than in an incoherent system (such as a standard microscope). Conversely, if the transmissions are not in phase, the two-point resolution cutoff can outperform for a coherent system [3, 64]. As such, our Sparrow resolution measurements for our FPM systems establish base resolution (underestimation) scores for FPM. In a sample with significant phase variations (such as blood cells), the FPM can be expected to provide better resolution performance. Finally, we again note that differences in the nature of the transfer functions between the two systems can lead to variations in the FPM and standard microscopy images.

The FP technique simultaneously acquires quantitative sample phase during high-resolution intensity image reconstruction [51]. We can use the reconstructed sample phase to simulate other modalities typically offered by microscope systems, such as differential interference contrast (DIC) or dark-field imaging. This simulation requires no physical modification to the imaging system. Figure 5(a1-a2) shows the intensity and phase from a small region of the blood smear sample image in Fig. 5.3, taken with the 1.2 NA_{sys} FPM under red LED illumination. Phase gradient images in both directions are shown in Fig. 5.4(b1-b2), which have a similar appearance to what we will see under DIC microscope. Also, a simulated dark field microscope image assuming a 0.5 NA objective lens and condenser with 0.65-0.7 NA illumination ring is in Fig. 5.4(c).

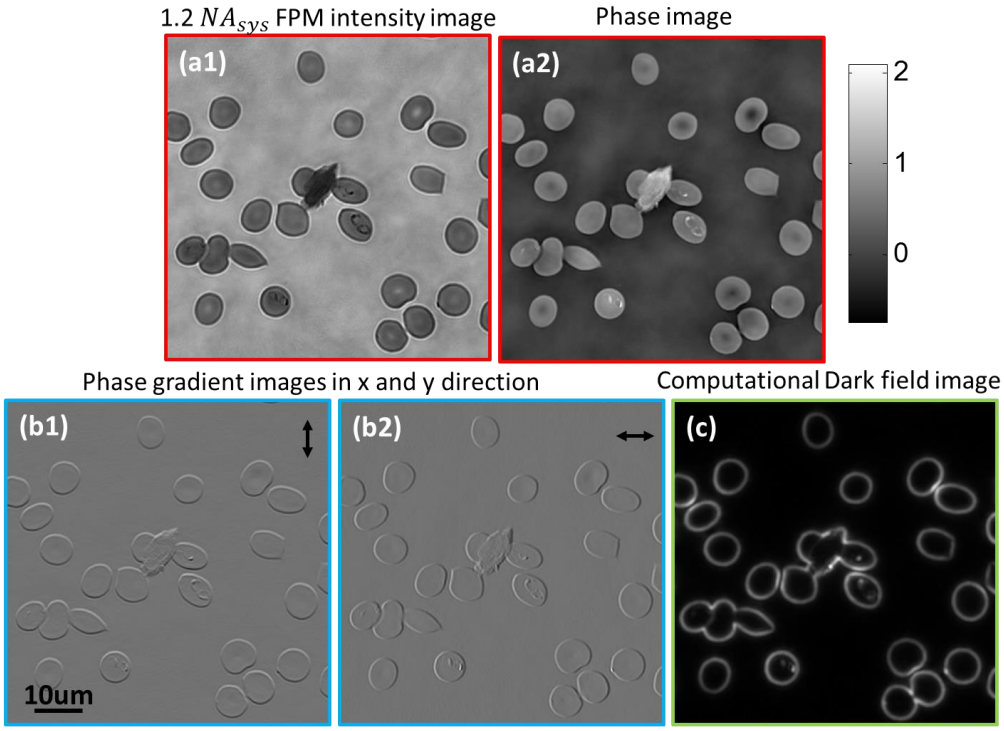

Figure 5.4: The amplitude and phase from FPM images may be post-processed into different modality of microscope (a1-a2) 1.2 NA_{sys} FPM intensity and phase image of the blood smear sample in Fig. 5.3. (b1-b2) Phase gradient images (similar appearance as DIC image). (c) Simulated dark field image using the data in (a).

5.5 Conclusion

In this chapter, we first described a new interpretation of Fourier ptychography as a coherent aperture synthesis technique, arriving at the conclusion that its synthesized system NA equals the sum of its objective NA and illumination NA. Then, we demonstrated for the first time an FPM system with an NA_{sys} over unity. This demonstration was performed on two unique setups: a 1.2 NA_{sys} setup formed by a 0.5 NA objective lens with a 0.7 illumination NA LED ring, and a 1.45 NA_{sys} setup formed by a 0.75 NA objective lens and the same LED ring. We verify the predicted synthesized aperture sizes for each FPM setup using a simple Sparrow resolution limit measurement, finding good agreement with theory. Performing the same Sparrow limit measurement with several conventional microscope configurations led to a larger mismatch between measurement and theory, attributable to larger uncorrected aberrations within higher-NA objective lenses. We further found that the 1.45 NA_{sys} FPM gave comparable resolution performance to an incoherent 100X 1.25 NA oil immersion objective standard microscope. Finally, we used our

FPM system to obtain comparable or better color imagery of a biological sample than a conventional 100X oil immersion objective lens.

This study substantiates our initial conjecture that the use of lower-NA objective lenses in FPM can yield resolutions that are competitive with those of standard microscopes using higher NA objectives. Particularly intriguing is our experimental result showing that an FPM employing a 40X 0.75 NA objective can give comparable resolution to that of commercially available standard microscope with an oil-immersion 100X 1.25 NA objective. We would like to stress that the observed competitive performance of the FPM with the 100X oil immersion objective is attributable to the inability of the oil immersion objective to deliver NA-limited resolution, rather than some extraordinary FPM ability. In other words, a perfect aberration-free oil immersion objective can be expected to perform better.

As a whole, these findings indicate that high-NA FPM offers five primary experimental benefits over conventional high-NA microscope counterparts: a wider FOV, longer working distance, larger depth-of-field, an ability to measure sample phase, and a mitigation of the need for an oil immersion medium in certain situations. These five primary advantages come with certain costs. First, FPM must acquire multiple images over time. Second, it now operates only with thin samples, and in its current configuration cannot improve the resolution of fluorescent samples. Finally, its image recovery process is an inverse problem that can be computationally demanding for large data sets. That said, a number of alternative applications may immediately gain from the above five advantages, given they are unaffected by or can tolerate these costs. Examples include the study of bacteria [65], differential leukocyte counting [66], muscle tissue examination [67], and, as we briefly demonstrated, malaria diagnosis [68].

Several future experimental steps may help improve high-NA FPM. First, the LED ring array we used for sample illumination in both FPMs was optimized for the 1.2 NA_{sys} FPM design. The 1.45 NA_{sys} FPM, using a 0.75 NA objective lens, can benefit from an even higher illumination NA. Second, an embedded pupil function recovery algorithm [69] can be implemented to simultaneously estimate and remove lens aberrations from our final FPM reconstruction. This additional step may lead to improved image quality. Finally, we conclude that Fourier ptychography offers a consistent technique to improve the resolution of conventional microscope objective lenses across all magnifications, and has the potential to scale up to even higher-NA configurations than this work includes.

Chapter 6

APERTURE SCANNING FOURIER PTYCHOGRAPHIC MICROSCOPY

6.1 Introduction

Fourier Ptychography (FP) [31, 52] is a recently developed phase retrieval technique that utilizes intensity images of limited numerical aperture (NA) overlapped in the Fourier domain to reconstruct a sample's complex field. In the original demonstration [31], angularly varying illumination realized by an LED matrix is used to scan the sample's Fourier spectrum, resulting in an expanded synthesized NA of the system. Images with resolution higher than the diffraction limit of the objective lens can be reconstructed [31, 32]. Quantitative phase measurement of the sample is also achieved [51].

The limitation of the angular illumination configuration of FP is its requirement on a sample's thickness[32]. Once the sample's thickness exceeds the thin-sample limit, the simple correlation between the change of illumination angle and the shift in 2D Fourier spectrum is no longer valid, and the phase retrieval algorithm would fail. Tian et al. [70] proposed and demonstrated a modification on FP to reconstruct a 3D sample by approximating the 3D sample as a stack of 2D slices. Horstmeyer et al.[71] modeled the imaging process as diffraction tomography and modified the reconstruction accordingly, resulting in a phase retrieval of the scattering density of a 3D sample. For both modifications, the computational complexity is increased dramatically.

FP can be implemented in an alternate configuration by placing a scannable aperture at the Fourier plane of the imaging system while illuminating the sample with a single plane wave. In this configuration, the wavefront (scattered field) exiting the sample is captured and reconstructed, and the thin sample requirement is circumvented.

In this work, we demonstrate the usage of conventional microscope elements to build an aperture scanning FP microscope (ASFPM) in section 2. This work builds on previous non-microscopy FP works that are focused on 3D sample refocusing [72] and aberration removal [73]. We show that ASFPM can be used for transmissive mode and reflective mode imaging. In section 3, we image spirogyra (transmissive)

and microprocessor chip (reflective) with our setup, and demonstrate our ability to refocus through thick samples at designated plane. In section 4, we show that ASFPM's reconstructed result could be combined with decompressive recovery method to recover the 3D sample scattering density information.

6.2 System Setup

The core of ASFPM is a 4-f imaging system with a spatial light modulator (SLM) at the intermediate Fourier plane, as shown in Fig. 6.1 (a). The wavefront exiting the sample is collected by the first lens, passing through the open aperture of the SLM and reimaged on the camera. A sequence of intensity images of the wavefront is captured with different parts of the SLM aperture opened. The captured images contain different spatial frequency information of the wavefront determined by the open aperture's location. These images are the input of the phase retrieval algorithm [31] to be stitched in the Fourier domain. The aperture opening sequence is arranged such that the adjacent apertures have a certain degree of overlap [14], providing redundant information for the phase retrieval algorithm to retrieve phase information merely from intensity measurements. The reconstructed complex Fourier spectrum is then converted to the complex sample wavefront, with the resolution limited by the aperture scanning range of the SLM. Because the wavefront carries information from the entire sample volume, it can be further processed to analyze sample distribution at different depths.

The experimental setup of the transmissive mode and reflective mode ASFPM are shown in Fig. 6.1 (b) and (c), in which a reflective mode liquid crystal on silicon display (LCOS display) (Model: Holoeye LC-R 1080) in combination with a pair of linear polarizers (LP1 and LP2) are used as the SLM. An objective lens (Olympus 20X 0.4NA) and a tube lens serve as the forward and inverse Fourier transforming device for the 4f system. Because the back focal plane of the objective lens is inside the lens set and not accessible by the LCOS, a 1:1 relay lens system (L3 with L4) is added in between to image the back focal plane of the objective onto the LCOS. For the illumination, light from a He-Ne laser (λ=632.8nm) is first shined on a rotating ground glass diffuser. The rotating diffuser decreases the temporal coherence of the light, which reduces the speckles in the captured image[74]. The scattered light from the diffuser is then collected into a multi-mode fiber, which allows for easy switching between transmissive and reflective mode. For both modes, lenses are arranged to illuminate the sample with a collimated beam.

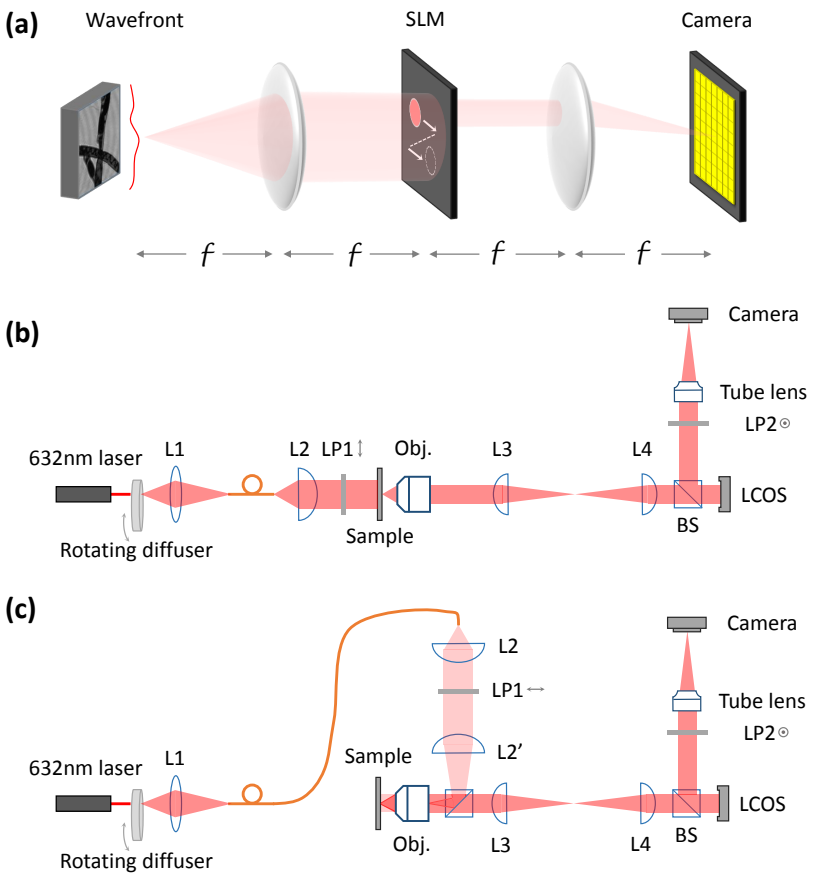

Figure 6.1: Principle of aperture scanning Fourier ptychographic microscopy (a), and schematic for transmissive (b) as well as reflective (c) mode microscope system. f: focal length of the lens; L, lens; LP, linear polarizer; Obj., objective lens; BS, beam splitter

While prior work [73] has used an electronically addressable SLM to implement Fourier ptychography, the current setup offers the following 4 key benefits: 1) usage of a reflective LCOS with a much higher fill factor and efficiency than the previously used transmissive liquid crystal display, 2) removal of temporal coherence artifacts, 3) adoption to a microscopic imaging arrangement, and 4) a new capability to operate in a reflective configuration.

A Siemens star resolution target, recommended by ref. [75], is used as a sample to test the lateral resolution of the imaging system. The patterns are fabricated on gold-coated glass by focused iron beam. For all experiments, a circular aperture on the SLM plane is used to scan the sample's Fourier spectrum, as shown in Fig. 6.2 (a) by the blue trajectory. Each aperture has 80% of its region overlapped (in one dimension) with its adjacent one, and the scanning covers a Fourier spectrum

range equaling a numerical aperture of $NA_{syn} = 0.36$, which is within the NA of the 20X 0.4NA objective lens. 20 images are captured in transmissive mode, and the phase retrieval algorithm is used to reconstruct an image. The intensity of the reconstructed image is shown in Fig. 6.2 (b). The center of the image is magnified and shown in Fig. 6.2 (c). A red circle with spoke periodicity of 1.8 μm is drawn in Fig. 6.2 (c), and the intensity distribution on the circle is plotted in Fig. 6.2 (d). As we can see, the spokes with periodicity of 1.8 μm can be resolved by our imaging system, which matches well with the theoretical resolution defined by the synthesized NA: $d = \lambda/(NA_{syn}) = 1.76\mu$m.

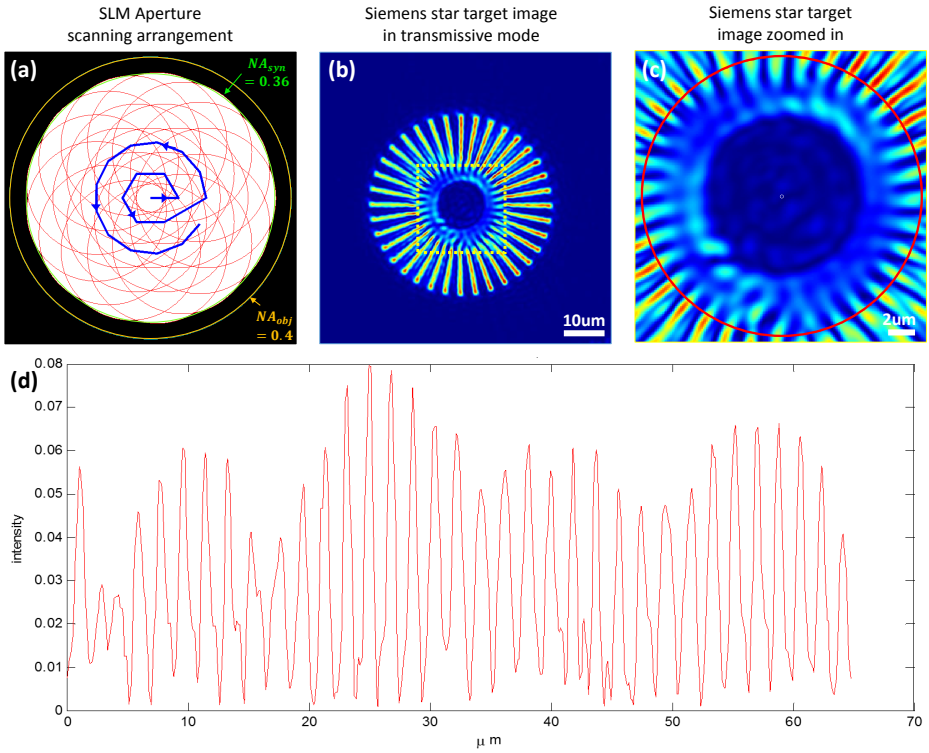

Figure 6.2: (a) The arrangement of aperture scanning sequence on the SLM plane. A circular aperture is scanned following the blue trajectory. The covered area provides a synthesized NA of 0.36, which is within the objective NA of 0.4. (b-c) Siemens star target intensity image in transmissive mode ASFPM. (d)intensity distribution of the red circle in (c), showing a resolution of 1.8 μm which matches the theoretical resolution of the synthesized NA.

6.3 Imaging Performance

To demonstrate the refocusing capability of ASFPM for a thick sample, a multilayer spirogyra slide is imaged in transmissive mode. The reconstructed hologram is shown in Fig. 6.3 (a1-a2), in which no feature is in focus. The angular spec-

trum propagation (ASP) method [3] is used to digitally propagate the hologram to distances of -9μm, 6μm, and 17μm away from the objective's front focal plane as shown in Fig. 6.3 (b1-b3), allowing different segments of the spirogyra to come into focus. The in-focus filament for each refocused plane is indicated by the red arrow, in which the helical arrangement of the chloroplasts can be observed clearly.

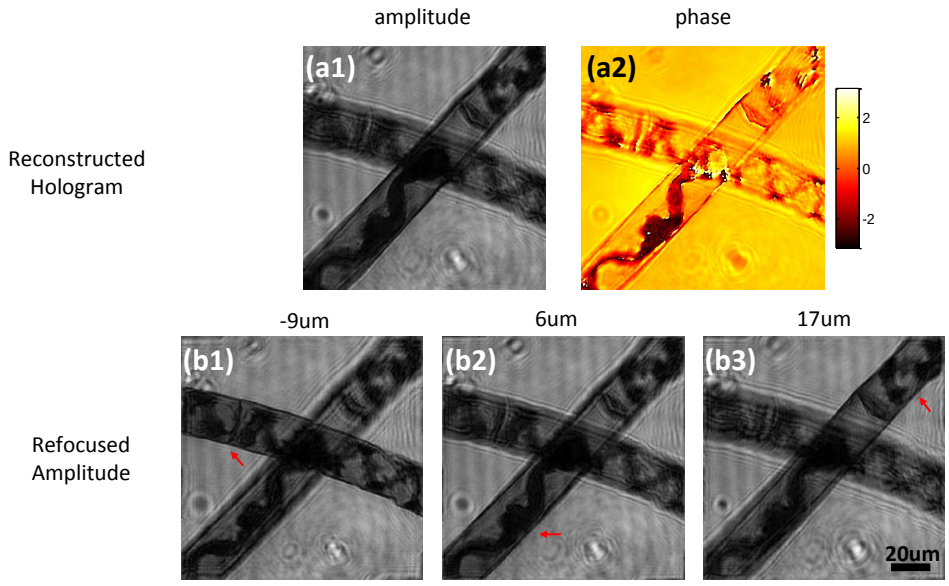

Figure 6.3: Transmissive mode ASFPM image of a spirogyra slide. (a1-a2) Amplitude and phase distribution of the reconstructed hologram. (b1-b3) Refocused amplitude image of the hologram at different focal planes, in which different filaments come into focus as indicated by red arrows.

The reflective mode ASFPM can be used to examine non-transparent samples such as semiconductor devices, metallic structures, and ceramic surfaces. In our experiment, we image a microprocessor (Fig. 6.4 (a)) with our ASFPM and show the reconstructed hologram in Fig. 6.4. (b1-b2). Because the circuit is printed on multiple layers, the hologram needs to be digitally propagated to different planes to bring different regions into focus. As an example, three regions labeled by dashed lines are zoomed in and the intensity images at -3μm and 2μm away, respectively, from the objective's focal plane are shown in Fig. 6.4 (c1-c2, d1-d2, e1-e2). The wires in region c and the top half of the region in d are in focus at 2μm plane, while the grating structure in the bottom half of region d and the structures in region e are in focus at -3μm plane. To verify the result, we display on SLM an open aperture with size equal to the synthesized aperture of ASFPM, and capture two intensity images by physically moving the sample to -3μm and 2μm planes. As shown in Fig. 6.4

(c3-c4, d3-d4, e3-e4), the images match closely with the digitally refocused image generated by ASFPM. Moreover, due to the fact that multiple images are captured and processed in ASFPM, the wire's features in region c appear smoother and finer than the single capture result. With the digital refocusing capability, researchers can achieve in-focus images of every small part on the microprocessor and also get the information of the height of different layers. These pieces of information are useful for applications such as quality control, reverse engineering, and CMOS failure analysis.

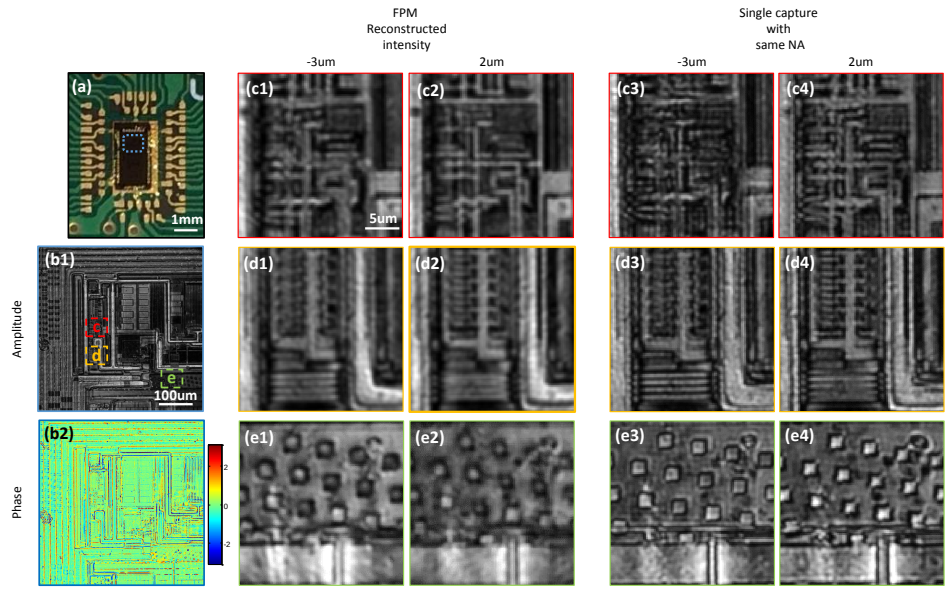

Figure 6.4: Reflective mode ASFPM image of a microprocessor chip. (a) Picture of the microprocessor. (b1-b2) Amplitude and phase of the reconstructed hologram. The hologram is digitally propagated to -3μm (c1-e1) and 2μm (c2-e2) away from the objective lens' focal plane and three sub-regions are zoomed in. Intensity image captured with the aperture opened at NA=0.36 and microprocessor chip physically moved -3μm (c3-e3) and 2μm (c4-e4) are shown as a comparison to the digitally propagated results.

Previous works have verified that the phase information captured in transmissive mode Fourier ptychography, both by angularly-varying-illumination [51] and aperture scanning [73], is quantitative. Here, for the first time, we demonstrate that the phase information captured in reflective mode Fourier ptychography (ASFPM in this case) is quantitative. We spread 10μm microspheres on a silicon wafer, immerse them in mineral oil, and acquire an image with the reflective mode ASFPM. The reconstructed hologram is shown in Fig. 6.5 (a-b). A line trace of phase distribution through one of the microspheres is measured, and converted to microsphere thick-

ness using the equation: $\Delta = \theta/2 * \lambda/(2\pi * (n_{oil} - n_{bead}))$, where θ is the relative phase against background, λ is the wavelength of the laser light, $n_{oil} = 1.5825$ and $n_{bead} = 1.5875$ are the refractive indices of the mineral oil and the microspheres, respectively. The factor of 2 in the denominator takes into account the fact that the collimated beam passes through the microsphere twice before it is collected by the objective lens. The measurement is plotted in Fig. 6.5 (c) with a blue line, and the theoretical value is shown with a black line for comparison. The close agreement between the measured and theoretical line plots proves that the phase information we reconstruct from ASFPM is quantitative.

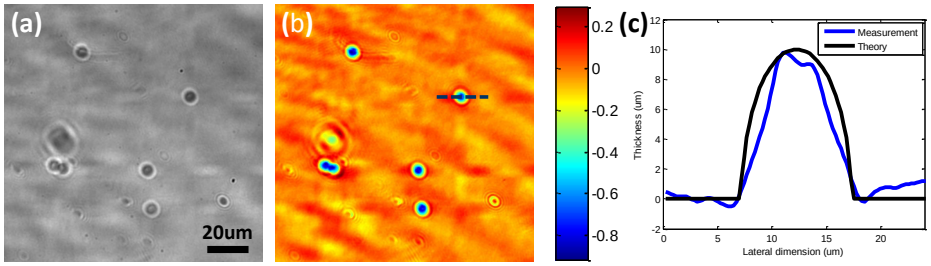

Figure 6.5: ASFPM image of 10μm microspheres on silicon wafer, immersed in mineral oil. Reconstructed amplitude (a) and phase (b) distribution of the hologram. (c) The phase distribution through the dashed line in (b) is converted to the microsphere's thickness and plotted with a blue line. The theoretical thickness distribution is plotted with a black line, showing a good match with the measurement.

6.4 Decompressive Inference of Hologram

As mentioned in section 6.2, ASFPM captures the complex wavefront distribution at the focal plane of the objective lens. When the sample is thin and in focus, the complex wavefront represents the amplitude and phase distribution of the sample. When the sample is thick, this wavefront carries the 3D information of the sample and can be used to bring into focus different planes of interest, as demonstrated in Fig. 6.3 and 6.4.

Furthermore, with the combination of compressive sensing theory [76–78], here we show that 3D tomographic structure of the sample can be recovered from a single frame of 2D holographic data. Similar work and analysis were carried out by Brady et al [79], in which they used Gabor holography, but only the intensity of the 2D holographic data was recorded. Because of the loss of phase information, a few approximations had to be made and the method had difficulties dealing with a phase target. In our case, ASFPM records both the amplitude and phase information of

the hologram. We show in the following section that the quantitative phase as well as the amplitude information of a sample can be recovered from the decompressive inference.

Forward Model of the Compressive Sampling Process

When a 3D sample with the scattering density of $\eta(x', y', z')$ is illuminated with a monochromatic plane wave, the scattered field $E(x, y)$ is defined under the Born approximation [80] as:

$$E(x, y) = \iiint \eta(x', y', z')h(x - x', y - y', z - z')dx'dy'dz', \tag{6.1}$$

where h is the point spread function which can be calculated as the product of $\exp(ik_0z)$ (the phase delay at a distance z) [81] and the inverse Fourier transform of the propagation transfer function $\exp(iz\sqrt{k_0^2 - k_x^2 - k_y^2})$[3], and $k_0 = 2\pi/\lambda$ is the wavevector.

We place the front surface of the 3D sample with scattering density $\eta(x', y', z')$ at the focal plane of the imaging system, i.e. $z' = 0$. To discretize the equation, we let: 1) lateral sample spacings be $\Delta_x = \Delta_y = \Delta$; 2) axial sample spacing be Δ_z; and 3) number of pixels along each dimension of the sample be N. Using this notation, the relationship between the discretized 2D scattered field distribution $E_{n_1n_2} = E(n_1\Delta, n_2\Delta)$ and the discretized 3D sample scattering density $\eta_{m_1'm_2'l} = \eta(m_1'\Delta, m_2'\Delta, l\Delta_z)$ can be expressed as [79] :

$$\begin{aligned}
E_{n_1n_2} =& E(n_1\Delta, n_2\Delta) \\
=& \frac{1}{(2\pi)^2} \int \dots \int dz'dxdydk_xdk_y \iint dx'dy'\eta(x', y', z')e^{ikz'}e^{-i(k_xx'+k_yy')} \\
& \sum_{m_1'} \sum_{m_2'} \delta(x' - m_1'\Delta)\delta(y' - m_2'\Delta)e^{iz\sqrt{k^2-k_x^2-k_y^2}}\delta(z - z')e^{-i(k_xx+k_yy)} \\
& \delta(x - n_1\Delta)\delta(y - n_2\Delta) \sum_{m_1} \sum_{m_2} \delta(k_x - m_1\Delta_k)\delta(k_y - m_2\Delta_k) \sum_{l} \delta(z - l\Delta_z) \\
=& \frac{1}{N^2} \sum_{l} \sum_{m_1} \sum_{m_2} \Big[\sum_{m_1'} \sum_{m_2'} \eta_{m_1'm_2'l} e^{-i2\pi \frac{m_1m_1' + m_2m_2'}{N}} \Big] \\
& e^{ikl\Delta z} e^{il\Delta z\sqrt{k^2-m_1^2\Delta_k^2-m_2^2\Delta_k^2}} e^{-i2\pi \frac{n_1m_1+n_2m_2}{N}}.
\end{aligned} \tag{6.2}$$

This equation can be further simplified by noticing the following two facts: 1) the terms in the square bracket represent the 2D discrete Fourier transform of $\eta_{m_1' m_2' l}$; 2) the last exponential term in the last line of Eq. 6.2 forms the inverse 2D Fourier transform in conjunction with the summations over m_1 and m_2. Therefore, Eq. 6.2 can be interpreted as [79]:

$$\begin{aligned} E_{n_1 n_2} =& \mathcal{F}_{2D}^{-1}\Big\{ \sum_l \hat{\eta}_{m_1 m_2 l} e^{ikl\Delta z} e^{il\Delta z\sqrt{k^2 - m_1^2\Delta_k^2 - m_2^2\Delta_k^2}} \Big\} \\ =& \sum_l \mathcal{F}_{2D}^{-1}\Big\{ \hat{\eta}_{m_1 m_2 l} e^{ikl\Delta z} e^{il\Delta z\sqrt{k^2 - m_1^2\Delta_k^2 - m_2^2\Delta_k^2}} \Big\}, \end{aligned} \tag{6.3}$$

where $\hat{\eta}$ denotes the Fourier transform of η, and $\mathcal{F}_{2D}^{-1}$ denotes the 2D inverse Fourier transform operation on subscript m_1 and m_2. In this interpretation, the 3D sample is treated as a stack of 2D slices, and the 2D scattered field $E_{n_1 n_2}$ is the summation of slice-wise scattered field [82].

To write the equation into a matrix form for the purpose of decompressive inference, we need to reshape the 2D scattered field E_{n_1,n_2} and 3D sample scattering density $\eta_{m_1',m_2',l}$ into 1D vectors $g \in \mathbb{C}^{N_x N_y \times 1}$ and $f \in \mathbb{C}^{N_x N_y N_z \times 1}$, respectively. We define $g_{(n_2-1)\times N_x + n_1} = E_{n_1,n_2}$, and $f_{(l-1)\times(N_x \times N_y)+(m_2'-1)\times N_x + m_1'} = \eta_{m_1',m_2',l}$, where N_x, N_y, and N_z denote the number of pixels in the x-direction, y-direction and z-direction, respectively.

The operation can also be written in matrix form by defining 1) $B = blkdiag($ $F_{2D}, F_{2D}, ..., F_{2D})$ with F_{2D} being the matrix representing the 2D DFT whose size is $(N_x N_z) \times (N_y N_z)$, and "blkdiag" denoting the block diagonal matrix; 2) $Q = [P_1 P_2 ... P_{N_z}]$ with $[P_l]_{m_1 m_2} = e^{ikl\Delta_z} e^{il\Delta_z\sqrt{k^2 - m_1^2\Delta_k^2 - m_2^2\Delta_k^2}}$, where $[P_l]_{m_1 m_2}$ represents the element of the matrix P_l at the intersection of the row m_1 and the column m_2; and 3) G_{2D} represents the 2D inverse DFT matrix.

With these definitions, Eq. 6.3 can be rewritten as:

$$g = G_{2D} Q B f. \tag{6.4}$$

Fig. 6.6 shows the matrix representation of the compressive sampling forward model in the above discussion. The 'compressing' process is the process in which all the slices of the 3D sample propagate and project on to a 2D focal plane, where

the complex hologram is captured. In matrix form, the 'compressing' process is incorporated in the matrix Q, in which the slice-wise information is summed up and shrunk in size.

The linear relationship between the detected hologram and the sample scattering density is the key to decompressive inference. In comparison, for Ref. [79] to achieve a similar linear relationship, the technique had to capture hologram at a significant distance from the sample of interest and exclude the nonlinear term caused by intensity-only measurement. These approximations added to the error of their system and resulted in an inaccurate phase recovery.

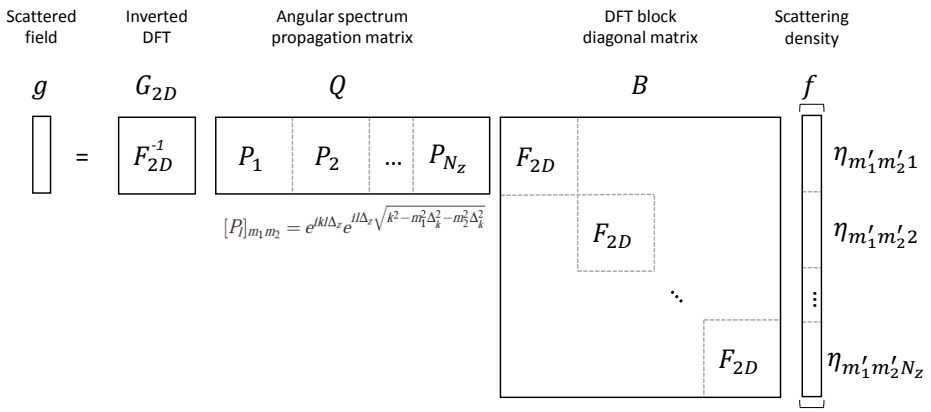

Figure 6.6: Matrix representation of the compressive sampling model

Decompressive Inference Using Total Variation Constraint

To simplify the discussion, let $H = G_{2D}QB$ represent the operation of hologram acquisition. In ref. [79], Brady et al. showed that this holographic acquisition matrix H obeys the restricted isometry property (RIP) [76, 77] as a compressive multiplexed encoder, which ensures an accurate recovery of f from the compressive measurement of $g = Hf$ with a high probability. We notice here that in this previous case, the hologram acquisition process only determined the real values of the optical field, whereas in our case the acquired field are can take on any complex value at each pixel. As a result, our matrix can map values to the entire complex space, as opposed to just the real axis. Thus, our matrix H obeys the RIP of higher order [83] and can in principle lead to the successful reconstruction of samples that are less sparse.

There are different approaches to recover f, such as selecting a basis (wavelets, for instance) in which f may be assumed to be sparse, or enforcing a sparsity constraint on the total variation (TV), as defined by Rudin et al [84], of f. In this

work, we select the second method and model the decompressive recovery of f as an optimization problem:

$$\hat{f} = arg\min_{f} ||f||_{TV} \quad \text{such that} \quad g = Hf, \tag{6.5}$$

where $||f||_{TV}$ is defined by

$$||f||_{TV} = \sum_{l} \sum_{n_1} \sum_{n_2} |\nabla(f_l)_{n_1,n_2}|, \tag{6.6}$$

where f_l denotes a 2D slice of the 3D object datacube. This optimization problem can be solved using the two-step iterative shrinkage/thresholding algorithm (TwIST) proposed in ref. [85]. In this work, we adapt the released MATLAB code from Bioucas-Dias et al [86] to inversely recover f from our measurement of g, which is the complex hologram reconstructed from ASFPM.

Experimental Results

To experimentally demonstrate the performance of decompressive recovery, a two-layer microsphere sample is prepared. A mixture of microspheres with diameter of 4.3 μm (target) and 75 μm (spacer) is spread on the surface of a microscope glass slide and a #1.5 coverslip. These two surface are glued together (face to face) with the immersion oil in between, as shown in Fig. 6.7 (a3). The sample is imaged with the ASFPM setup and the amplitude and phase image is shown in Fig. 6.7 (a1-a2). As we can see, the microspheres that are on the glass slide are close to the in-focus plane, while the microspheres that are on the coverslip are defocused and casting large diffraction rings on top of the image. The hologram is digitally refocused to different imaging planes using ASP, and we find the two planes corresponding to the in-focal plane of the two layers are at 2μm and 45μm (the gap is not 75μm because the spacer microspheres are squeezed in the gluing process). The holographic acquisition matrix H is constructed according to these parameters, and the modified TwIST algorithm is used to recover the sample scattering density on these two planes from the complex hologram reconstructed using ASFPM.

The recovered amplitude and phase distribution of the two layers are shown in Fig. 6.7 (b1-b2, c1-c2). As we can see, the sample information in these two planes are mostly isolated, and the large diffraction fringes disappear. To verify the quantitative-phase-recovery capability of this method, line traces through the center

of two microspheres, one in 2μm plane and the other in 45μm plane are used to calculate the corresponding thickness (same method as mentioned in section 3) and are shown in Fig. 6.7 (b3, c3) with blue lines. The theoretical thickness profile are shown with red lines, which match the recovered result well.

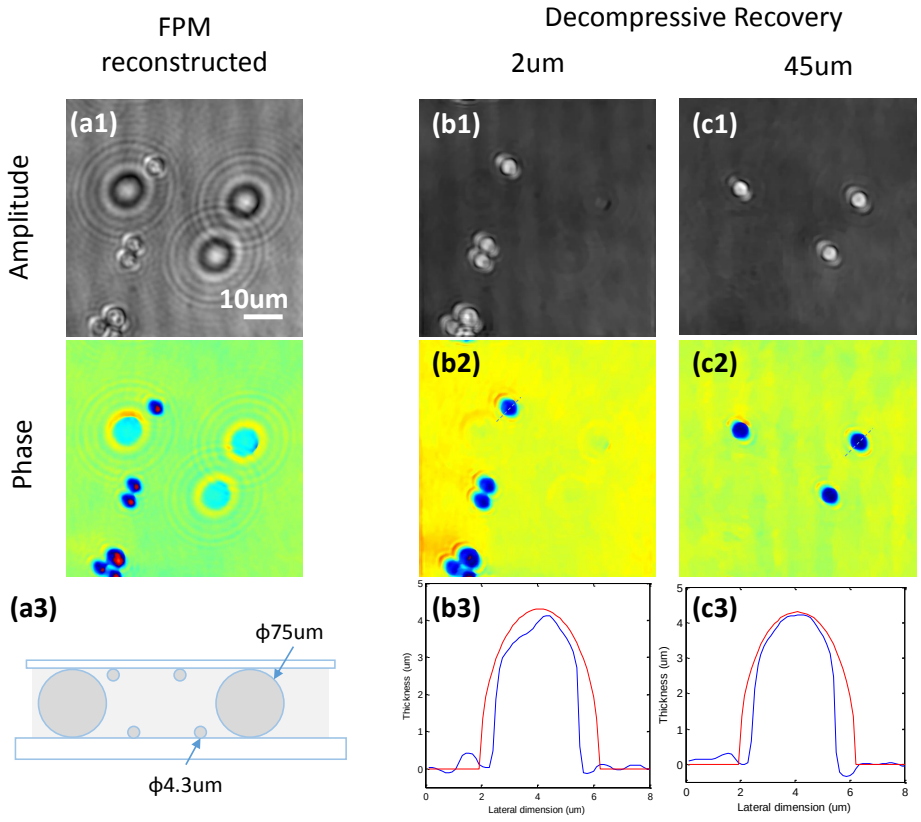

Figure 6.7: Decompressive recovery of a microsphere sample. (a1-a2) Reconstructed amplitude and phase information of the sample using ASFPM. (a3) Two-layer sample configuration. (b-c) Amplitude and phase from decompressive recovery at (b1-b2) 2μm and (c1-c2) 45μm focal planes. (b3) and (c3) are the thickness profiles of microsphere calculated from the recovered phase through the two lines in (b2) and (c2), shown in blue. The red lines show the theoretical thickness value of the 4.3μm microsphere.

In the second experiment, the spirogyra image shown in Fig. 6.3 is inputted into the decompressive recovery algorithm. In this case, the algorithm is modified to recover the sample information in three planes: -9μm, 6 μm, and 17 μm, which are the planes with the sharpest features when refocused. The recovery results are shown in Fig. 6.8. The in-focus parts of the sample manifest themselves in the corresponding planes, both for the amplitude and phase images. The chloroplasts

in the three planes are also reconstructed clearly.

We would like to point out that the recovered result has worse resolution compared to the ASP result. There are two reasons causing this: 1) The spirogyra sample is continuously distributed in z direction, and thus the effort to isolate the 3D continuous information into three slices of 2D distribution introduces some error. 2) The sample is a complicated bio-structure which is not sparse enough in terms of total variation, where the TwIST algorithm used to recover the solution to Eq. 6.5 finds a sparse version of the real sample distribution [87]. The solution has a lower resolution because a smoother function has a smaller total variation compared to a high resolution function with more fine features. The decompressive recovery process may be improved by 1) adding more slices in the reconstruction, and 2) implementing sophisticated sparsity constraint such as dictionary learning [88].

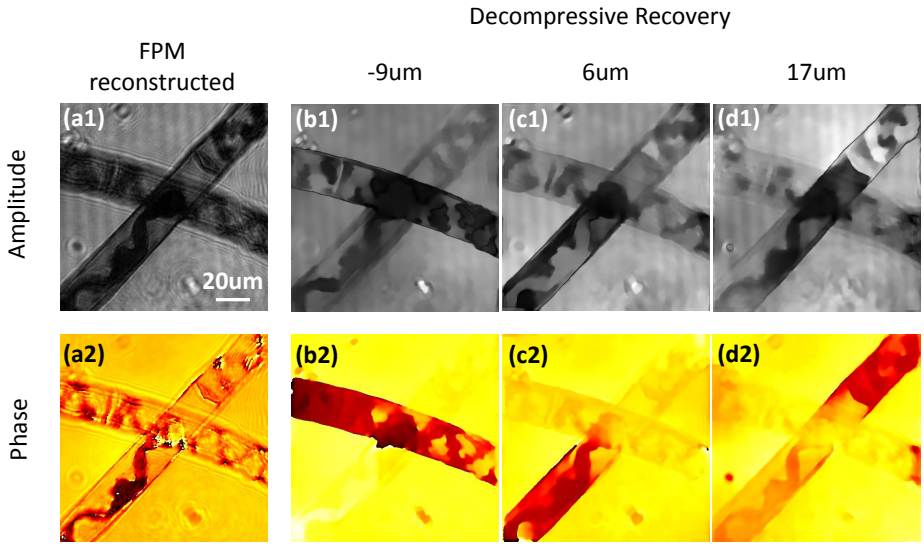

Figure 6.8: Decompressive recovery of spirogyra sample from Fig. 6.3. (a1-a2) Amplitude and phase reconstructed from ASFPM. (b1-d1) Amplitude and (b2-d2) phase recovered from decompressive recovery at -9μm, 6 μm and 17 μm plane.

6.5 Conclusion

In summary, we implemented an aperture-scanning-based Fourier ptychographic microscopy system which reconstructs the complex wavefront from a sequence of intensity measurements. We demonstrated applications in imaging thick biological samples (transmissive mode) and microprocessor surfaces (reflective mode) and digital refocusing, and we verified the phase we measure is quantitative. Moreover, by the introduction of compressive sensing theory, we show that the 3D

sample distribution can be recovered from the 2D complex wavefront. Comparing to other wavefront measurement methods such as digital in line holography [89], ASFPM has several advantages: no interference measurement is needed to reconstruct the phase information, it is easier to align the optical system, and it has a low requirement of temporal coherence which results in much less speckle noise in the reconstructed image. This imaging scheme can be potentially useful in applications such as 3D moving object tracking, semiconductor device testing and analysis, and skin cancer diagnosis.

BIBLIOGRAPHY

[1] E. Abbe, "Beiträge zur theorie des mikroskops und der mikroskopischen wahrnehmung," *Archiv für mikroskopische Anatomie*, vol. 9, no. 1, pp. 413–418, 1873.

[2] M. W. Davidson and M. Abramowitz, "Optical microscopy," *Encyclopedia of imaging science and technology*, 2002.

[3] J. W. Goodman, *Introduction to Fourier Optics*. Roberts and Company Publishers, 2005.

[4] B. E. Saleh and M. C. Teich, *Fundamentals of Photonics*. John Wiley & Sons, New York, 2007.

[5] A. W. Lohmann, R. G. Dorsch, D. Mendlovic, C. Ferreira, and Z. Zalevsky, "Space-bandwidth product of optical signals and systems," *JOSA A*, vol. 13, no. 3, pp. 470–473, 1996.

[6] W. Hoppe, "Beugung im inhomogenen primärstrahlwellenfeld. i. prinzip einer phasenmessung von elektronenbeugungsinterferenzen," *Acta Crystallographica Section A: Crystal Physics, Diffraction, Theoretical and General Crystallography*, vol. 25, no. 4, pp. 495–501, 1969.

[7] J. Rodenburg, "Ptychography and related diffractive imaging methods," *Advances in Imaging and Electron Physics*, vol. 150, no. 07, pp. 87–184, 2008.

[8] J. R. Fienup, "Phase retrieval algorithms: A comparison," *Applied optics*, vol. 21, no. 15, pp. 2758–2769, 1982.

[9] M. Guizar-Sicairos and J. R. Fienup, "Phase retrieval with transverse translation diversity: A nonlinear optimization approach," *Optics express*, vol. 16, no. 10, pp. 7264–7278, 2008.

[10] R. W. Gerchberg, "A practical algorithm for the determination of phase from image and diffraction plane pictures," *Optik*, vol. 35, p. 237, 1972.

[11] W. Saxton, *Computer techniques for image processing in electron microscopy*. Academic Press, 2013, vol. 10.

[12] L.-H. Yeh, J. Dong, J. Zhong, L. Tian, M. Chen, G. Tang, M. Soltanolkotabi, and L. Waller, "Experimental robustness of Fourier ptychography phase retrieval algorithms," *Optics Express*, vol. 23, no. 26, pp. 33 214–33 240, 2015.

[13] R. Horstmeyer, R. Y. Chen, X. Ou, B. Ames, J. A. Tropp, and C. Yang, "Solving ptychography with a convex relaxation," *New journal of physics*, vol. 17, no. 5, p. 053 044, 2015.

[14] S. Dong, Z. Bian, R. Shiradkar, and G. Zheng, "Sparsely sampled Fourier ptychography," *Opt. Express*, vol. 22, no. 5, pp. 5455–5464, Mar. 2014.

[15] S. Chowdhury and J. Izatt, "Structured illumination quantitative phase microscopy for enhanced resolution amplitude and phase imaging," *Biomedical optics express*, vol. 4, no. 10, pp. 1795–1805, 2013.

[16] D. J. Lee and A. M. Weiner, "Optical phase imaging using a synthetic aperture phase retrieval technique," *Optics express*, vol. 22, no. 8, pp. 9380–9394, 2014.

[17] W. Lukosz, "Optical systems with resolving powers exceeding the classical limit," *JOSA*, vol. 56, no. 11, pp. 1463–1471, 1966.

[18] S. A. Alexandrov, T. R. Hillman, T. Gutzler, and D. D. Sampson, "Synthetic aperture Fourier holographic optical microscopy," *Physical review letters*, vol. 97, no. 16, p. 168 102, 2006.

[19] P. Feng, X. Wen, and R. Lu, "Long-working-distance synthetic aperture Fresnel off-axis digital holography," *Optics express*, vol. 17, no. 7, pp. 5473–5480, 2009.

[20] Y. Cotte, F. Toy, P. Jourdain, N. Pavillon, D. Boss, P. Magistretti, P. Marquet, and C. Depeursinge, "Marker-free phase nanoscopy," *Nature Photonics*, vol. 7, no. 2, pp. 113–117, 2013.

[21] V. Mico, Z. Zalevsky, P. Garcia-Martinez, and J. Garcia, "Synthetic aperture superresolution with multiple off-axis holograms," *JOSA A*, vol. 23, no. 12, pp. 3162–3170, 2006.

[22] T. R. Hillman, T. Gutzler, S. A. Alexandrov, and D. D. Sampson, "High-resolution, wide-field object reconstruction with synthetic aperture Fourier holographic optical microscopy," *Optics express*, vol. 17, no. 10, pp. 7873–7892, 2009.

[23] K. Lee, H.-D. Kim, K. Kim, Y. Kim, T. R. Hillman, B. Min, and Y. Park, "Synthetic Fourier transform light scattering," *Optics express*, vol. 21, no. 19, pp. 22 453–22 463, 2013.

[24] L. Allen and M. Oxley, "Phase retrieval from series of images obtained by defocus variation," *Optics communications*, vol. 199, no. 1, pp. 65–75, 2001.

[25] R. G. Paxman, T. J. Schulz, and J. R. Fienup, "Joint estimation of object and aberrations by using phase diversity," *JOSA A*, vol. 9, no. 7, pp. 1072–1085, 1992.

[26] R. A. Gonsalves, "Phase retrieval and diversity in adaptive optics," *Optical Engineering*, vol. 21, no. 5, pp. 215 829–215 829, 1982.

[27] M. R. Bolcar and J. R. Fienup, "Sub-aperture piston phase diversity for segmented and multi-aperture systems," *Applied optics*, vol. 48, no. 1, A5–A12, 2009.

[28] B. H. Dean and C. W. Bowers, "Diversity selection for phase-diverse phase retrieval," *JOSA A*, vol. 20, no. 8, pp. 1490–1504, 2003.

[29] I. Yamaguchi and T. Zhang, "Phase-shifting digital holography," *Optics letters*, vol. 22, no. 16, pp. 1268–1270, 1997.

[30] H. V. Pham, B. Bhaduri, K. Tangella, C. Best-Popescu, and G. Popescu, "Real time blood testing using quantitative phase imaging," *PLoS One*, vol. 8, no. 2, e55676, 2013.

[31] G. Zheng, R. Horstmeyer, and C. Yang, "Wide-field, high-resolution Fourier ptychographic microscopy," *Nature photonics*, vol. 7, no. 9, pp. 739–745, 2013.

[32] X. Ou, R. Horstmeyer, G. Zheng, and C. Yang, "High numerical aperture Fourier ptychography: Principle, implementation and characterization," *Optics express*, vol. 23, no. 3, pp. 3472–3491, 2015.

[33] T. Gutzler, T. R. Hillman, S. A. Alexandrov, and D. D. Sampson, "Coherent aperture-synthesis, wide-field, high-resolution holographic microscopy of biological tissue," *Optics letters*, vol. 35, no. 8, pp. 1136–1138, 2010.

[34] T. Colomb, E. Cuche, F. Charriére, J. Kühn, N. Aspert, F. Montfort, P. Marquet, and C. Depeursinge, "Automatic procedure for aberration compensation in digital holographic microscopy and applications to specimen shape compensation," *Applied optics*, vol. 45, no. 5, pp. 851–863, 2006.

[35] R. K. Tyson, *Principles of Adaptive Optics*. CRC press, 2015.

[36] R. Liang, *Optical Design for Biomedical Imaging*. SPIE Press, 2010.

[37] Z. Bian, S. Dong, and G. Zheng, "Adaptive system correction for robust Fourier ptychographic imaging," *Optics express*, vol. 21, no. 26, pp. 32 400–32 410, 2013.

[38] A. Williams, J. Chung, X. Ou, G. Zheng, S. Rawal, Z. Ao, R. Datar, C. Yang, and R. Cote, "Fourier ptychographic microscopy for filtration-based circulating tumor cell enumeration and analysis," *Journal of biomedical optics*, vol. 19, no. 6, pp. 066 007–066 007, 2014.

[39] C. Audet and J. E. Dennis Jr, "Analysis of generalized pattern searches," *SIAM Journal on Optimization*, vol. 13, no. 3, pp. 889–903, 2002.

[40] G. Zheng, X. Ou, R. Horstmeyer, and C. Yang, "Characterization of spatially varying aberrations for wide field-of-view microscopy," *Optics express*, vol. 21, no. 13, pp. 15 131–15 143, 2013.

[41] W. Singer, M. Totzeck, and H. Gross, *Handbook of Optical Systems, Physical Image Formation*. John Wiley & Sons, 2006, vol. 2.

[42] X. Yang, H. Li, and X. Zhou, "Nuclei segmentation using marker-controlled watershed, tracking using mean-shift, and Kalman filter in time-lapse microscopy," *Circuits and Systems I: Regular Papers, IEEE Transactions on*, vol. 53, no. 11, pp. 2405–2414, 2006.

[43] H. Nomura and T. Sato, "Techniques for measuring aberrations in lenses used in photolithography with printed patterns," *Applied optics*, vol. 38, no. 13, pp. 2800–2807, 1999.

[44] J. Wesner, J. Heil, and T. Sure, "Reconstructing the pupil function of microscope objectives from the intensity PSF," in *International Symposium on Optical Science and Technology*, International Society for Optics and Photonics, 2002, pp. 32–43.

[45] A. M. Maiden and J. M. Rodenburg, "An improved ptychographical phase retrieval algorithm for diffractive imaging," *Ultramicroscopy*, vol. 109, no. 10, pp. 1256–1262, 2009.

[46] J. R. Fienup, "Invariant error metrics for image reconstruction," *Applied optics*, vol. 36, no. 32, pp. 8352–8357, 1997.

[47] V. N. Mahajan, "Zernike circle polynomials and optical aberrations of systems with circular pupils," *Applied optics*, vol. 33, no. 34, pp. 8121–8124, 1994.

[48] G. Zheng, X. Ou, and C. Yang, "0.5 gigapixel microscopy using a flatbed scanner," *Biomedical optics express*, vol. 5, no. 1, pp. 1–8, 2014.

[49] M. Watanabe and S. K. Nayar, "Telecentric optics for focus analysis," *Pattern Analysis and Machine Intelligence, IEEE Transactions on*, vol. 19, no. 12, pp. 1360–1365, 1997.

[50] H. Gross, "Handbook of Optical Systems, Volume 1, Fundamentals of Technical Optics," *Handbook of Optical Systems, Volume 1, Fundamentals of Technical Optics, by Herbert Gross, pp. 848. ISBN 3-527-40377-9. Wiley-VCH, April 2005.*, p. 848, 2005.

[51] X. Ou, R. Horstmeyer, C. Yang, and G. Zheng, "Quantitative phase imaging via Fourier ptychographic microscopy," *Optics letters*, vol. 38, no. 22, pp. 4845–4848, 2013.

[52] R. Horstmeyer and C. Yang, "A phase space model of Fourier ptychographic microscopy," *Optics express*, vol. 22, no. 1, pp. 338–358, 2014.

[53] S. Dong, K. Guo, P. Nanda, R. Shiradkar, and G. Zheng, "Fpscope: A field-portable high-resolution microscope using a cellphone lens," *Biomedical optics express*, vol. 5, no. 10, pp. 3305–3310, 2014.

[54] E. Wolf and M. Born, *Principles of Optics, Electromagnetic Theory of Propagation, Interference and Diffraction of Light*. 1970.

[55] A. Den Dekker, A. Van den Bos, *et al.*, "Resolution: A survey," *JOURNAL-OPTICAL SOCIETY OF AMERICA A*, vol. 14, pp. 547–557, 1997.

[56] R. W. Cole, T. Jinadasa, and C. M. Brown, "Measuring and interpreting point spread functions to determine confocal microscope resolution and ensure quality control," *Nature protocols*, vol. 6, no. 12, pp. 1929–1941, 2011.

[57] S. F. Gibson and F. Lanni, "Experimental test of an analytical model of aberration in an oil-immersion objective lens used in three-dimensional light microscopy," *JOSA A*, vol. 8, no. 10, pp. 1601–1613, 1991.

[58] M. G. Gustafsson, "Surpassing the lateral resolution limit by a factor of two using structured illumination microscopy," *Journal of microscopy*, vol. 198, no. 2, pp. 82–87, 2000.

[59] K. Wicker and R. Heintzmann, "Resolving a misconception about structured illumination," *Nature Photonics*, vol. 8, no. 5, pp. 342–344, 2014.

[60] D. N. Grimes and B. J. Thompson, "Two-point resolution with partially coherent light," *JOSA*, vol. 57, no. 11, pp. 1330–1334, 1967.

[61] C. M. Sparrow, "On spectroscopic resolving power," *The Astrophysical Journal*, vol. 44, p. 76, 1916.

[62] H. Kapitza and S. Lichtenberg, *Microscopy from the very beginning*. Zeiss, 1997.

[63] D. L. van de Hoef, I. Coppens, T. Holowka, C. B. Mamoun, O. Branch, and A. Rodriguez, "Plasmodium falciparum-derived uric acid precipitates induce maturation of dendritic cells," *PloS one*, vol. 8, no. 2, e55584, 2013.

[64] S. Van Aert, D. Van Dyck, and J. Arnold, "Resolution of coherent and incoherent imaging systems reconsidered - Classical criteria and a statistical alternative," *Optics express*, vol. 14, no. 9, pp. 3830–3839, 2006.

[65] R. Zimmermann, R. Iturriaga, and J. Becker-Birck, "Simultaneous determination of the total number of aquatic bacteria and the number thereof involved in respiration.," *Applied and Environmental Microbiology*, vol. 36, no. 6, pp. 926–935, 1978.

[66] I. T. Young, "The classification of white blood cells," *IEEE Transactions on Biomedical Engineering*, vol. 4, no. BME-19, pp. 291–298, 1972.

[67] R. Touyz, G. Yao, M. Quinn, P. Pagano, and E. Schiffrin, "P47phox associates with the cytoskeleton through cortactin in human vascular smooth muscle cells role in NAD (P) H oxidase regulation by angiotensin ii," *Arteriosclerosis, thrombosis, and vascular biology*, vol. 25, no. 3, pp. 512–518, 2005.

[68] *Malaria microscopy quality assurance manual*. World Health Organization, 2009.

[69] X. Ou, G. Zheng, and C. Yang, "Embedded pupil function recovery for Fourier ptychographic microscopy," *Optics express*, vol. 22, no. 5, pp. 4960–4972, 2014.

[70] L. Tian and L. Waller, "3d intensity and phase imaging from light field measurements in an LED array microscope," *Optica*, vol. 2, no. 2, pp. 104–111, 2015.

[71] R. Horstmeyer and C. Yang, "Diffraction tomography with Fourier ptychography," *ArXiv preprint arXiv:1510.08756*, 2015.

[72] S. Dong, R. Horstmeyer, R. Shiradkar, K. Guo, X. Ou, Z. Bian, H. Xin, and G. Zheng, "Aperture-scanning Fourier ptychography for 3D refocusing and super-resolution macroscopic imaging," *Optics express*, vol. 22, no. 11, pp. 13 586–13 599, 2014.

[73] R. Horstmeyer, X. Ou, J. Chung, G. Zheng, and C. Yang, "Overlapped Fourier coding for optical aberration removal," *Optics express*, vol. 22, no. 20, pp. 24 062–24 080, 2014.

[74] S. Kubota and J. W. Goodman, "Very efficient speckle contrast reduction realized by moving diffuser device," *Appl. Opt.*, vol. 49, no. 23, pp. 4385–4391, Aug. 2010.

[75] R. Horstmeyer, R. Heintzmann, G. Popescu, L. Waller, and C. Yang, "Standardizing the resolution claims for coherent microscopy," *Nature Photonics*, vol. 10, no. 2, pp. 68–71, 2016.

[76] E. J. Candes, J. Romberg, and T. Tao, "Robust uncertainty principles: Exact signal reconstruction from highly incomplete frequency information," *Information Theory, IEEE Transactions on*, vol. 52, no. 2, pp. 489–509, 2006.

[77] E. J. Candes and T. Tao, "Near-optimal signal recovery from random projections: Universal encoding strategies?" *Information Theory, IEEE Transactions on*, vol. 52, no. 12, pp. 5406–5425, 2006.

[78] D. L. Donoho, "Compressed sensing," *Information Theory, IEEE Transactions on*, vol. 52, no. 4, pp. 1289–1306, 2006.

[79] D. J. Brady, K. Choi, D. L. Marks, R. Horisaki, and S. Lim, "Compressive holography," *Optics express*, vol. 17, no. 15, pp. 13 040–13 049, 2009.

[80] M. Born, "Quantenmechanik der stossvorgange," *Zeitschrift für Physik*, vol. 38, no. 11-12, pp. 803–827, 1926.

[81] R. E. Blahut, *Theory of remote image formation*. Cambridge University Press, 2004.

[82] D. Paganin, *Coherent X-ray optics*. Oxford University Press, 2006.

[83] E. J. Candes and T. Tao, "Decoding by linear programming," *Information Theory, IEEE Transactions on*, vol. 51, no. 12, pp. 4203–4215, 2005.

[84] L. I. Rudin, S. Osher, and E. Fatemi, "Nonlinear total variation based noise removal algorithms," *Physica D: Nonlinear Phenomena*, vol. 60, no. 1, pp. 259–268, 1992.

[85] J. M. Bioucas-Dias and M. A. Figueiredo, "A new TwIST: Two-step iterative shrinkage/thresholding algorithms for image restoration," *Image Processing, IEEE Transactions on*, vol. 16, no. 12, pp. 2992–3004, 2007.

[86] ——, "Two-step iterative shrinkage/thresholding algorithm for linear inverse problems," [Online]. Available: http://www.lx.it.pt/~bioucas/TwIST/TwIST.htm.

[87] E. J. Candes, J. K. Romberg, and T. Tao, "Stable signal recovery from incomplete and inaccurate measurements," *Communications on pure and applied mathematics*, vol. 59, no. 8, pp. 1207–1223, 2006.

[88] J. Mairal, J. Ponce, G. Sapiro, A. Zisserman, and F. R. Bach, "Supervised dictionary learning," pp. 1033–1040, 2009.

[89] I. Yamaguchi and T. Zhang, "Phase-shifting digital holography," *Opt. Lett.*, vol. 22, no. 16, pp. 1268–1270, Aug. 1997.

[90] A. Lohmann, "Matched filtering with self-luminous objects," *Applied optics*, vol. 7, no. 3, 561_1–563, 1968.

[91] P. Thibault and A. Menzel, "Reconstructing state mixtures from diffraction measurements," *Nature*, vol. 494, no. 7435, pp. 68–71, 2013.

[92] S. Dong, R. Shiradkar, P. Nanda, and G. Zheng, "Spectral multiplexing and coherent-state decomposition in Fourier ptychographic imaging," *Biomedical optics express*, vol. 5, no. 6, pp. 1757–1767, 2014.

[93] Y. Park, C. A. Best, T. Auth, N. S. Gov, S. A. Safran, G. Popescu, S. Suresh, and M. S. Feld, "Metabolic remodeling of the human red blood cell membrane," *Proceedings of the National Academy of Sciences*, vol. 107, no. 4, pp. 1289–1294, 2010.

[94] R. Barakat, "Application of apodization to increase two-point resolution by the Sparrow criterion. I. Coherent illumination," *JOSA*, vol. 52, no. 3, pp. 276–283, 1962.

[95] R. Barakat and E. Levin, "Application of apodization to increase two-point resolution by the Sparrow criterion. II. Incoherent illumination," *JOSA*, vol. 53, no. 2, pp. 274–282, 1963.

[96] D. Goldstein, "Resolution in light microscopy studied by computer simulation," *Journal of Microscopy*, vol. 166, no. 2, pp. 185–197, 1992.

Appendix A

FURTHER ANALYSIS ON SYSTEM PERFORMANCE

A.1 Coherent Requirement Analysis, Fourier Ptychography as a Coherent Imaging System

Here, we briefly discuss the spatial and temporal coherence properties of the FP microscope. While the light from each FPM LED is neither fully temporally or spatially coherent, we now argue why it is suitable to approximate it as such to first-order. This approximation is mathematically equivalent to reducing the full description of each LED illumination via its cross-spectral density (CSD) function, $c(x_1, x_x, v_u)$, to a single coherent field, $\mathbf{U}(x)$, which is the form of our phase retrieval solution. First, to drop the dependence of the CSD upon v, the quasi-monochromatic criterion ($v/\Delta v > M$, with Δv the spectral bandwidth and M the number of sensor pixels along one axis) should be ideally fulfilled [90]. This requires a Δv of several nanometers, which a highly temporally coherent LED may satisfy. (This assumption is independent of the FPM setup's objective NA.)

Second, a spatially coherent field (i.e., a single coherent mode) removes the CSD's statistical dependence upon two spatial coordinates (i.e., we may assume $x_1 = x_2 = x$ if a single coherent mode is present). To fulfill this criterion, the field's spatial coherence length, given by the Van-Cittert Zernike theorem as $l = \lambda z/w$, should extend across the entire image FOV at the sample plane. Here w is the LED active area width and z is distance between the LED and sample. Given image FOV decreases with an increased NA lens, we can expect required spatial coherence conditions to relax in high-NA setups, such as those current demonstrated. The inability to satisfy either of the above temporal or spatial coherence requirements does not fundamentally limit the FPM technique. Several proposed algorithms identify and account for the unknown (spatial and temporal) source incoherence by working with functions resembling the CSD, albeit at the cost of additional computation and possibly more required measurements [91, 92].

Under the above conditions, each raw image in FPM contains the magnitude of a spatially coherent field, and the phase retrieval-based combination of these images is identical to forming a synthetic coherent aperture. The output of an ideal FPM operation is the complex field at the sample plane $s(x)$ filtered by a synthetic

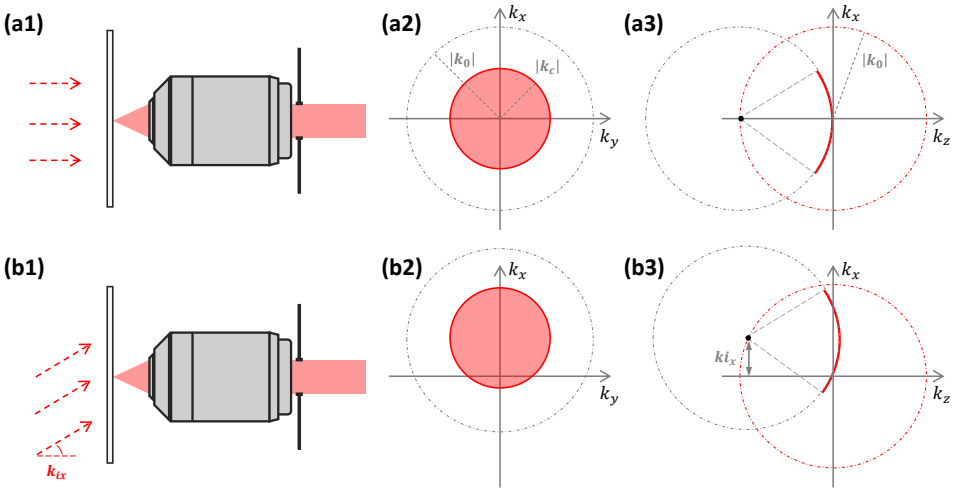

Figure A.1: Three dimensional spatial frequency space analysis of Fourier ptychography. (a1-a3) Normal angle illumination case, (b1-b3) oblique angle illumination case. Solid line red circles and arcs represent spatial frequency information of the sample captured with the microscope system under certain illumination, and dot rings depict the cross-sections of Ewald spheres.

coherent transfer function, CTF(k_x) (the larger rectangle in Fig. 2.2), which defines our system performance. CTF(k_x) is most fairly compared to the physical CTF of the coherently illuminated, high-NA physical system that also detects phase. Thus, we model FP as a coherent imaging system with a synthesized system NA of $\mathrm{NA_{obj}} + \mathrm{NA_{illu}}$.

A.2 The Influence of Sample's Thickness on Fourier Ptychography

In previous discussions, we assume the sample to be infinitely thin in the axial direction such that a tilt in illumination results in a shift of the sample spectrum in Fourier domain. For practical samples with finite thickness, we now introduce a three dimensional spatial frequency representation to further analyze the problem [23].

As shown in Fig. A.1(a1-a3), when a sample is illuminated with a normally incident plane wave, a spherical shell shape fraction of the sample's 3D spatial frequency spectrum can pass through the system and be captured by the camera. The radius of the sphere is determined by the wavevector of light $k_0 = 2\pi/\lambda$, and the radius of the cross section in $k_x - k_y$ space is limited by the numerical aperture of the objective lens $k_c = 2\pi \cdot \mathrm{NA_{obj}}/\lambda$, as shown in Fig. A.1(a2). The center of the grey sphere (known as Ewald sphere) is on the surface of the red sphere, which also

has a radius of k_0. In case of normal incident plane wave illumination, the center is also on k_z axis, as shown in Fig. A.1(a3). When the sample is illuminated by an oblique angle plane wave, the sample's spectrum is going to shift with an amount of (k_{ix}, k_{iy}, k_{iz}). Equivalently, the spherical shell is shift for the same amount to the opposite direction, as shown in Fig. A.1(b1-b3). Since the illumination wavelength is fixed, i.e. $(k_{ix}^2 + k_{iy}^2 + k_{iz}^2 = k_0^2)$, the center of the grey sphere remains on the surface of the red sphere. Here, we define (k_{px}, k_{py}) as the coordinates of the Fourier spectrum of the light field that passes through our imaging system, and (k_x, k_y) as the coordinates of 3D sample spatial frequency spectrum. In this particular case, $k_x = k_{px} - k_{ix}$, $k_y = k_{py} - k_{iy}$.

For an illumination wave with wavevector (k_{ix}, k_{iy}, k_{iz}), the Fourier spectrum of the light field that pass through the imaging system corresponds to a particular 3D sample spatial frequency spectrum. As we can see in Fig. A.1(b3), the k_z component of the sample spectrum is:

$$k_z = \sqrt{k_0^2 - k_{px}^2 - k_{py}^2} - \sqrt{k_0^2 - k_{ix}^2 - k_{iy}^2}. \tag{A.1}$$

From Eq. A.1, we can see that the same (k_x, k_y) sample information acquired by different illumination wavevector (k_{ix}, k_{iy}) will have different k_z, which means simply stitching in the spatial frequency domain for aperture synthesis might not be valid for thick sample. Thus, prior research studies in synthetic aperture required the sample to be thin [21, 22].

Lee et al. [23] reported their further study of the influence of sample's thickness on synthetic aperture for transmission geometry. They states that for a thick sample with h as the crude maximum thickness, the sample Fourier spectrum $\hat{s}(k_x, k_y, k_z)$ can be approximated as $\hat{s}(k_x, k_y, 0)$ for $|k_z| < \delta \cdot k_0$, where $\delta = \pi/(k_0 \cdot h)$ defined as thin-sample limit.

In case of FPM system with $\mathrm{NA_{obj}}$ and $\mathrm{NA_{illu}}$, according to Eq. A.1,

$$|k_z|_{max} = \max\left(k_0 - \sqrt{k_0^2 - (k_0 \cdot \mathrm{NA_{obj}})^2}, k_0 - \sqrt{k_0^2 - (k_0 \cdot \mathrm{NA_{illu}})^2}\right). \tag{A.2}$$

The maximum thickness h that satisfies $|k_z| < \delta \cdot k_0$ for all k_z can be calculated as $h_{max} = \pi/|k_z|_{max}$. For 1.2 $\mathrm{NA_{sys}}$ FPM, $\mathrm{NA_{illu}} = 0.7 > \mathrm{NA_{obj}} = 0.5$, which give us $h_{max} = 1.75\lambda$. As for 1.45 $\mathrm{NA_{sys}}$ FPM, we have $\mathrm{NA_{obj}} = 0.75 > \mathrm{NA_{illu}} = 0.7$, thus $h_{max} = 1.48\lambda$.

According to the derivation above, the ideal thickness of sample for 1.2 NA_{sys} FPM should be smaller than 822nm, while for 1.45 NA_{sys} FPM, this number should be 696nm. The resolution target which is 100nm thick gold falls into this range. For red blood cells, which have average thickness at the thickest point of 2 to 2.5 μm and a minimum thickness in the center of 0.8 to 1 μm [93], this limit is likely exceeded.

In our opinion, the requirement of $|k_z| < \delta \cdot k_0$ is restrictively strict. It is valid for samples with complicated 3D Fourier spectrum distribution in the k_z direction. However, in the case of single layer blood smear sample, structure in the z direction is mainly extension of thickness of the same component. In this case, spectrum $\hat{s}(k_x, k_y, k_z)$ is $\hat{s}(k_x, k_y, 0)$ with a scale down factor in a larger range of $|k_z|$. By rescaling captured images, these information can still be stitched together in Fourier domain – this is likely why we still get reasonable reconstructed images from our samples. However, the noise and artifacts introduced by this process should not be ignored and the rendered images can be significantly impacted if these effects are significant.

A.3 Resolution Calibration Using 2D Circular Hole Pairs

In Fig. A.2 we show our measurements of the Sparrow resolution limit, for the 1.2 NA_{sys} FPM and several conventional incoherent microscope setups, using targets consisting of two circular holes. We fabricated each two-hole calibration target on a gold-coated (100 nm coat thickness) microscope slide using a focused ion beam. Each hole has a diameter of 200 nm and the hole pairs have center to center distance varying from 400 nm to 740 nm. The SEM image of 10 sets of hole pairs are shown in the first row of Fig. A.2(a). The resulting images are shown in the remaining rows of (a), while the traces through each intensity image are shown in Fig. A.2(b). The result of the 1.45 NA_{sys} FPM is not shown here, because the captured images suffered from a high level of noise, due to the low brightness of each LED as compared to an incoherent halogen lamp. Finally, we list the corresponding experimentally measured and theoretically predicted Sparrow resolution limits in Table. A.1. The equations used to predict theoretical Sparrow resolution is listed in Appendix A.4

A.4 Discussion on Sparrow Resolution Limitation for Microscope System

The Sparrow resolution limit [61] of imaging system was first derived by Barakat [94, 95]. The model he used is shown in Fig. A.3(a), and ε' is the

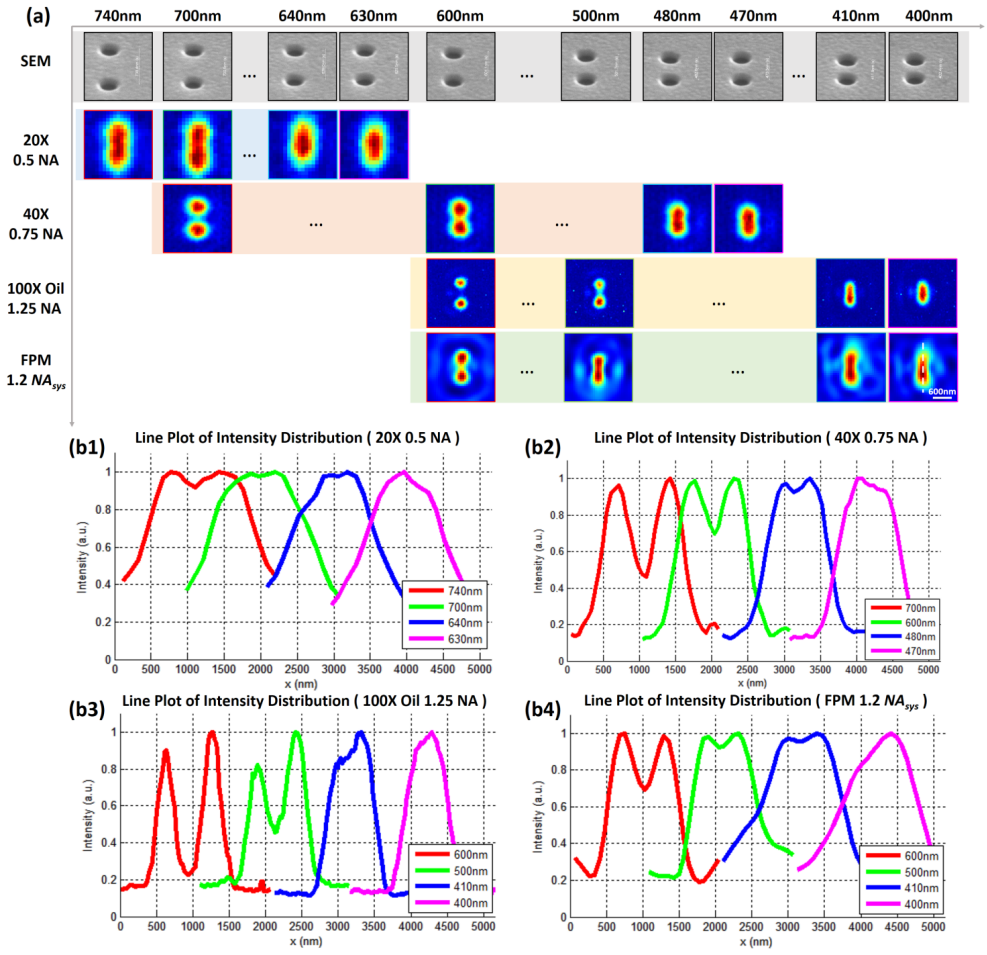

Figure A.2: Resolution calibration using a customized two-hole targets, illumination wavelength λ=632nm. (a) SEM, FPM and conventional microscope image of holes (200nm diameter) on the target. (b) Line plots of vertical intensity distribution through the center of each hole pair, showing a Sparrow resolution of (b1) 635 nm for 20X 0.5 NA objective, (b2) 475 nm for 40X 0.75 NA objective, (b3) 405 nm for the 100X oil immersion 1.25 NA objective, and (b4) 405 nm for 1.2 NAsys FPM setup.

	System Parameter	Theoretical Sparrow resolution (nm)	Measured Sparrow resolution (nm)	Deviation from theory
Conventional Microscope	20X 0.5NA	595	635	6%
	40X 0.75NA	396	475	20%
	100X 1.25NA	238	405	70%
FPM 1.2 NA_{sys}	$0.5\ NA_{obj}$ + $0.7NA_{illu}$	384	405	5%

Table A.1: Sparrow resolution for microscope systems (λ = 632nm, two-hole targets)

minimum resolvable separation in image space, q is the image distance, a is the pupil half-width, and $k = 2\pi/\lambda$ is the wavelength. In the derivation, he assumes the receiving plane is far away from the aperture ($q >> a^2/\lambda$), and thus the image is a Fraunhofer diffraction of the E-field distribution at the aperture plane. The image plane illuminance distribution is analyzed and the separation ε' when the second derivative of the total distribution between two peak vanishes (definition of Sparrow limit) is given by the following relationships [60]:

$$\varepsilon' = \alpha \times \frac{q}{ka}, \tag{A.3}$$

α here is the coefficient determined by image system dimension and illumination condition, which is summarized in Table A.2 [60]:

	Coherent Illumination	Incoherent Illumination
Slit aperture (1D) system	4.164	2.606
Circular aperture (2D) system	4.600	2.976

Table A.2: Sparrow resolution limit coefficient α in different circumstances

For finite corrected microscope system, the two-point image formation schematic is shown in Fig. A.3(b). As have been point out by [54], according to the sine condition, $n\varepsilon \sin\theta = n'\varepsilon' \sin\theta'$, where n, n' are refractive index on sample side and image side of the system, θ, θ' are the angles which the marginal ray make with the axis, and ε is the separation in the sample side. Given that $n' = 1$ for microscope system, and $\sin\theta' \approx \theta' \approx a/q$ (long imaging distance). We have:

$$\varepsilon \approx \frac{\alpha}{2\pi} \times \frac{\lambda}{n \sin\theta} = \beta \times \frac{\lambda}{\mathrm{NA}}. \tag{A.4}$$

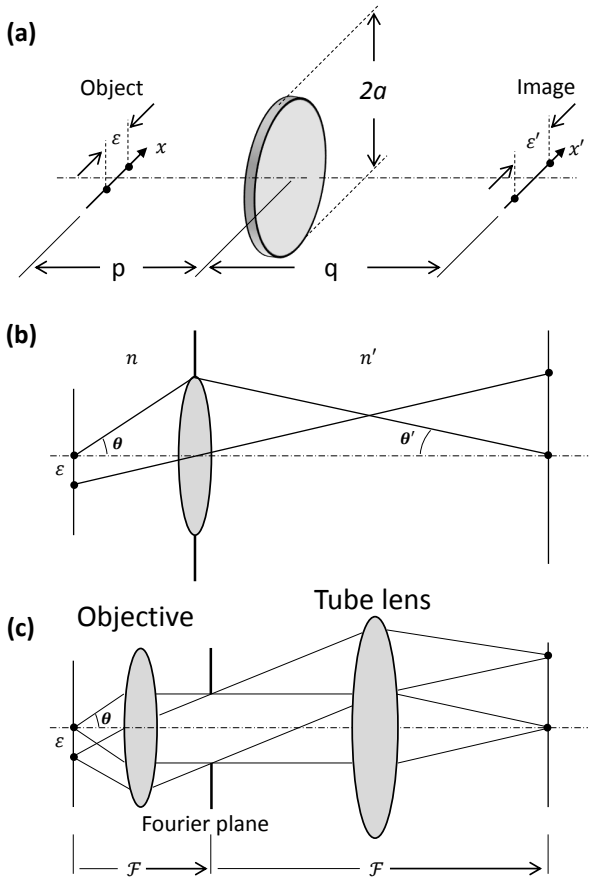

Figure A.3: Two-point image formation. (a) General imaging system (adapted from [60]). (b) Finite corrected microscope system (adapted from [54]). (c) Infinite corrected microscope system.

Here $\beta = \alpha/2\pi$, and the value of β in different circumstances is shown in Table A.3. This derivation might not be valid for high NA objective lenses. For an example, in order to satisfy the Fraunhofer diffraction condition, image distance q needs to be larger than 1.5 m for a 1 mm exit pupil objective lens illuminated by 632 nm light source, while the typical value of image distance is only 160mm.

	Coherent Illumination	Incoherent Illumination
Slit aperture (1D) system	0.66	0.41
Circular aperture (2D) system	0.73	0.47

Table A.3: Sparrow resolution limit coefficient β in different circumstances

As for infinity-corrected microscope system, which is commonly used in

research-grade biomedical and industrial microscopes in the last decade, the image distance of the objective lens is set to infinity, and a tube lens is placed within the microscope to produce the image (Fig. A.3(c)). In this case, the objective lens and the tube lens forms a low pass filter type 4f system, with is cutoff spatial frequency, k_c, defined by the lens numerical aperture, $\mathrm{NA_{obj}}$, and the illumination wavelength: $k_c = 2\pi \cdot \mathrm{NA_{obj}}/\lambda$. Because of the Fourier transform property of the 4f system, no Fraunhofer diffraction assumption and small-angle approximation is needed. Using similar mathematical derivation as mentioned above [94, 95], we can deduce Sparrow resolution limit as:

$$\varepsilon = \gamma \times \frac{\lambda}{\mathrm{NA_{obj}}}, \tag{A.5}$$

which is suitable for both low NA and high NA occasions.

For the case when the object consists of two parallel lines in a 2-D circular aperture system (our scenario in section 3), the coefficient γ is found from a simulations [96]. All the numbers of γ are summarized in Table A.4.

		Coherent Illumination	Incoherent Illumination
Slit aperture (1D) system		0.66	0.41
Circular aperture (2D) system	Two-point target	0.73	0.47
	Two-slit target	0.68	0.44

Table A.4: Sparrow resolution limit coefficient γ in different circumstances